Optical imaging in scattering medium using supercontinuum laser and the effects of polarization

by

Qing Chao

B.E., The University of Sydney, 2008

M.S., University of Colorado at Boulder, 2011

A thesis submitted to the
Faculty of the Graduate School of the
University of Colorado in partial fulfillment
of the requirements for the degree of
Doctor of Philosophy
Department of Electrical, Computer and Energy Engineering
2017

This thesis entitled:
Optical imaging in scattering medium using supercontinuum laser and the effects of polarization
written by Qing Chao
has been approved for the Department of Electrical, Computer and Energy Engineering

Prof. Kelvin H. Wagner

Prof. Daniel Feldkhun

Date

The final copy of this thesis has been examined by the signatories, and we find that both the content and the form meet acceptable presentation standards of scholarly work in the above mentioned discipline.

Chao, Qing (Ph.D., Electrical, Computer and Energy Engineering)

Optical imaging in scattering medium using supercontinuum laser and the effects of polarization

Thesis directed by Prof. Kelvin H. Wagner

As optical imaging in scattering medium is emerging as a promising imaging modality, several challenges arise against deeper imaging due to the multiple-scattering caused by the inhomogeneous distribution of refractive index. To obtain high quality images through active structured light illumination and polarization imaging, an polarized, tunable and intense broadband light source is highly desirable to perform coherence gating for enhancing ballistic photons in a highly scattering medium. This thesis describes the challenges of optical imaging, polarization imaging in scattering medium, the experimental investigations of a dynamic structured illumination microscope (DSIM), and the development of a versatile broadband supercontinuum light source generated using ultrafast nonlinear optics for enabling new optical imaging modalities in scattering medium. The DSIM was demonstrated as a Fourier synthesis and polarization-sensitive imaging method using a moving illumination pattern requiring only a single pixel camera or a photodiode detector. To increase penetration depth in a scattering medium, it is suggested that a broadband supercontinuum laser can be used as a powerful and tunable fiber-based light source for coherence gating to enhance ballistic photons. Therefore, an octave-spanning broadband supercontinuum light laser is experimentally demonstrated using an ultrafast femtosecond Ti:Sapphire seed laser and a highly nonlinear micro-structured photonics crystal fiber. During the experiment, the broadband supercontinuum output is demonstrated to be polarization-dependent, thus a detailed numerical simulation is developed using vectorized generalized nonlinear Schrödinger equations (GNLSE) for both isotropic and anisotropic fiber mediums. The polarization trajectories of Raman solitons in the supercontinuum generation visualized on the Poincaré sphere reveals rich polarization dynamics, including a polarization separatrix for light propagation in the birefringent fiber. While most of the previous works were focused on polarization dynamics for light propagation in linearly birefringent fiber, I investigated the case of circularly birefringent fiber and found a simplified polarization evolution that leads to a motivation for developing twisted fibers for single polarization broadband light sources. The versatile and stable circularly polarized broadband supercontinuum can be potentially one of the most attractive light source to improve optical imaging in scattering medium.

Dedication

This thesis is dedicated to my mother Yang, for raising me up with love and patience, for teaching me to pursue my dream with courage, persistence and faiths.

Acknowledgements

I express my deep gratitude to my PhD advisor Prof. Kelvin Wagner for his encouragements and discussions that motivate me to dive deeper in research. When I was struggling the most, he brought me back on track and provided the most energetic and creative research environment. His amazing intuition and passion in science will continue to inspire me throughout my career.

Prof. Daniel Feldkhun's pioneer work in Doppler encoded excitation pattern microscopy enabled me to explore exciting research topics and I learned tremendously from the insightful conversations with him as I navigate in research. Prof. Steven Cundiff guided my two years of research at JILA and I am grateful for his guidance in creating the first waveguide array mode-locked fiber laser. Dr. Youzhi Li guided my internship in Covidien and it was an amazing experience to research in biomedical optics. Prof. Rafael Piestun introduced me to the optics program at CU-Boulder from Australia and I am thankful for the research experience in his group. I thank Prof. Juliet Gopinath and Prof. Robert Mcleod for their encouragements during my PhD.

The group members Daniel Feldkhun, Keith Nowicki, Stephanie Swartz, and Johnathan Pfeiffer are very supportive in the lab. My friends offered many support throughout my graduate life: Eryan Dai, Lisa Rengnath, Sarah Murray Espinoza, Bosheng Zhang, Hien Nguyen, Lavanya Periasamy, Kendra Krueger, Ginni Grover, Anthony Barsic, Sushant Shresta, Antonio Caravaca, Sepideh Kianbakht, Jim Frank, Xiaoge Zeng, Karissa Kimmel, Nadia Yoza, Margot Crowe, Anurag Agrawal, Ali Sepahvand, Omer Tzang, Haiyan Wang, Judy Lee, Jeremy Brown and Eyal Niv.

I gave my deepest gratitude to my parents for their faith and love. Finally, I praise my savior Jesus Christ for the countless blessings I undeservingly received.

Contents

Chapter

Figures

Figure

Chapter 1

Introduction and motivation of thesis

Optical imaging in scattering environments has attracted significant attention in recent years [1, 2, 3, 4, 5, 6, 7, 8, 9]. The understanding of this phenomena requires the modeling of light-matter interactions, whether a cell or an entire organ in biological tissue, a vehicle in smoke, a fish in the sea or a building in the fog. Optical imaging in scattering media is challenging because the inhomogeneous refractive index distribution can cause multiple-scatterings of light which can severely degrade the image quality or prevent imaging altogether. Because it is often preferable that the object to be imaged remain in its original environment and to avoid disturbing or perturbing the object, it is desirable to only manipulate the optical properties of the incident light [10, 11]. Therefore, an advanced light source with unique optical properties including its polarization, wavelength, bandwidth, spatial and temporal profile, and coherence is highly desirable. Since the invention of the laser in 1960, optical imaging has experienced tremendous growth benefiting from the intense, monochromatic and spatial coherence of laser source [12]. The invention of ultrafast lasers has led to a series of new optical imaging techniques include optical coherence tomography [13], high harmonic optical imaging [14] and multi-photon microscopy [15].

Supercontinuum generation is a technique for producing spatially coherent and ultra-broadband light that was first discovered in bulk crystals in the 1970s [16]. With the rapidly developing diverse host of optical imaging applications, broadband supercontinuum light sources are in high demand for their unique characteristics. For instance, biophotonics for optical imaging in scattering tissue using temporally incoherent light has had a great impact from the development of supercontinuum based laser sources [10]. This broadband light source provides a wide range of wavelengths from UV to Infrared and spatially coherent beam profile for fiber-based supercontinuum generation. It has the bandwidth of sun light but is 10^4 times brighter and the spatial coherence allows diffraction limited focusing. Nonlinear spectroscopy can benefit from the time-resolved multi-wavelength pump-probe functionalities using supercontinuum generation for tracking electron motions in femto-second scale [17]. Frequency combs using supercontinuum generation can enable high resolution spectroscopy from the study of the composition of extrasolar planets to forensic science investigations [18, 19]. Because of the cost effective and compact size considerations, fiber-based supercontinuum light source has the potential to enable even more exciting applications in optical imaging. The broadband supercontinuum generation in photonic crystal fiber (PCF) from extreme spectral broadening based on intense nonlinear light-matter interactions was discovered in early 2000s [20, 21, 22, 23]. The unique capability for dispersion engineering in PCF and highly effective nonlinearity have made the PCF an excellent medium for broadband supercontinuum generation.

In my PhD research, I have investigated optical imaging in scattering media using a polarimetry technique with orthogonal polarization analyzers to improve image contrast. In addition, I studied a structured light illumination technique to achieve Fourier domain optical imaging by acousto-optically modulating the optical light illuminated on an object and detecting the scattered light with a single pixel detector. This technique has the potential to improve optical penetration depth for optical imaging into the scattering medium through a mechanism analogous to coherence gating, and for this technique a broadband supercontinuum light source is highly desirable. I conducted experiment to demonstrate an octave-spanning supercontinuum from a highly nonlinear PCF using dispersion-compensated femtosecond pulses from an ultrafast mode-locked Ti:Sapphire laser. In the experiment, I discovered both the spectral and polarization characteristics of the supercontinuum can be directly controlled by varying a polarization launched into the fiber. To gain physical insights, the polarization dynamics of this laser source was investigated theoretically using a vectorized generalized nonlinear Schrödinger equations (GNLSE) for both isotropic and anisotropic PCF fibers. The Raman scattering induced spectral shift caused by the different incident state of polarizations is revealed through the simulations. The polarization trajectories of the shifting Raman soliton-like spectrum was extracted from the simulation and it is found to be a rich and dynamic process which are visualized on a Poincaré sphere. A polarization separatrix is found for supercontinumm generation when light is propagating in a birefringent PCF. However, most of the previous works for the supercontinuum light source are focused on polarization dynamics of light propagation in a linearly birefringent fiber. In my PhD work, I also investigated light propagation in a circularly birefringent fiber medium using the GNLSE and the Poincaré sphere representation. The numerical simulation reveals a surprisingly simplified polarization evolution for this circularly birefringent PCF. If twisted fiber waveguide can be made to create such a circularly birefringent medium, a circularly polarized broadband supercontinuum source can be employed to potentially improve optical imaging in scattering medium.

The thesis chapters are organized as follows:

Chapter 2 presents the background and theories for light propagation in scattering medium. The challenges of optical imaging in scattering medium and optical properties of scattering medium will be discussed. Mie and Rayleigh scattering will be analyzed using scattering matrix approach. Polarimetry imaging techniques in scattering medium using Stokes and Mueller matrix will be reviewed. In addition, polarization memory effect for circularly polarized light will also be discussed.

Chapter 3 describes biologically inspired polarization gated imaging in scattering medium. Resolution image improvement using polarization difference polarimetry for both Mie and Rayleigh scatterings will be presented using the derived analytical models based on point spread functions. Furthermore, the scattering coefficients of scattering phantom are measured and polarization-gated imaging in the scatter phantom is demonstrated for image contrast enhancement.

Chapter 4 discusses structured light illumination microscopy which is developed for optical imaging in scattering medium. Topics will be described includes Fourier synthesis of objects and Moiré pattern formation, acousto-optic devices for active illumination, the experiment of polarization-interferometric structured light illumination microscopy, and signal reconstruction using the matched-filter algorithm. Using a broadband light source, optical penetration depth can be improved through coherence gating, hence through the theoretical simulation performed recently, a broadband supercontinuum light source is highly desirable for our optical imaging application.

Chapter 5 describes the experiments of polarization-controlled octave-spanning supercontinuum generation in a photonic crystal fiber with dispersion-compensated femtosecond pulses from an ultrafast Ti:Sapphire laser. Background of supercontinuum generation will be reviewed. In addition, a polarization rotation system for supercontinuum laser source using dielectric mirrors to increase the repetition rate will be presented. The observation of polarization dynamics of the supercontinuum generation motivates further numerical investigations of the polarization dynamics of supercontinuum generation.

Chapter 6 presents numerical investigations for the polarization dynamics of the supercontinuum laser source. The detailed theoretical background and derivations of supercontinuum, including the nonlinear effects and polarization instability in birefringent fiber will be discussed in detail. The coupled nonlinear Schrödinger equations are numerically solved using the symmetric split-step Fourier method. The numerical algorithm using eigen-polarization basis switching will be presented as well as discussions and comparisons of the critical Raman response function including the anisotropic response part for modeling the supercontinuum.

Chapter 7 focuses on the analysis of the numerical simulation results for both linear and elliptical input polarizations for soliton fission and the polarization evolution of the Raman soliton. Polarization dynamics represented on the Poincaré sphere reveal the presence of a polarization separatrix and the emergence of stable slow and unstable fast eigen-polarizations for the Raman solitons ejected in the supercontinuum generation process. Circularly birefringent fiber is also investigated and found to simplify the nonlinear polarization dynamics. The circularly polarized Raman soliton in scupercontinuum generation could become a new stable, tunable, and broadband light source for polarization-sensitive optical imaging in a scattering medium.

Chapter 8 summarizes the thesis and provides an outlook for future research.

Chapter 2

Polarized light propagation in scattering medium

2.1 Motivation and challenges of optical imaging in scattering medium

Light is one of the most useful probe for investigating complex scattering media at the mesoscopic level. However, due to the inhomogeneous distribution of refractive index in complex medium such as biological tissues, multiple optical scattering can severely degrades optical image quality. The most common type of scattering medium is biological tissue. However, the issue of optical scattering exist not only in biomedical imaging, but also in transportation, navigation, forensic science, remote sensing and planetary atmospheric science, and some example environments are shown in Figure 2.1 (a) to (e). In this chapter, I review light propagation and interaction in optical scattering medium for biological tissues and compare optical absorption and scattering in a biological tissue model.

I first review to Mie and Rayleigh scattering and use the Mie scattering coefficients to derive and simulate the scattering probability function for various particle sizes. Polarization imaging in scattering medium is of special interest to my research. Stokes parameters and Mueller scattering matrix will be presented and previous research for polarimetry imaging in scattering medium including planet surface imaging will be analyzed. The Stokes parameters presented in the chapter forms the basic tools that will be used for the numerical simulation of polarization dynamics of light source using vectorized generalized nonlinear Schrödinger equations (GNLSE).

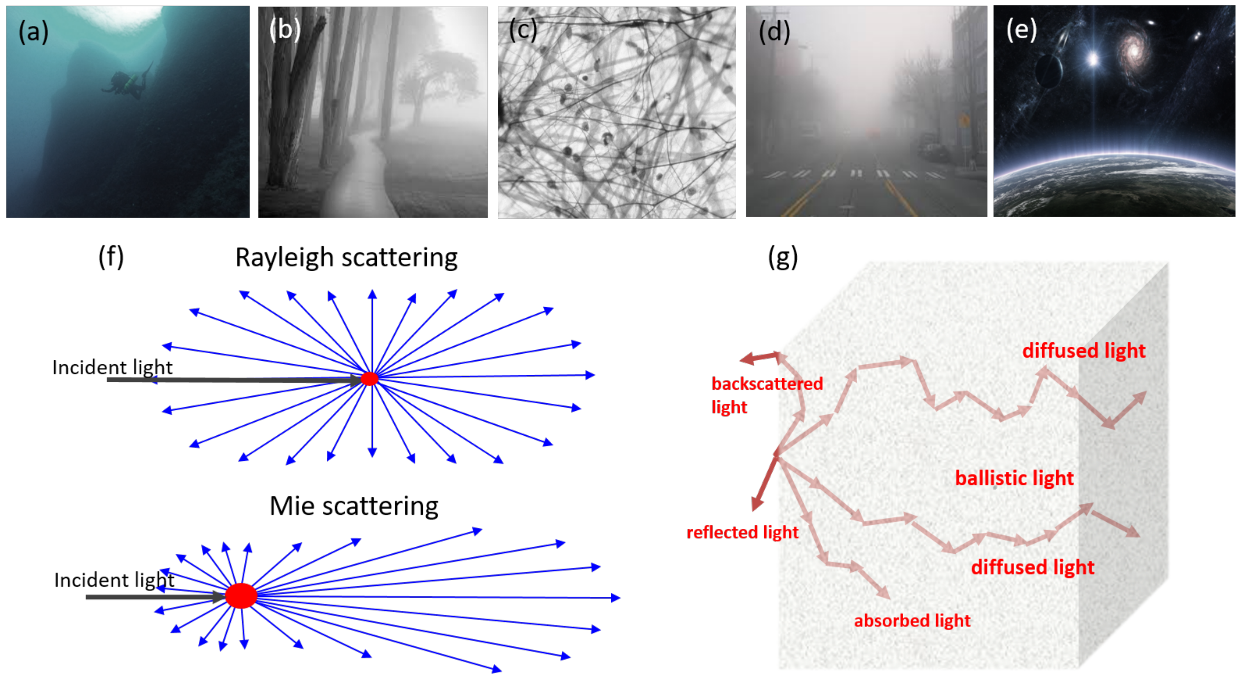

Figure 2.1: Scattering medium in nature. From (a) to (e): undersea water, fog in a forest, turbid biological tissue, smog in a city and remoate ssensing in atmospheric science. Small scale particle picture for two main types of scattering: (f) Rayleigh scattering for small particle and Mie scattering for large particle, (g) Cartoon illustrating possible photon propagation experience in a typical scattering and absorptive medium.

2.2 Overview of optical properties of scattering medium

Biological tissue is a highly heterogeneous and complex medium which can interact strongly with optical radiation. A biological tissue can be treated as a collection of scatterers, absorbers and sometimes even fluorophores. The average refractive index of biological tissues is typically higher than that of air which causes partial Fresnel reflection at the interface of tissue and air [24]. Due to the randomly varying size, shape and density of cell, fibers and organelles, the relative refractive index varies in space and time and this can significantly affect the propagation of light in such complex medium.

When propagating in a biological tissue, the optical wave can experience structures with dimensions ranging from the width of a protein macromolecule (typically 50 to 100 nm), to the diameter of the body of a biological cell (typically 2 to 50 μm), to the length of a blood vessel (typically $> 100\mu$m). Biological tissue can be viewed crudely as a material consisting of cells that reside in and attached to an extracellular matrix [25]. In terms of mass, most biological tissue generally consists of water (about 55 to 99%) and collagen (about 0 to 35%).Therefore, because most biological tissues consists of structures with varying sizes, it can be modeled as a random distribution of refractive index which varies spatially. Indeed, the choice of modeling biological tissue highly depends on the shape and structure of the tissue understudy, as well as the characteristic of lighting scattering in the tissue medium. Interestingly, it was demonstrated that the structure of the refractive index inhomogeneities in a variety of biological tissues resembles that of frozen turbulence in the atmosphere by using phase contrast microscopy [26]. The results obtained are fundamental for understanding light propagation in tissue and may provide clues about how tissues develop and organize.

For biological media that consists of discrete particles, such as blood, another approach for a tissue model is to represent the medium as a collection of discrete scattering particles. In particular, for blood cells the shapes are very similar to spheres or ellipsoids, hence the Mie theory can be used to describe the diffraction of light from these spherical particles[27, 28].

2.2.1 Optical scattering and absorption

When interacting with particles in a scattering medium, the incident photon can experience various possibilities. As shown in Figure 2.1 (g), it can be reflected, back-scattered, multi-scattered, absorbed, red-shifted (fluorescent) or transmitted without having been scattered. When a light beam propagates in a thin layer of tissue medium with thickness d, the transmitted intensity obeys the exponential Bouguer-Beer-Lambert law which is given by [29]:

$$I_{trans}(d) = (1 - R_F) I_{in} e^{-\mu_t d} \tag{2.1}$$

where $I_{trans}(d)$ is the intensity of transmitted light (W/cm^2), R_F is the Fresnel reflection coefficient (Note when the light beam is at normal incidence, $R_F = (\frac{n-1}{n+1})^2$, where n is the relative average refractive index of the tissue medium), I_{in} is the incident light intensity (W/cm^2), and the extinction coefficient μ_t (cm^{-1}) is given by $\mu_t = \mu_a + \mu_s$. μ_t is also referred to as the total attenuation coefficient. Optical absorption in biological tissue originates mainly from hemoglobin, melanin and water, and it can be represented by the absorption coefficient μ_a, which is defined as the probability of photon absorption in a medium per path length. (In an absorption dominated medium, the optical radiation is attenuated obeying $\frac{dI_{in}}{z} = -\mu_a I_{in}$, and z is the distance of light propagation. Hence, optical absorption exponentially attenuate the optical radiation given by Beer's law: $I_{tr}(z) = I_{in}e^{-\mu_a z}$ and $l_a = \frac{1}{\mu_a}$, where I_{tr} is the transmitted intensity after going through the absorptive medium, and l_a is the mean absorption length which represents the average distance traveled by a photon before being absorbed.) However, most biological tissues are instead dominated by strong optical scattering because the optical absorption is relatively weak in the absorption window of 600 - 1350 nm [4].

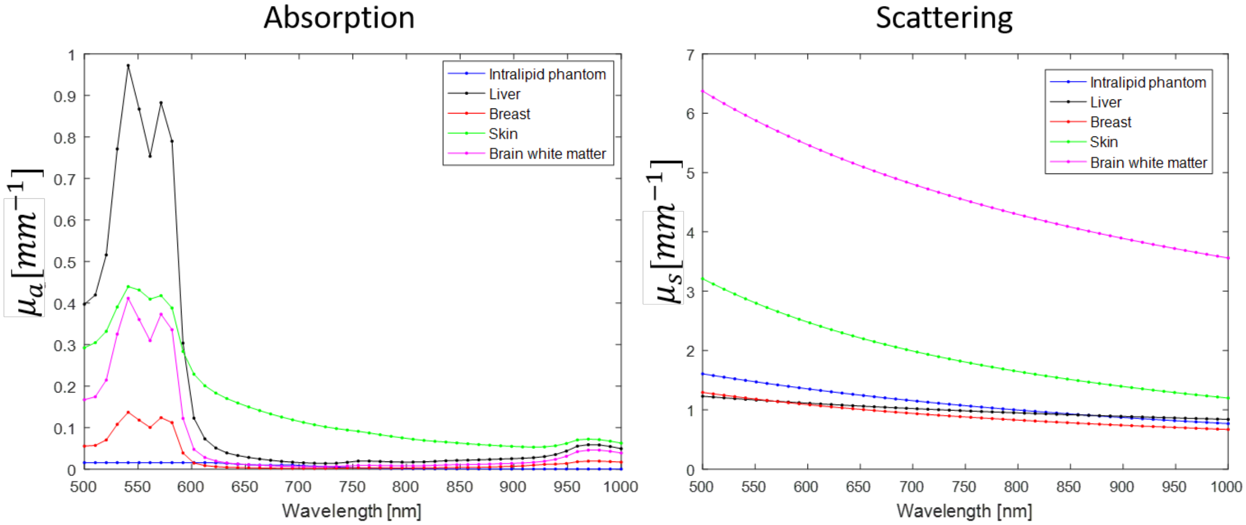

Figure 2.2: Absorption and reduced scattering coefficients for various tissue types. Results are simulated using software developed at Beckman laser institute.

Optical scattering is represented by the scattering coefficient μ_s, which is defined as the probability of photon scattering in a medium per path length. Similar to optical absorption, optical scattering exponentially reduces the transmitted optical intensity given by Beer's law: $I_{tr} = I_{in}e^{-\mu_s l}$ and $l_s = \frac{1}{\mu_s}$, where l_s is the scattering mean free length. In the presence of both absorption and scattering, the mean free path between interactions in the tissue medium is given by $l_{ph} = \frac{1}{\mu_t}$. The average scattering cross section per scattering particle is given by [30]: $\sigma_{sc} = \frac{\lambda^2}{2\pi}\frac{1}{I_{in}}\int_0^{\pi} I(\theta)sin\theta d\theta$, where I_{in} is the intensity of the incident light, $I(\theta)$ is the intensity of the angular distribution of the scattered light, and θ is the scattering angle. Note for isotropic scattering, σ_{sc} is independent of the polarization and direction of the incident light. Another important parameter of scattering is the anisotropy factor g, which is the mean cosine of the scattering angle θ given by,

$$g = \langle cos(\theta)\rangle = \int_0^{\pi} p(\theta)\ cos(\theta)\ 2\pi\ sin(\theta)\ d\theta \tag{2.2}$$

where $\langle\ \rangle$ is the expectation value operator, $p(\theta)$ is the so called phase function and represents the probability of being scttered by an angle θ (which can be approximated with Henyey-Greenstein function) and it depends on the scattering angle. g varies between -1 and 1. $g = 0$ represents isotropic (Rayleigh) scattering, $g = 1$ represents total forward (Mie) scattering, and $g = -1$ represents total backward scattering. Most biological tissue is forward scattering which means g is around 0.7 - 0.9. Given g, the reduced scattering coefficient including the effect of g can be written as,

$$\mu_s^{`} = \mu_s(1-g) \tag{2.3}$$

$$l_s^{`} = \frac{1}{\mu_s^{`}} \tag{2.4}$$

where $l_s^{`}$ is the transport scattering length, which represents the propagation distance of collimated light beam travels in a scattering medium before becoming isotropically distributed with uniform probability of propagating in any direction [31].

As shown in Figure 2.2, the scattering coefficient decreases as wavelength increases. With increasing Rayleigh scattering, the reduced scattering coefficient is enhanced more in the short wavelength. Comparing the absorption and scattering, scattering has a much larger influence for light-tissue interaction than absorption in the optical window of 600 to 1200 nm. As an example, light will be mostly scattered after going through two to three transport scattering lengths. Notice both scattering and absorption are wavelength dependent in a biological tissue. However, absorption is low in red and NIR wavelengths (650 nm to 1100 nm) where scattering has the dominating magnitude, i.e. $\mu_s' \gg \mu_a$. For the wavelength windows of 450 nm to 650 nm in the plot, we see $\mu_s' \sim \mu_a$. (As can be seen later in Figure 2.3, the typical reduced scattering length in biological tissue is 10^1 - 10^2 cm around the visible and near infrared wavelength region, while the typical absorption length is 10^{-3} - 10^1 cm in the same wavelength region.) Hence, optical scattering is often the most dominating and challenging problem for light propagation in biological tissue.

Despite the extreme diversity and structural complexity of biological tissue, from an optics point of view, biological tissue can be broadly classified to highly scattering (such as brain, skin, blood, breast, vessel wall and lymph) and weakly scattering tissues (crystalline lens, cornea and vitrorous humor). In a highly scattering medium, photons that experience multiple-scattering are referred to as diffused photons while in a weakly scattering medium, photons that experience no scattering are referred to as ballistic photons. There has been significant progress made to combat the scattering problem for imaging in turbid medium.

2.3 Polarized light in scattering medium

In the previous section, we considered the fundamentals of light propagation in scattering and absorptive medium. However, we assumed isotropic scattering medias. The vectorial nature of light can also play a role in optical imaging and light transportation in a scattering medium. Many researchers have assumed that photons become quickly depolarized in a random scattering medium. However, even in a relatively thick tissue structure, the degree of polarization (DoP) can still be measured for a wide variety of tissue types, such as eye cornea, cartilage, superficial skin tissue, tendon, collagen fibers, bone, nerves, teeth, myelin, and mucous membrane [5].

Many biological tissues are optically anisotropic because of the form birefringence of certain fibrous structures that form the extracellular medium. Form birefringence can be caused by the parallel cylinders in some tissue which effectively form a uniaxial optically birefringent structure, which can modify the state of polarization (SoP) of light as it propagates through these tissues. In addition the depolarization of light as it propagate through certain tissues can reveal interesting structural informations, by manipulating the degree of polarization (DoP) of the incident light, some particular SoPs can be maintained better than depolarized or other SoPs for light propagation in scattering medium.

2.3.1 Mie scattering and Rayleigh scattering

The Rayleigh and the Mie theory can be used to model the scattering of a plane monochromatic wave by a single particle. However, Rayleigh theory models the scattering of incident light by particles much smaller than the wavelength. Mie theory is applicable to isotropic particles of any size [4].

By taking into account the Mie and Rayleigh scattering and absorption in the tissue, a realistic and generic tissue model can be represented as shown in Figure 2.3. As shown in the figure, the average blood volume fraction is 0.2%. The total fat and water volume fraction is 70% and the volume fraction of fibrous material is about 30%. Note as the fat content changes from 70% to 0% by 10%, the water content changes from 0% to 70% by 10%. In Figure 2.3b), the generic effective scattering coefficient is plotted. The scattering due to Mie scattering is represented as blue lines. Then the scattering due to Rayleigh scattering is added to the model and are shown as red lines. The wavelength dependence of the scattering coefficient can be described in terms of contributions from both Mie and Rayleigh scattering [32]. It can be represented by the following equation which was obtained by fitting to the experimental data for several type of tissues including dermis, epidermis, bone, breast, liver, brain, cortex, heart wall, kidneys, lung and whole blood [33, 34, 35, 36]:

$$\mu_s{}'(\lambda) = a'\left(f_{Rayleigh}\left(\frac{\lambda}{500(nm)}\right)^{-4} + (1 - f_{Rayleigh})\left(\frac{\lambda}{500(nm)}\right)^{-b_{Mie}}\right) \tag{2.5}$$

where $\mu_s{}'$ is the reduced scattering coefficient, λ is the wavelength, a' is a scaling factor, b_{Mie} is the scattering power of Mie scattering. In particular, b_{Mie} describes the wavelength dependence of the reduced scattering coefficient $\mu_s{}'$, and the typical value of b_{Mie} for skin it is between 0.7 and 2.5, for brain it is between 0.3 and 3.2, for bone is between 0.1 and 1.4 [32, 34, 33, 36]. This equation provides a good fit to wavelength dependence of the scattering coefficient of biological tissue scattering for studying the behavior of light diffusion in the optical window of 400 to 1300 nm, particularly for skin, brain, breast, bone, fibrous tissues and fatty tissues [32].

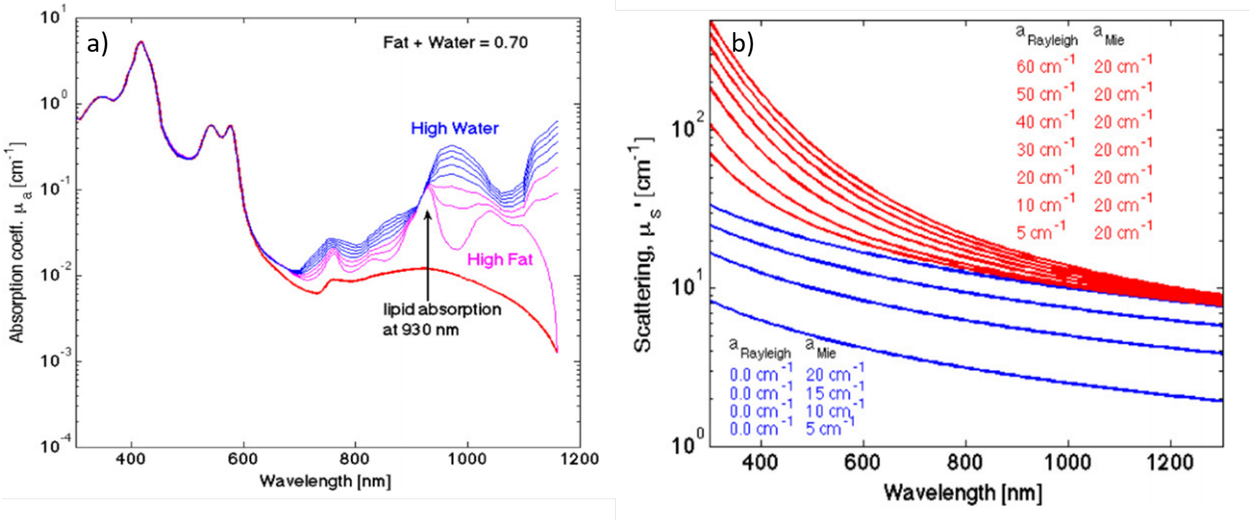

Figure 2.3: Absorption and reduced scattering coefficients for a generic tissue model. a) Absorption coefficient. Red lines: oxygenated blood, pink lines: high fat, blue line: high water. b) Reduced scattering coefficient. Blue lines: Mie scattering, red lines: Mie and Rayleigh scattering. Adapted from [32].

Following [37], Rayleigh theory can be summarized as the follows. If we assume a linearly polarized incident field plane wave propagating in z with the transverse electric field in the x-y plane,

$$\vec{\mathbf{E}}_0(x, y, z, t) = (E_x\hat{x} + E_y\hat{y})e^{i(\omega t - kz)} \tag{2.6}$$

where $\vec{\mathbf{E}}_0$ is the incident electrical field phasor, ω is angular frequency, $k = \frac{\omega}{c}$ is the wave vector and t is time, then the induced oscillating dipole moment can be written as,

$$\vec{\mathbf{p}} = \bar{\alpha}\vec{\mathbf{E}}_0(x, y, z, t) = \begin{pmatrix} \alpha_{xx} & \alpha_{xy} \\ \alpha_{yx} & \alpha_{yy} \end{pmatrix} \begin{pmatrix} E_x\hat{x} \\ E_y\hat{y} \end{pmatrix} e^{i(\omega t - kz)} + c.c. \tag{2.7}$$

where $\bar{\alpha}$ represents polarizability tensor of the particle which is the proportionality between the dipole moment $\vec{\mathbf{p}}$ and incident the electric field $\vec{\mathbf{E}}_0$, $k = \frac{2\pi n}{\lambda}$ is the propagation constant in the medium, n is the refractive index of the medium and λ is the wavelength in vacuum. The components of the polarizibility tensor $\bar{\alpha}$ may depend on frequency and maybe complex. The electric field of the scattered light in the far field is [4, 37],

$$\vec{E}_{sc}(\vec{r},t) = \frac{e^{-ikr}}{4\pi r}\frac{k^2|\vec{p}|sin\gamma}{r}\hat{p}e^{i\omega t} + c.c. \tag{2.8}$$

where γ is the angle between the direction of the scattered light and the direction of the dipole oscillation. Therefore, the intensity of the scattered light can be derived as,

$$I_{sc} = \frac{|\vec{E}_{sc}|^2}{\eta_0/n} = \frac{k^4|\vec{p}|^2 sin^2\gamma}{16\pi^2 r^2} = \frac{k^4|\alpha|^2 sin^2\gamma}{16\pi^2 r^2}I_0 \tag{2.9}$$

where I_0 is the intensity of the incident light, η_0 is the impedence of free space and n is the refractive index. On the other hand, Mie theory is a rigorous solution of Maxwell's equation for a plane wave scattered by a sphere. Mie scattering can model the scattering of light from particle of any size with plane wave illumination. The particle should be isotropic and homogeneous. The plane wave assumption is valid when the particle and the wavelength are both much smaller than the wavefront. The derivation of Mie theory should include solving the Maxwell's equations for fields both inside and outside the sphere and then apply boundary conditions to solve for the undetermined Mie coefficients for the solutions from the Maxwell's equations. To gain physical insights to how the scattering behaves as the size and optical properties of the particle and its surrounding environment varies, the expressions for the Mie scattering coefficients should be explained. The Mie scattering coefficients are represented as a_n and b_n respectively and are defined as [30],

$$a_n = \frac{m\psi_n(ms)\psi_n'(s) - \psi_n(s)\psi_n'(ms)}{m\psi_n(ms)\xi_n'(s) - \xi_n(s)\psi_n'(ms)} \tag{2.10}$$

$$b_n = \frac{\psi_n(ms)\psi_n'(s) - m\psi_n(s)\psi_n'(ms)}{\psi_n(ms)\xi_n'(s) - m\xi_n(s)\psi_n'(ms)} \tag{2.11}$$

The a_n and b_n coefficients will be used to solve the scattering functions S_{sc1} and S_{sc2} in Eqn 2.24. Note m is the refractive index of the sphere relative to the background medium, s is the size parameter defined as $s = ka$, a is the radius of the sphere and k is the wave number and,

$$\psi_n(ms) = msj_n(ms) \tag{2.12}$$

$$\xi_n(s) = sh_n^{(1)}(s) \tag{2.13}$$

$$h_n^{(1)}(kr) = j_n(kr) + y_n(kr) \tag{2.14}$$

where r is the radius in spherical coordinates. Furthermore,

$$h_n^{(1)}(kr) = j_n(kr) + iy_n(kr) \tag{2.15}$$

is the spherical Hankel function and

$$j_n(kr) = \sqrt{\frac{\pi}{2kr}} J_{n+0.5}(kr) \tag{2.16}$$

$$y_n(kr) = \sqrt{\frac{\pi}{2kr}} Y_{n+0.5}(kr) \tag{2.17}$$

are the spherical Bessel functions, and J and Y are the Bessel functions of the first and second kind evaluated at half integral order.

In general, there are two more Mie coefficients c_n and d_n, however they're needed only when the electric field inside the particle is of interest, hence only a_n and b_n is needed for the Mie simulation model that will be investigated in the next section. For optical imaging in scattering medium shown in Fig 2.1, it becomes crucial to obtain a theoretical model to investigate the scattering behaviors from various particle sizes and refractive indexes. From Mie theory, the detailed shape of the angular scattering pattern can be visualized. This is a useful tool to gain insights to the scattered far field diagram as a function of particle size and the relative refractive index to the background medium. The scattering probability function can be used to infer the size of the scattering particles in biological tissue, under-sea, smog and atmosphere of planets. In the next section, the derivation of the angular scattering functions will be discussed using the Mie coefficients and the scattering probability functions will be plotted for single particles with various sizes and index of refractions.

2.3.2 Theory of polarized light propagation in scattering medium

To completely understand the scattering effects, Maxwell's equations and the resulting vector wave equations are a good starting point for the rigorous electromagnetic wave modeling of the scattering from an atomic dipole or spherical particle although scattering from arbitrary shaped nano-particles is challenging to model rigorously. When extending this analysis to scattering from dense distributions of randomly shaped particles as encountered in tissue, ocean or atmosphere, then various statistical averaging techniques will need to be employed. Hence we begin here with the single particle case. Electromagnetic radiation obey the vector wave equations and can be written as,

$$\nabla^2 \mathbf{E} + k^2 \mathbf{E} = 0 \tag{2.18}$$

$$\nabla^2 \mathbf{H} + k^2 \mathbf{H} = 0 \tag{2.19}$$

where k is the wave number $k^2 = \omega^2 \epsilon \mu$, ϵ is the electric permittivity, and μ is the magnetic permeability. $\mathbf{E}$ and $\mathbf{H}$ represents the spatial-temporally varying electric and magnetic vector fields, respectively.

When a monochromatic plane wave of light is incident on a single particle, a scattering field will be produced and the direction of scattering can be defined as θ and ϕ. The scattering geometry and coordinate system is plotted in Figure 2.4. A particle scatters a polarized incident plane wave where z is defined by the propagation direction of the incident light. The $\hat{x}$, $\hat{y}$ and $\hat{z}$ are the orthogonal basis vectors in the positive x, y and z Cartisian coordinates. The scattering plane is defines by the scattering direction $\hat{k}_r$ and the forward light propagation direction $\hat{z}$. The electrical field of the incident wave can be written as,

$$\mathbf{E_i} = \mathbf{E_{\|i}} + \mathbf{E_{\perp i}} = E_{\|i}\ \hat{\mathbf{k}}_{\|i} + E_{\perp i}\ \hat{\mathbf{k}}_{\perp i} \tag{2.20}$$

where $\mathbf{E_{\|i}}$ is the parallel and $\mathbf{E_{\perp i}}$ is the perpendicular component of the incident electric field to the scattering plane, respectively. $\hat{\mathbf{k}}_{\|i}$ and $\hat{\mathbf{k}}_{\perp i}$ are the orthogonal basis vectors defined as parallel and perpendicular to the scattering plane respectively (shown in Figure 2.4). Hence, $\hat{\mathbf{k}}_{\|i} = \frac{\hat{\mathbf{z}} \times \hat{\mathbf{k}}_{\perp i}}{|\hat{\mathbf{z}} \times \hat{\mathbf{k}}_{\perp i}|}$, and $\hat{\mathbf{k}}_{\perp i} = \frac{\hat{\mathbf{z}} \times \hat{\mathbf{k}}_r}{|\hat{\mathbf{z}} \times \hat{\mathbf{k}}_r|}$. Then the relationship between the scattered and the incident electric field can be derived as the following [30, 38, 39, 40, 41, 5, 42]:

$$\begin{pmatrix} \mathbf{E_{\|sc}} \\ \mathbf{E_{\perp sc}} \end{pmatrix} = \frac{e^{ikr}}{-ikr} \bar{\bar{\mathbf{S}}}_{sc}\ \mathbf{E_i} = \frac{e^{ikr}}{-ikr} \begin{pmatrix} S_{sc2} & S_{sc3} \\ S_{sc4} & S_{sc1} \end{pmatrix} \begin{pmatrix} E_{\|i} \\ E_{\perp i} \end{pmatrix} \tag{2.21}$$

where r is the distance from the single scatterer to the detector, n is the index of refraction of

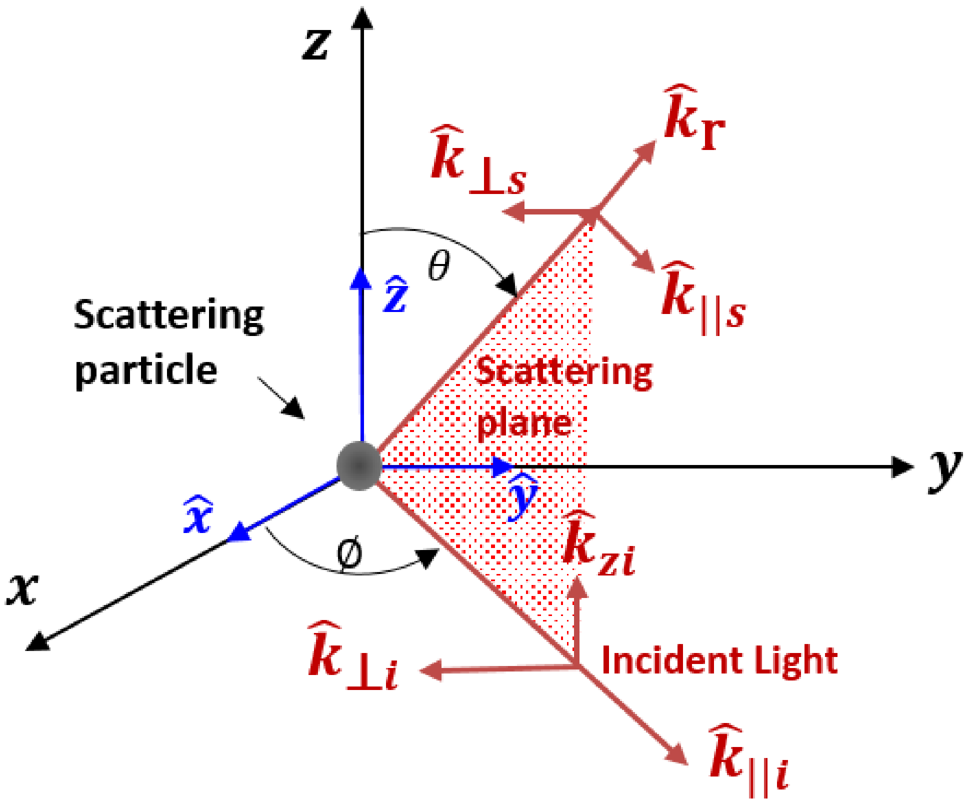

Figure 2.4: Scattering coordinate system. $(\hat{x}, \hat{y}, \hat{z})$ is the orthogonal basis vector along Cartisian coordinate system of (x, y, z). The incident propagates in the $\hat{k}_{zi}$ direction, $\hat{k}_{\perp i}$ and $\hat{k}_{||i}$ are the orthogonal basis vectors for the incident light, and . The scattering particle is located at the origin of (x, y, z). $\hat{k}_r$ is the scattering direction, $\hat{k}_{\perp s}$ and $\hat{k}_{||s}$ are the orthogonal basis vectors for the scattered light. θ is the scattering angle and ϕ is the azimuthal angle.

the scattering medium. The complex scattering matrix is given by $\bar{\bar{\mathbf{S}}}_{sc} = \begin{pmatrix} S_{sc2} & S_{sc3} \\ S_{sc4} & S_{sc1} \end{pmatrix}$. The two angular scattering functions S_{sc1} and S_{sc2} describe the scattered field $\mathbf{E_{sc}}$. Hence the vector scattered far field in spherical coordinates is given by,

$$E_{s\theta}(r, \theta, \phi) = \frac{e^{ikr}}{-ikr}\ cos\phi\ S_{sc2}(cos\theta) \tag{2.22}$$

$$E_{s\phi}(r, \theta, \phi) = \frac{e^{ikr}}{ikr}\ sin\phi\ S_{sc1}(cos\theta) \tag{2.23}$$

while the scattering functions can be written as the following,

$$S_{sc1}(cos\theta) = \sum_{n=1}^{\infty} \frac{2n+1}{n(n+1)}(a_n \pi_n + b_n \tau_n) \tag{2.24}$$

$$S_{sc2}(cos\theta) = \sum_{n=1}^{\infty} \frac{2n+1}{n(n+1)}(a_n \tau_n + b_n \pi_n) \tag{2.25}$$

π_n and τ_n are defined as [30],

$$\pi_n = \frac{2n-1}{n-1}\ cos(\theta)\pi_{n-1} - \frac{n}{n-1}\ \pi_{n-1} \tag{2.26}$$

$$\tau_n = n\ cos(\theta)\ \pi_n - (n+1)\ \pi_{n-1} \tag{2.27}$$

Because we know the Mie coefficients a_n and b_n coefficients from Eqn. 2.10, the scattering amplitudes $S_{sc1}(\theta)$ and $S_{sc2}(\theta)$ can be solved. Once $S_{sc1}(\theta)$ and $S_{sc2}(\theta)$ are known, the probability of scattering at an angle can be calculated after converting the amplitude scattering functions to flux scattering functions by magnitude squaring the complex amplitude. The scattering probability functions can be simulated using MATLAB [43]. I extended the original MATLAB program by including both the parallel and perpendicular polarization scattering probability functions instead of only the unpolarized one. The simulated angular scattering probability functions are plotted in Figure. 2.5 a) to f), for spherical particle sizes of 10 nm, 50 nm, 100 nm, 200 nm, 300 nm and 1000 nm, it results in size parameter of $s = 0.148938$ to 14.8938 ($s = \frac{2\pi ma}{\lambda}$, where m is the relative refractive index and a is radius of the particle.) The incident wavelength is 632.8 nm and the relative refractive index is assumed to be 1.5 for the spheres and the surrounding environment. As can be seen, the scattering probability functions depend on both the size of the particle relative to the wavelength and the relative refractive index. The scattering functions for parallel (red lines), perpendicular (blue lines), and average or unpolarized (black lines) polarized light are plotted for various real relative refractive indexes and particle sizes. We see in a) for a very small particle, the normalized angular scattering for unpolarized illumination is more isotropic while the scattering probability functions for the perpendicular and the parallel polarizations are distinct. The backscattering for the unpolarized, perpendicular and parallel cases is more pronounced. While for a larger particle as shown in c), d), e) and especially f), the two orthogonal polarization scatterings

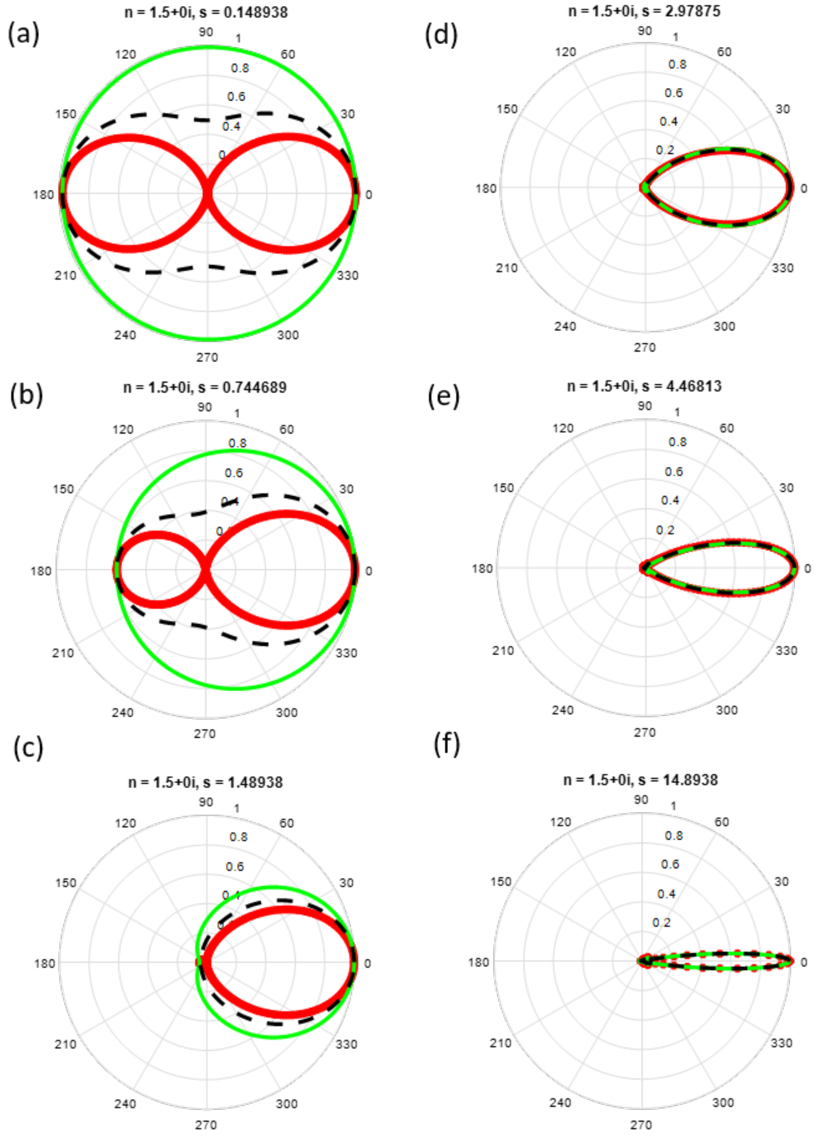
(a) n = 1.5+0i, s = 0.148938

(b) n = 1.5+0i, s = 0.744689

(c) n = 1.5+0i, s = 1.48938

(d) n = 1.5+0i, s = 2.97875

(e) n = 1.5+0i, s = 4.46813

(f) n = 1.5+0i, s = 14.8938

Figure 2.5: Scattering probability function simulation for parallel (red line), perpendicular (green line) and unpolarized light (black dashed line) for various particle sizes. As the particle size increases from 10 nm, 50 nm, 100 nm, 200 nm, 300 nm to 1000 nm relative to the wavelength of 632 *nm*, the scattering probability becomes more concentrated in the forward direction for both parallel and perpendicular polarizations.

are nearly indistinguishable and forward-scattering dominants over back-scattering. The amount of back-scattering for this case is very small compared to the more isotropic scattering environment shown in a) for unpolarized illumination.

2.4 Polarization imaging in scattering medium using Stokes parameters and Mueller scattering matrix

Besides wavelength, coherence and intensity, polarization is one of the primary physical quantities associated with light. Polarization information using polarimetric imaging can reveal details about surface features, shape, shading and roughness with high contrast, which is largely uncorrelated with spectral or intensity images [44]. Polarization imaging has been demonstrated to be a powerful method to improve image contrast, aid with navigation, improve under-sea imaging, investigate biological tissue properties, and identify targets in scattering environments. Polarimetric observations of the atmosphere and surface feature of the planets including Venus, Mars, Jupiter and Earth has been investigated since late 1960s. A first and most extensive set of polarized images of the Earth was obtained from space in 1986 using remote sensing polarization experiment [48]. By measuring and computing the Stokes parameters, a more distinct surface properties of the Earth was imaged in degree of polarization rather than in conventional intensity image alone. As shown in Figure 2.6, using earth based polarimetric telescopes, the research demonstrated a

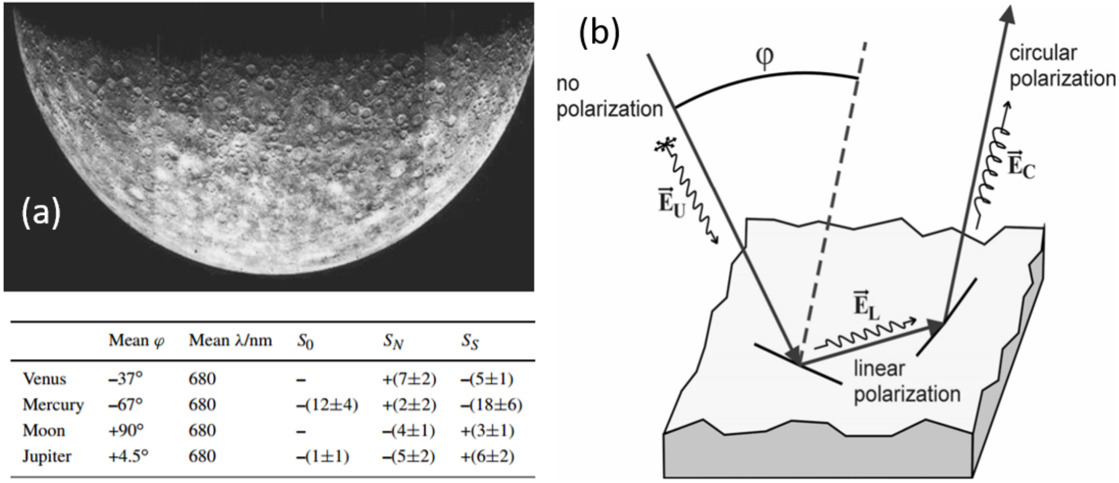

	Mean φ	Mean λ/nm	S_0	S_N	S_S
Venus	–37°	680	–	+(7±2)	–(5±1)
Mercury	–67°	680	–(12±4)	+(2±2)	–(18±6)
Moon	+90°	680	–	–(4±1)	+(3±1)
Jupiter	+4.5°	680	–(1±1)	–(5±2)	+(6±2)

Figure 2.6: Polarimetric imaging for investigations of planets using Stokes parameter measurements. (a) Image of southern hemisphere of Mercury taken in 1974 by NASA spacecraft Mariner 10, adapted from [45]. (b) Fraction of circular polarization generated from unpolarized illumination, adapted from [46]. Table: degree of polarization, adapted from [47]

high resolution optical polarimeter to determine and map the circular polarization scattered from the surface of Mercury by imaging the planet's surface using unpolarized illumination from the sun. The polarimeter is capable of detecting the enantiomorphism of surface crystal and mineral if combined with an *in situ* sensor.

Scattering poses a challenge for optical imaging in scattering environments such as fog, underwater, atmosphere and biological tissues. It is thus critical for an imaging system to discriminate a target from the background scene or to increase depth of sensing in the scattering medium. The many real world applications includes optical imaging, coherence tomography, discrimination of short-path photons in a highly scattering environment, enhancing detection range in scattering medium and imaging objects in turbid media. In this section, I will focus on polarization imaging in scattering media by reviewing and discussing various types of polarization imagers.

2.4.1 Contrast improvement with variable polarizer

The simplest type of imaging polarimetry is a one-dimensional polarimeter that has been investigated for under-water imaging to suppress scattering using linear and circular polarizers for both unpolarized and polarized illumination. The one-dimensional means only one polarizer is used in front a camera. Then we can adjust the polarization state of the polarizer to maximize the contrast between the object and the background, which is often used in photography. Note depending on the scattering environment, either circular or linear polarizer can be used, and the state of polarization should be orthogonal to the polarization of the background in order for it to optimize the contrast of the object to the background.

2.4.2 Full Mueller matrix imaging polarimetry

While Jones vector represents polarization assuming pure polarized light (DoP = 1), Stokes parameter provide an even more useful tool for a systematic analysis of both the state of polarization and degree of polarization. The Stokes parameters may be determined from experiments. Polarimeters based on intensity measurements of polarized light more often uses Stoke parameters which is given by the following,

$$\mathbf{S} = \begin{pmatrix} S_0 \\ S_1 \\ S_2 \\ S_3 \end{pmatrix} = \begin{pmatrix} I_H + I_V \\ I_H - I_V \\ I_{+45} - I_{-45} \\ I_{RHC} - I_{LHC} \end{pmatrix} = \begin{pmatrix} \langle E_H E_H^* + E_V E_V^* \rangle \\ \langle E_H E_H^* - E_V E_V^* \rangle \\ \langle E_H E_V^* + E_V E_H^* \rangle \\ \langle i(E_H E_V^* - E_V E_H^*) \rangle \end{pmatrix} \tag{2.28}$$

where S_0, S_1, S_2 and S_3 are the Stokes parameters satisfying $S_0^2 \leq S_1^2 + S_2^2 + S_3^2$, and S_0 represents the intensity of the light. E_H and E_V are the stochastically time varying horizontal and vertical electric field components with respect to the laboratory x, y, z frame, and $<>$ is an expectation value computed with a time average. The $*$ sign indicates the complex conjugate and the angle brackets represents time averages. The measurement of the Stoke parameter can be obtained with 6 independent intensity measurements using 4 linear polarization analyzers to obtain I_H, I_V, I_{+45}, I_{-45}, and 2 circular polarizers to obtain I_{RHC} and I_{LHC}, respectively. Jones vector $\mathbf{J}$ and Stokes parameter $\mathbf{S}$ are related by $\mathbf{S} = \mathbf{J}^* \bar{\bar{A}}_i \mathbf{J}$, where $\bar{\bar{A}}_i = \begin{pmatrix} 1 & 0 \\ 0 & 1 \end{pmatrix}, \begin{pmatrix} 1 & 0 \\ 0 & -1 \end{pmatrix}, \begin{pmatrix} 0 & 1 \\ 1 & 0 \end{pmatrix}, \begin{pmatrix} 0 & -i \\ -i & 0 \end{pmatrix}$, and $*$ represent complex conjugate. (For monochromatic plane wave traveling in the z direction, its complex envelopes can be written as $E_x = a_x e^{i\phi_x}$ and $E_y = a_y e^{i\phi_y}$ for the x and y components. The complex fields can be written in the form of Jones vector as $\mathbf{J} = \begin{pmatrix} E_x \\ E_y \end{pmatrix}$.) In addition, the DoP can be represented in terms a Stokes parameter as,

$$DoP = \frac{\sqrt{S_1^2 + S_2^2 + S_3^2}}{S_0} \tag{2.29}$$

$DoP = 1$ for polarized light, $DoP < 1$ for partially polarized light, $DoP = 0$ for completely unpolarized light. Furthermore, the degree of linear polarization (DoP_L) and the degree of circular polarization (DoP_C) can be defined as:

$$DoP_L = \frac{\sqrt{S_1^2 + S_2^2}}{S_0} \tag{2.30}$$

$$DoP_C = \frac{S_3}{S_0} \tag{2.31}$$

On the other extreme, a complicated polarimetry imaging method can be applied to measure all the 16 elements in the Mueller matrix (or a subset of the matrix for the back-scattered light). The controlled light source generates a combination of state of polarizations and the detector is configured to measure the full Stokes parameter (or a subset of it). For the most sophisticated type of Mueller imaging polarimeter, the Mueller matrix is measured for each pixel for the light reflected or back-scattered. The polarization of the scattered light in the far field can be described by the Mueller matrix M_{sc} that transforms the incident to the scattered Stokes parameters,

$$\mathbf{S_{out}} = \mathbf{M_{sc}S_{in}} = \begin{pmatrix} M_{11} & M_{12} & M_{13} & M_{14} \\ M_{21} & M_{22} & M_{23} & M_{24} \\ M_{31} & M_{32} & M_{33} & M_{34} \\ M_{41} & M_{42} & M_{43} & M_{44} \end{pmatrix} \begin{pmatrix} S_0 \\ S_1 \\ S_2 \\ S_3 \end{pmatrix} = \begin{pmatrix} S_{0out} \\ S_{1out} \\ S_{2out} \\ S_{3out} \end{pmatrix} \tag{2.32}$$

where $\mathbf{S_{in}}$ is the input Strokes parameter and $\mathbf{M_{sc}}$ is the Mueller scattering matrix [30] and its components are related to the scattering matrix components (S_{sc1}, S_{sc2}, S_{sc3} and S_{sc4}) in Eqn 2.21 by the following,

$$\begin{aligned}
&M_{11} = \frac{1}{2}(|S_{sc1}|^2+|S_{sc2}|^2+|S_3sc3|^2+|S_{sc4}|^2), \quad M_{12} = \frac{1}{2}(|S_{sc2}|^2-|S_{sc1}|^2+|S_{sc4}|^2-|S_{sc3}|^2) \\
&M_{13} = Re\left\{S_{sc2}S_{sc3}^* + S_{sc1}S_{sc4}^*\right\}, \quad M_{14} = Im\left\{S_{sc2}S_{sc3}3^* - S_{sc1}S_{sc4}^*\right\} \\
&M_{21} = \frac{1}{2}(|S_{sc2}|^2-|S_{sc1}|^2-|S_{sc4}|^2-|S_{sc3}|^2), \quad M_{22} = \frac{1}{2}(|S_{sc2}|^2+|S_{sc1}|^2-|S_{sc4}|^2-|S_{sc3}|^2) \\
&M_{23} = Re\left\{S_{sc2}S_{sc3}^* - S_{sc1}S_{sc4}^*\right\}, \quad M_{24} = Im\left\{S_{sc2}S_{sc3}^* + S_{sc1}S_{sc4}^*\right\} \\
&M_{31} = Re\left\{S_{sc2}S_{sc4}^* + S_{sc1}S_{sc3}^*\right\}, \quad M_{32} = Re\left\{S_{sc2}S_{sc4}^* - S_{sc1}S_{sc3}^*\right\} \\
&M_{33} = Re\left\{S_{sc1}S_{sc2}^* + S_{sc3}S_{sc4}^*\right\}, \quad M_{34} = Im\left\{S_{sc2}S_{sc1}^* + S_{sc4}S_{sc3}^*\right\} \\
&M_{41} = Im\left\{S_{sc2}^*S_{sc4} + S_{sc3}^*S_{sc1}\right\}, \quad M_{42} = Re\left\{S_{sc2}S_{sc4}^* - S_{sc1}S_{sc3}^*\right\} \\
&M_{43} = Im\left\{S_{sc1}S_{sc2}^* - S_{sc3}S_{sc4}^*\right\}, \quad M_{44} = Re\left\{S_{sc1}S_{sc2}^* - S_{sc3}S_{sc4}^*\right\}
\end{aligned} \tag{2.33}$$

Usually all the 16 elements of scattering matrix should be measured in order to completely characterize the effect that scattering sample has on various input states of polarization in order to characterize its physical properties. Generally this would require exciting the scattering sample

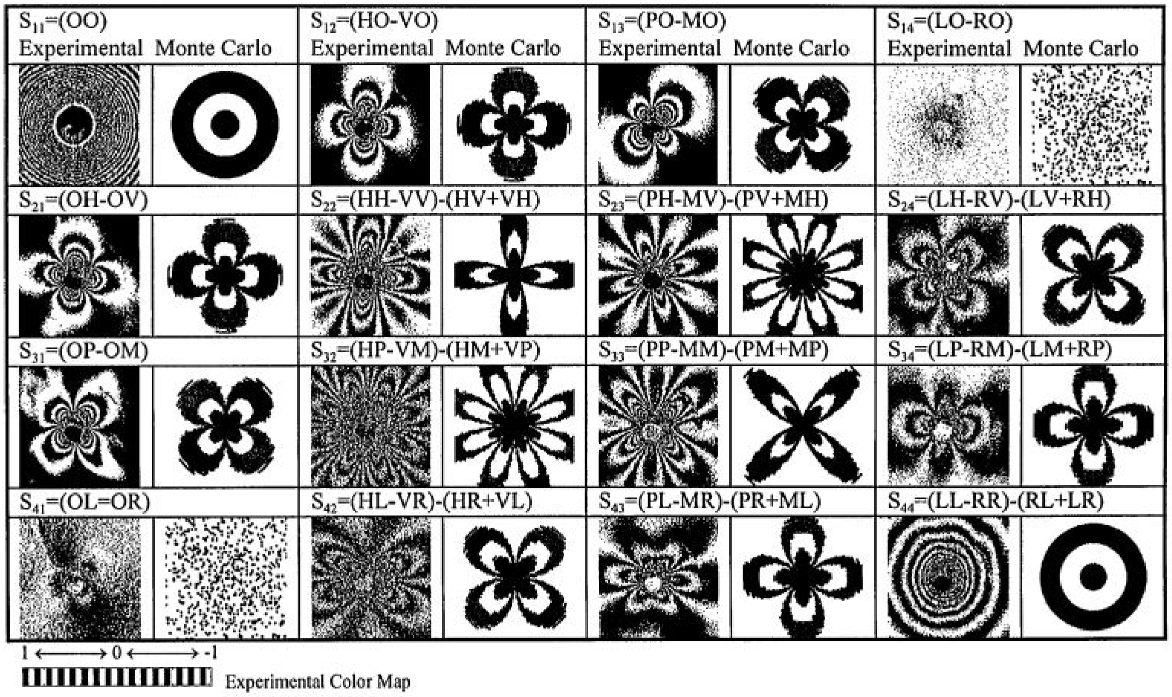

Figure 2.7: Experimental and Monte Carlo Mueller scattering matrix. Each image size is about $1.6cm \times 1.6cm$. Each individual image is represented by a combination of two letters which denotes the orientation of input and output polarization analyzers. H: horizontal, V: vertical, R: right hand circular, L: left hand circular, P: $+45^o$, M:-45^o and O: open polarization optics or none. Adapted from [49]. Note typographical errors were corrected for the following elements: $S_{14} = RO - LO$, $S_{22} = (HH+VV)-(HV+VH)$, $S_{23} = (PH+MV)-(PV+MH)$, $S_{24} = (RH+LV)-(RV+LH)$, $S_{32} = (HP+VM)-(HM+VP)$, $S_{33} = (PP+MM)-(PM+MP)$, $S_{34} = (RP+LM)-(RM+LP)$, $S_{41} = OR - OL$, $S_{42} = (HR + VL) - (HL + VR)$, $S_{43} = (PR + ML) - (PL + MR)$ and $S_{44} = (RR + LL) - (RL + LR)$ [50].

with light having different state of polarizations such as $H, V, +45^o, -45^o, RHC, LHC$. For each incident polarization, the scattered light is analyzed with different analyzer configurations, such as $P_H, P_V, P_{+45^o}, P_{-45^o}, P_{RHC}, P_{LHC}$, and assembling the Mueller matrix coefficients for thesis measurements. However, these 16 elements are determined through four complex parameters and the resulting Mueller Jone matrix is not general and can not represent depolarization, hence it does not require all 16 elements, only 7 is required.

In Imaging polarimetry, these measurements are made for every pixel in a two-dimensional image. Here we discuss the Mueller matrix imaging polarimetry through a scattering sample for the case of a single focused spot through a scattering media. As shown in Figure 2.7, the experimental and Monte Carlo Mueller spatially varying scattering matrix are compared for polarized light illumination on tissue-like scattering phantom [49]. The phantom is composed of a suspension of 2μm polystyrene spheres suspended in water ($\mu_s^{'} \approx 12cm^{-1}$, $g \approx 0.912$ and $\mu_a \approx 0$). To measure the 16 Mueller scattering matrix elements, 49 images were taken at different combinations of input and output state of polarization for the analyzers. The details of the combinations are indicated in the figure. In the study presented in [49], each image were taken with a 12-bit cooled CCD camera with exposure time of 1.7 s to average out the speckles induced by the laser as the spheres moved around in the water which generally has an estimated correlation time on the order of about 10 ms. The results show excellent agreement between the experiment and the computation of the Mueller scattering matrix based on Monte Carlo method. (The Monte Carlo method relies on discretize the scattered light and express the scattering as a sum of a large number of random photon trajectories. Each photon trajectory starts from where the corresponding scattering took place. There is a threshold for when the trajectory should be ignored if their contribution is small. The Mueller scattering matrix can be then computed after the contributions of the photon trajectories are known.) From the results shown in Figure 2.7, only 4 elements are independent (the rest can be obtained by simple rotations), indicating fewer measurements is actually needed which can simplify the acquisition process and speed up the experiment. To summarize the scattering Mueller matrix components using the state of polarization notations in Figure 2.7, we can write the following using M as the notation of Mueller matrix elements,

$$\begin{aligned}
M_{11} &= OO \\
M_{12} &= HO - VO \\
M_{13} &= PO - MO \\
M_{14} &= RO - LO \\
M_{21} &= OH - OV \\
M_{22} &= (HH + VV) - (HV + VH) \\
M_{23} &= (PH + MV) - (PV + MH) \\
M_{24} &= (RH + LV) - (RV + LH) \\
M_{31} &= OP - OM \\
M_{32} &= (HP + VM) - (HM + VP) \\
M_{33} &= (PP + MM) - (PM + MP) \\
M_{34} &= (RP + LM) - (RM + LP) \\
M_{41} &= OR - OL \\
M_{42} &= (HR + VL) - (HL + VR) \\
M_{43} &= (PR + ML) - (PL + MR) \\
M_{44} &= (RR + LL) - (RL + LR)
\end{aligned} \tag{2.34}$$

(Hence from the above relations, we can see the 4 independent elements are M_{11}, M_{22}, M_{33}, M_{44} for this specific experiment. However, in general there should be at most 7 independent Mueller matrix elements for a single scatterer.)

2.4.3 Polarization difference imager

To obtain high speed and polarization imaging in scattering medium, a polarization difference imaging (PDI) technique can be used, which is an extension of the single polarizer imaging polarimetry technique discussed in Section 2.4. Compared to the full Mueller matrix polarimetry, PDI is a faster and more practical technique to enhance ballistic light while suppressing multi-scattered photons in scattering medium. It only requires two captures of intensity images for horizontal and vertical polarization, or left hand circular and right hand circular polarization, respectively, which is essentially the second term in the Stokes parameter shown in Equation 2.28: $S_1 = I_H - I_V$, while the first term $S_0 = I_H + I_V$ corresponds to polarization sum imaging which is essentially the conventional imaging technique used commonly. The circular polarization case corresponds to decomposing the Stokes parameters with: $S_0 = I_{LHC} + I_{RHC}$ and $S_3 = I_{LHC} - I_{RHC}$.

Significant contrast can be obtained using this method in scattering medium assuming there is a difference between the polarization properties of the light scattered from the background and the light scattered by the object. When applied for range sensing, this high speed method was shown to improve the range detection by a factor of 2 to 3 [51, 6]. In the next chapter, I will present experimental investigation of the PDI technique for optical imaging in scattering medium using orthogonal linear polarization measurements.

2.4.4 Polarization memory effect of circularly polarized light in scattering medium

The polarization memory effect has been investigated since 1978 [52, 53, 54] and can be used to enhance the visibility of an object buried within a highly scattering medium such as dense fog or smog. This effect is based on the fact that when traveling in a scattering medium, the weak ballistic light maintains the same or similar polarization state, hence “remembering” the illumination polarization state, while the diffuse light loses the original polarization state and its polarization quickly becomes randomized, hence “losing” the illumination polarization state. If we could block the unpolarized light selectively, letting the polarized light through a polarizer, we could see through a scattering medium. Unfortunately we can not do that and half of the unpolarized light passes through the polarizer. But we might expect a contrast improvement by a factor of two.

The memory effect of circularly polarized light is an interesting phenomenon with potential for improving optical imaging in scattering media. A circular polarization survival parameter can be derived from the Stokes parameters introduced in the previous section. The Mie theory provides an exact solution for scattering of a plane wave by single spherical particle of any size. Recall the scattering matrix 2.32 relating the incoming and the scattered Stokes parameters that describe the polarization, for spherical particles, $S_{sc3} = S_{sc4} = 0$ in Equation 2.21, the matrix can be simplified to the following form [55, 37]: $\mathbf{M_{sc}} = \begin{pmatrix} M_{11} & M_{12} & 0 & 0 \\ M_{12} & M_{11} & 0 & 0 \\ 0 & 0 & M_{33} & M_{34} \\ 0 & 0 & -M_{34} & M_{33} \end{pmatrix} \begin{pmatrix} 1 \\ 0 \\ 0 \\ 1 \end{pmatrix}$ where each scattering matrix elements depend on the scattering angle θ and ϕ. Since for right hand circularly polarized light, $S_{0out} = S_{3out} = 1$ and $S_{1out} = S_{2out} = 0$, the scattered Stokes parameter is thus the following, $\mathbf{S_{out}} = \begin{pmatrix} S_{0out} \\ S_{1out} \\ S_{2out} \\ S_{3out} \end{pmatrix} = \begin{pmatrix} M_{11} \\ M_{12} \\ M_{34} \\ M_{33} \end{pmatrix}$. Hence from Eqn. 2.31, the degree of circular polarization for this case can be expressed as, $DoP_c = \frac{M_{33}}{M_{11}}$. As discussed previously, the 16 Mueller matrix components all together provide a qualitative description of the scattering medium. Hence by comparing two entire Mueller matrix measurements we can distinguish qualitatively two scattering medium. By looking at each component of the Mueller scattering matrix, a more detailed analysis of the scattering medium can be obtained. For example, the M_{44} term which is calculated from 4 measurements involves only circularly polarized light, as shown in the last term in Figure 2.7 where $M_{44} = (LL - RR) - (RL + LR)$. M_{44} is essentially a measurement of the efficiency of the medium in maintain (for positive M_{44}) or flipping (for negative M_{44}) the helicity of the back-scattered light.

The measurement of M_{44} was performed in an investigation previously to measure optical properties of a highly scattering medium and the results are shown in Figure 2.8. In this study, four different sizes of polystyrene sphere suspensions were investigated ($d = 204, 497, 890$ and $2040nm$, where d represents the nominal mean diameters of the spheres). The illumination wavelength is $\lambda = 543nm$ from a green HeNe laser. The back-scattered light from the scattering medium was imaged through polarization-analysis optics onto a CCD camera. A variety of intensity patterns were observed by changing the input state of polarization and changing the analyzer to detect

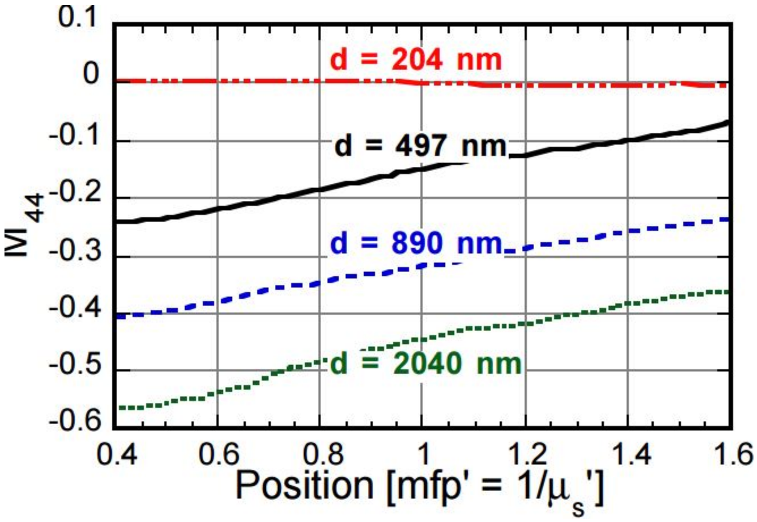

Figure 2.8: M_{44} obtained from 4 different polystyrene sphere suspensions. d is diameter of the spheres in the suspension. The position is represented in terms of mean transport free path ($l_s^{'}$=mfp′=$\frac{1}{\mu_s^{'}}$, where $\mu_s^{'}$ is the reduced scattering coefficient). Courtesy of [56].

different polarization components of the back-scattered light. From Figure. 2.8, it can be seen that M_{44} increases with decreasing sphere size. This indicates the larger scattering spheres flips the helicity of the light more effectively. The larger the particle the closer resembles a mirror because the scattering cross section is increased in which case the helicity is flipped and $M_{44} \approx -1$. On the other extreme, if the sphere is too small, $M_{44} \approx 0$, and because $M_{44} = (RR + LL) - (RL + LR)$ the state of polarization of the back-scattered light should be equally RHC and LHC representing a circular depolarization.

A rigorous simulation using Monte Carlo polarization tracking was demonstrated recently for evolution of circularly polarized light in scattering medium [57]. The results found that linearly polarized input light remain highly polarized for small number of scattering events but depolarize more quickly than circularly polarized input light. Interestingly, the research also found in general, circularly polarized light persists through a larger number of scattering events longer than linearly polarized light in a scattering medium. Because the circularly polarized light maintains a reasonably high degree of circular polarization and remains in a range of states close to the initial state of polarization through a large number of scattering events especially in forward scattering geometries, this polarization memory effect can have an interesting potential for applications in optical remote sensing, deepening the penetration depth for polarization resolved imaging in various scattering media such as biological tissue, fog, smog and navigation by using a circular polarization filtering. In addition, the Stokes parameter described in this chapter are a useful tool that will also be used in the investigation of polarization dynamics of the supercontinuum light source development for optical imaging in Chapters 5, 6 and 7. This polarization memory effect provides part of the motivation for the development of such a circularly polarized broadband light source with the potential for improving optical imaging in scattering medium.

Chapter 3

Polarization-gated optical imaging in scattering medium

3.1 Polarization-gating imaging in scattering medium

In the last chapter, we see optical scattering severely degrade image quality for a variety of scattering situations including under-sea photography, atmospheric remote sensing and biomedical imaging. However, several approaches have been developed to mitigate the effects of scattering including time-resolved imaging[58, 59], optical coherence techniques[60, 59], confocal microscopy [60] and diffuse photon imaging [33]. Although these methods can provide substantial improvements on the depth into a scattering medium that can be imaged, they can require expensive and complex implementations and may not be practical to use in all situations. Another category of technique for imaging a short distance into a scattering medium relies on simple polarization sensitive detection of the scattered light to image the embedded objects. This class of imaging utilizes differential polarimetry discussed in Chapter 2, which is relatively easy to implement with either passive or active illumination. It also can be combined with the aforementioned time-resolved imaging and optical coherence techniques to further improve object detection in scattering environments. Note in this chapter, I will refer to the conventional intensity-only imaging as polarization sum imaging, because the intensity of light can be decomposed to vertical and horizontal eigen-states as $I_{tot} = I_H + I_V$ as discussed in Chapter 2 for the Stokes parameter formalism.

In fact, in nature, the retina of some insects and certain birds, reptiles and fish are sensitive to polarization in the environment [61]. Behavioral studies provided evidence for polarization sensitivities in vertebrates by the change in orientation of animals as a function of incident polarization [62]. Some species of fish are also able to discriminate the direction of polarization of the visible light in addition to intensity and wavelength [63]. This study for fish shows that different cone mechanisms exhibit different polarization responses, and it has been found that certain double cones are sensitive to the direction of polarization. These types of fish (for e.g., teleost fishes or rainbow trout) are capable of detecting the polarization of light and it is generally believed their paired retinas are arranged orderly and possess some subtle optical anisotropy and it has been proposed that they may function as polarization detecters [63]. For fish with double cones, polarization can be detected by comparison of signals from cells in double cones or between double cones with orthogonally arranged partitions. It has been proposed that double cones are ideally situated to functions as the input for the computation of a retinal polarization difference image. The double cone inner segment functions as a polarization analyzer by using the geometric birefringence and a neural network computes a local polarization difference at each point in the retina to enhance polarization contrast [64].

3.1.1 Resolution and contrast enhancement using polarization

The point spread function (PSF) of polarization difference imaging can be compared with intensity imaging to ascertain the theoretical resolution improvement. As illustrated in Figure 3.1, the imaging system for computing the PSF is a $4f$ imaging setup that captures the radiation of a dipole point source located in a thin slab of scattering medium. The scattering slab is assumed infinite in x and y directions and consists of identical scatterers uniformly distributed. The dipole source (Object O in Figure 3.1) is most relevant to a fluorescent point source emitter embedded inside a scattering medium. The scattered electric field at a far distance is assumed to be a spherical wave so the effect of the nth scatterer can be treated as a point source. The scatterers are assumed to be stationary in the medium even though in many cases tissue can move. Note this is assumed to be a single scattering medium. In addition, the effect of blurring and depolarization is the focus of the study, hence the details of the point source and receiver interaction is omitted. The effect of the scattering on the optical image can be determined as the following.

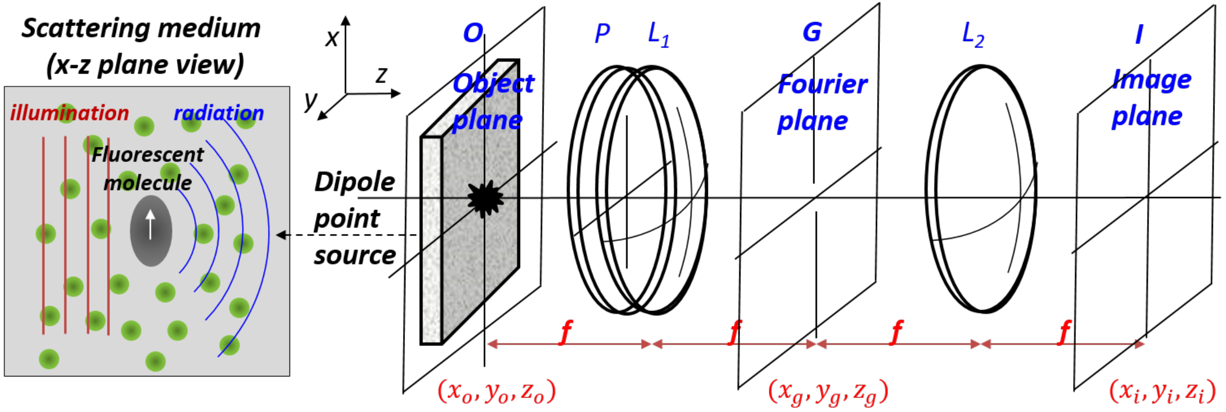

Figure 3.1: $4f$ imaging system for computing point spread function. O: object, a thin slab of scattering medium, P: polarization analyzer, L_1 and L_2: lenses, G: Fourier filter, f: focal length of lenses.

The scattered electric field in Eqn 2.21 can be applied in this case and it is re-written as the following,

$$\mathbf{E}_s = \begin{bmatrix} \mathbf{E}_{\|\mathbf{s}} \\ \mathbf{E}_{\perp\mathbf{s}} \end{bmatrix} = \frac{e^{ik(r-z)}}{-ikr} \begin{bmatrix} S_{sc2} & S_{sc3} \\ S_{sc4} & S_{sc1} \end{bmatrix} \begin{bmatrix} E_{\|i} \\ E_{\perp i} \end{bmatrix}$$

By applying Fourier optics and following the theoretical derivations in [65], the field at the image plane due to a point source can be represented as,

$$\begin{aligned}
\mathbf{E}_i^n(x_i, y_i) = \frac{\alpha e^{i\kappa(4f-z_n)}\kappa^2}{(\lambda f)^2} & \int\int_O \bar{\bar{\mathbf{P}}}\mathbf{E}_{sc}^n(\hat{\mathbf{z}}) \times \delta(x_o - x_n)\delta(y_o - y_n) \\
& \int\int_G G(x_g, y_g) \times e^{i\frac{\pi}{\lambda f}(x_g^2+y_g^2)} \times e^{-i\frac{2\pi}{\lambda f}(x_g x_o + y_g y_o)} \times e^{-i\frac{2\pi}{\lambda f}(x_g x_i + y_g y_i)} dx_g dy_g dx_o dy_o \\
& = \frac{\alpha e^{i\kappa(4f-z_n)}\kappa^2}{(\lambda f)^2} \bar{\bar{\mathbf{P}}}\mathbf{E}_{sc}^n(\hat{\mathbf{z}}) \times \mathscr{F}\{G(x_g, y_g) \times e^{i\frac{\pi}{\lambda f}(x_g^2+y_g^2)}\}\big|_{f_x = \frac{x_n + x_i}{\lambda f}, f_y = \frac{y_n + y_i}{\lambda f}} \qquad (3.1)
\end{aligned}$$

where the field at the image plane due to the nth scatterer is $\mathbf{E}_i^n(x_i, y_i)$, δ is the Dirac delta function, κ is a constant representing optical throughput, $\bar{\bar{\mathbf{P}}}$ is the tranmission matrix of the polarization analyzer placed in front of lens L_1, α is an attenuation constant assumed the same for all scatterers, $\mathbf{E}_{sc}^n(\hat{\mathbf{z}})$ is the scattered field of the nth scatterer in $\hat{\mathbf{z}}$ direction that is obtained from Eqn 2.21 assuming single scattering. $G(x_g, y_g)$ is the transfer function for the spatial filter located at the intermediate Fourier plane. Note the subscripts o, g and i denotes object, filter and image plane respectively. This equation is simplified using two dimensional Fourier transform using $f_x = \frac{x_n+x_i}{\lambda f}$ and $f_y = \frac{y_n+y_i}{\lambda f}$ as the spatial frequencies in x and y directions respectively. $\mathscr{F}$ is the two-dimensional Fourier transform of the spatial functions evaluated at spatial frequencies f_x and f_y. For the electric field scattered by a single scattering arrangement, we need to sum the $\mathbf{E}_i^n(x_f, y_f)$ over the scattering volume for N number of scatterers, $\mathbf{E}_i(x_i, y_i) = \sum_{n=1}^{N} \mathbf{E}_i^n(x_i, y_i)$. Therefore, because we are assuming uniformly distributed scatterer that are non-interacting, the ensemble average is given by the intensity distributions which can be written as [66],

$$|\mathbf{E}_i(x_i, y_i)|^2 = \int_V |\mathbf{E}_i^n(x_i, y_i; x_o, y_o, z_o)|^2 \rho dx_o dy_o dz_o \tag{3.2}$$

where ρ is the concentration of the scatterers in the medium, V is the volume of the scattering medium, and $\mathbf{E}_i^n(x_i, y_i; x_o, y_o, z_o)$ is the electric field at (x_i, y_i) in the image plane due to the scatterer located at (x_o, y_o, z_o) in the object plane. Therefore, the general PSF for the polarization sum and polarization difference imaging technique can be represented by the following,

$$\mathbf{I}_i^{PS}(x_i, y_i) = |\mathbf{E}_i^{PS}(x_i, y_i)|^2 = |\mathbf{E}_i^{\mathbf{x}}(x_i, y_i)|^2 + |\mathbf{E}_i^{\mathbf{y}}(x_i, y_i)|^2 \tag{3.3}$$

$$\mathbf{I}_i^{PD}(x_i, y_i) = |\mathbf{E}_i^{PD}(x_i, y_i)|^2 = |\mathbf{E}_i^{\mathbf{x}}(x_i, y_i)|^2 - |\mathbf{E}_i^{\mathbf{y}}(x_i, y_i)|^2 \tag{3.4}$$

where $\mathbf{E}_i^{\mathbf{x}}(x_i, y_i) = p_x \vec{\mathbf{E}}_i = \begin{bmatrix} 1 & 0 \\ 0 & 0 \end{bmatrix} \vec{\mathbf{E}}_i$, $\mathbf{E}_i^{\mathbf{x}}(x_i, y_i) = p_y \vec{\mathbf{E}}_i = \begin{bmatrix} 0 & 0 \\ 0 & 1 \end{bmatrix} \vec{\mathbf{E}}_i$ In general, Rayleigh scattering function does not adequately model the optical scattering in many environments such as biological tissue or milk mixture scattering phantom. For example, in a milk scattering phantom, the fatty molecules typically range from 0.1μm to 20μm, with an average diameter between $1-3\mu$m [67]. This milk size distribution measurements can be seen in the plots shown in Figure 3.5. Hence, Mie scattering function is typically used in optical scattering simulations [68].

As discussed in Chapter 2, Mie scattering approximates a more realistic scattering amplitude for many scattering mediums in practice. To investigate the PSF distributions for a medium with Mie scatterers, in the following I will continue to derive the PSFs for both polarization sum and polarization difference techniques starting from [65]. The scattering amplitude functions are given in Eqn 2.22. Hence starting from [65] the intensities can be represented as the following,

$$\mathbf{I}_i^x(x_i, y_i) = |\mathbf{E}_i^x(x_i, y_i)|^2 \approx \frac{1}{r^2} \times sin^2\theta \times cos^2\theta \times cos^2\phi \tag{3.5}$$

$$\mathbf{I}_i^y(x_i, y_i) = |\mathbf{E}_i^y(x_i, y_i)|^2 \approx \frac{1}{r^2} \times sin^4\theta \tag{3.6}$$

Therefore, I can write the polarization sum and polarization difference PSFs for Mie scatterers respectively as,

$$\begin{aligned}\mathbf{I}_i^{PS}(x_i, y_i) &= |\mathbf{E}_i^{\mathbf{x}}(x_i, y_i)|^2 + |\mathbf{E}_i^{\mathbf{y}}(x_i, y_i)|^2 \\ &\approx \frac{1}{r^2} \times sin^2\theta \times cos^2\theta \times cos^2\phi + \frac{1}{r^2} \times sin^4\theta\end{aligned} \tag{3.7}$$

$$\begin{aligned}\mathbf{I}_i^{PD}(x_i, y_i) &= |\mathbf{E}_i^{\mathbf{x}}(x_i, y_i)|^2 - |\mathbf{E}_i^{\mathbf{y}}(x_i, y_i)|^2 \\ &\approx \frac{1}{r^2} \times sin^2\theta \times cos^2\theta \times cos^2\phi - \frac{1}{r^2} \times sin^4\theta\end{aligned} \tag{3.8}$$

where (r, θ, ϕ) described the spherical coordinates of the position of the point with unit magnification $(x_o = -x_i, y_o = y_i, z_o = 0)$ with respect to the dipole source at the origin. Then Eqn 3.7 can be transformed to Cartesian coordinates using $(r = \sqrt{x_i^2 + y_i^2 + z_i^2}, \theta = cos^{-1}(z_i/r)$ and $\phi = tan^{-1}(y_i/x_i)$ as the following,

$$|\mathbf{E}_i^{\mathbf{x}}(x_i, y_i)|^2 = \frac{1}{x_i^2 + y_i^2} \tag{3.9}$$

$$|\mathbf{E}_i^{\mathbf{y}}(x_i, y_i)|^2 = \frac{1}{x_i^2 + y_i^2} \times cos^2\left(tan^{-1}\left(\frac{y_i}{x_i}\right)\right) \tag{3.10}$$

Therefore, the PSF for polarization sum and polarization difference for Mie scatterer can be represented as,

$$\mathbf{I}_i^{PS}(x_i, y_i) = \frac{1}{x_i^2 + y_i^2} + \frac{1}{x_i^2 + y_i^2} \times cos^2\left(tan^{-1}\left(\frac{y_i}{x_i}\right)\right) \tag{3.11}$$

$$\mathbf{I}_i^{PD}(x_i, y_i) = \frac{1}{x_i^2 + y_i^2} - \frac{1}{x_i^2 + y_i^2} \times cos^2\left(tan^{-1}\left(\frac{y_i}{x_i}\right)\right) \tag{3.12}$$

To compare the PSFs for the polarization difference and sum techniques, I plot the PSF distribution functions derived in Eqn 3.11 in Figure 3.2.

As demonstrated in Figure 3.2, (a) is the PSF for polarization sum imaging and (b) is the PSF for polarization difference imaging of a simple point source emitter. The polarization

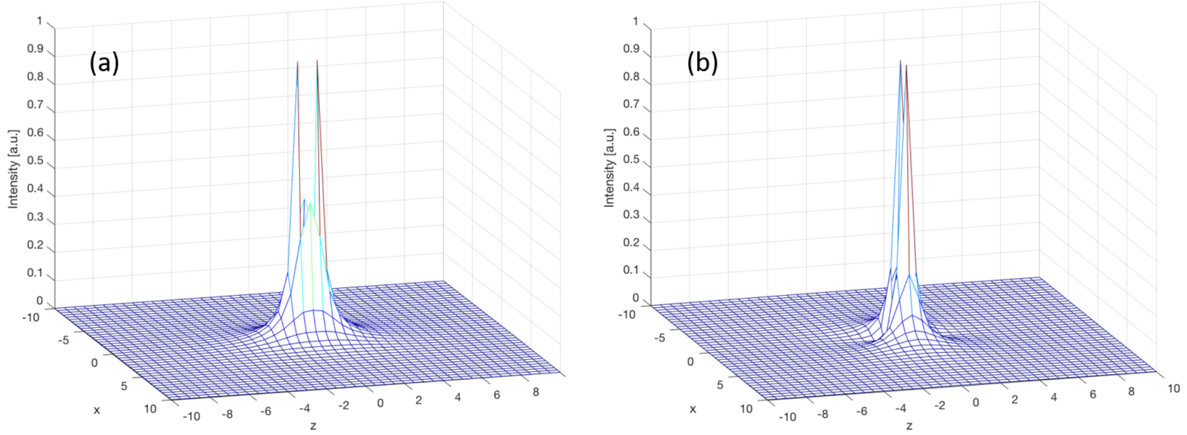

Figure 3.2: Point spread function distributions for a medium of Mie scatterers. (a) Polarization sum case (b) Polarization difference case.

difference PSF shows a narrower width compared with the polarization sum PSF distribution. The PSF distribution for Rayleigh scatterers has been demonstrated in [65]. The results from this Rayleigh scattering case is shown in Figure 3.3. In this study, it was found that the 3dB width for polarization difference PSF is about half the size relative to the polarization sum PSF. Because the Mie polarization sum and difference PSFs derived in Eqn 3.11 has a similar form relative to the Rayleigh polarization sum and difference PSFs derived in [65], the PSFs shown in Figure 3.3 and 3.2 are very similar.

For multiple scattering environments, the single scattering analysis becomes insufficient. However, the analysis obtained above may provide some insights into some previous investigations of using polarization sensitive methods to improve image resolution and contrast at relatively short optical thickness [6, 51, 69]. The narrower portion of the polarization difference PSF can be related to the enhanced detectability of objects demonstrated in [6]. This implies that the objects with fine details, especially edges of objects, can be detected with greater resolution by using polarization difference imaging in weak to medium scattering regime. Beyond this regime, a probabilistic photon-tracking Monte Carlo simulation would be required to extend the analysis to multiple-scattering regime. The probabilistic density function (PDF) for the direction of scatterer

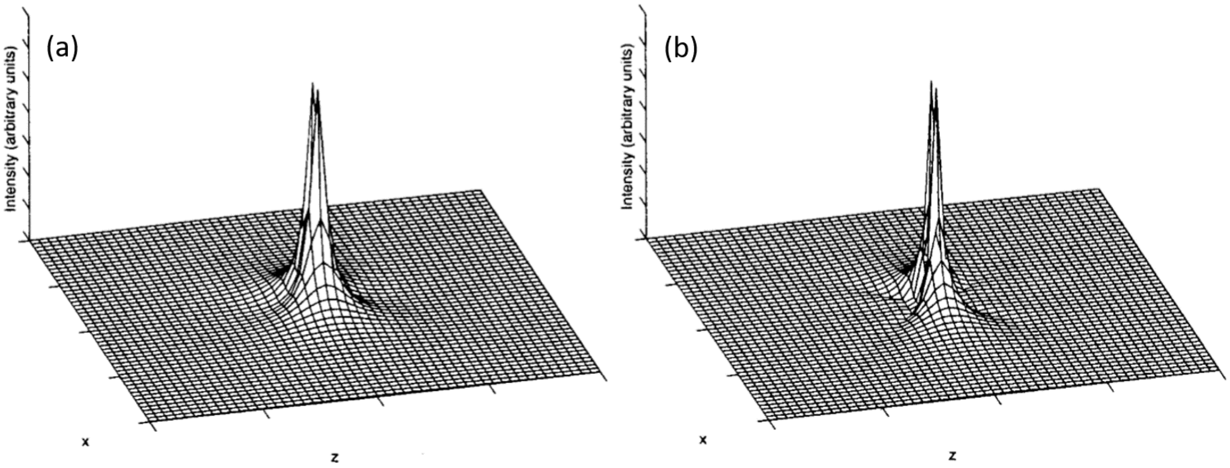

Figure 3.3: Point spread function distributions for a medium of Rayleigh scatterers. (a) Polarization sum case (b) Polarization difference case. Adapted from [65]

can be derived from the respective scattering functions for both Rayleigh and Mie scattering. However, for greater optical thickness (more than 10 transport mean free paths), the analysis can also be applied for time-resolved imaging which distinguishes ballistic and multiple scattered photons and greatly reduces the multiple-scattered light that can degrade the image.

3.1.2 Depolarization of multiple scattered light in a scattering medium

Images captured in conventional imaging systems record and measure the overall signal intensity of an object. However, theoretically the recorded image can be decomposed to linearly orthogonal eigen-polarization components. In a study presented in [70, 7], for a very strongly scattering medium, a time-gated imaging combined with polarization difference imaging is applied to eliminate most of the multiple-scattered photons from the PSF. Essentially the polarization difference image functions as an additional gating mechanism to enhance the forward-scattering light.

In the literature, the forward scattering photons is also referred to as ballistic photons, which are the unscattered or singly scattered light that contains high resolution information of the object for a limited imaging depth. The intensity of the ballistic light decays exponentially with the path length in the scattering medium that obeys the Bouguer-Beer-Lambert law discussed in Eqn 2.1, mathematically we can write the following,

$$I_{tot}(x,y) \sim I_{nb}(x,y) \tag{3.13}$$

$$I_b(x,y) \sim e^{-\mu_s L} I_{tot}(x,y) \tag{3.14}$$

$$n_{tot}(x,y) = n_{||}(x,y) + n_{\perp}(x,y) = \sigma_{shot} + \sigma_{det} = \sqrt{I_{tot}(x,y)} + \sigma_{det} \tag{3.15}$$

where $I_{tot}(x,y)$ is the intensity of the total incident light, I_{nb} is the intensity of the non-ballistic light and I_b is the intensity of ballistic light which decays exponentially as a function of distance L and scattering coefficient μ_s. $n_{tot}(x,y)$ is the total noise that includes shot noise $\sqrt{I_{tot}(x,y)}$ and detector noise σ_{det}, where $\sigma^2_{n_{tot}} \sim I_{tot}(x,y) + \sigma^2_{det}$. The intensities of the orthogonal polarization components can be described by $I_{\perp}(x,y)$ and $I_{||}(x,y)$ respectively. Hence this allows us to extract the high resolution information encoded in the ballistic light by subtracting $I_{\perp}(x,y)$ from $I_{||}(x,y)$ using polarization gating as the following,

$$I_{||}(x,y) = I_b(x,y) + \frac{1}{2} I_{nb}(x,y) + n_{||}(x,y) \tag{3.16}$$

$$I_{\perp}(x,y) = \frac{1}{2} I_{nb}(x,y) + n_{\perp}(x,y) \tag{3.17}$$

Hence the polarization difference intensity can be represented as,

$$I_{PD}(x,y) = I_{||}(x,y) - I_{\perp}(x,y) = I_b(x,y) + n_{||}(x,y) + n_{\perp}(x,y) \tag{3.18}$$

Hence the signal to noise ratio can be written as,

$$SNR = \frac{I_b(x,y)^2}{\frac{1}{2} I_{tot}(x,y) + \sigma^2_{det} + \frac{1}{2} I_{tot}(x,y) + \sigma^2_{det}} = \frac{(e^{-\mu_s L} I_{tot}(x,y))^2}{I_{tot}(x,y) + 2\sigma^2_{det}} = \frac{e^{-2\mu_s L} I_{tot}(x,y)}{1 + \frac{2\sigma^2_{det}}{I_{tot}(x,y)}} \tag{3.19}$$

The above equations are representations of the gating of forward scattering/ballistic photons in scattering medium including noise terms and exponential decays of the ballistic light intensity. However, it is assuming the multiple scattered photons is completely depolarized. In a medium containing small particles relative to the wavelength, i.e. the Rayleigh scattering regime, the characteristic depolarization length for linearly polarized incident light is greater than that of circularly polarized light (typically a factor of two). For larger scattering particles, i.e. Mie scattering regime, the opposite is true [71].

To analyze the depolarization of light in scattering medium, the theory of partial coherence based on Stochastic process should be used. The coherency matrix from this approach allows us to investigate the energy transport and the entropy of the multiple scattered light, because the intensity of light can be described by the trace of the coherency matrix while the degree of polarization is analytically related to the radiation entropy [72]. The coherency matrix **J** is Hermitian and can be represented as the following,

$$\mathbf{J} = \begin{bmatrix} \langle E_x E_x^* \rangle & \langle E_x E_y^* \rangle \\ \langle E_y E_x^* \rangle & \langle E_y E_y^* \rangle \end{bmatrix} \tag{3.20}$$

where the trace of the matrix is defined as the sum of the diagonal elements,

$$tr(\mathbf{J}) = J_{xx} + J_{yy} = \langle E_x E_x^* \rangle + \langle E_y E_y^* \rangle \tag{3.21}$$

The diagonal elements are real and represents the intensities in the x and y directions, respectively. In addition, the determinant of the matrix is defined as the following,

$$det(\mathbf{J}) = \langle E_x E_x^* \rangle \langle E_y E_y^* \rangle - \langle E_x E_y^* \rangle \langle E_y E_x^* \rangle \tag{3.22}$$

The degree of polarization of the light is given by,

$$DOP = \sqrt{1 - 4\frac{det(\mathbf{J})}{tr(\mathbf{J})^2}} = \sqrt{1 - \frac{4|\mathbf{J}|}{(J_{xx} + J_{yy})^2}} \tag{3.23}$$

Hence the Stokes parameters discussed in Chapter 2 and coherency matrix are related by the following,

$$\langle S_0 \rangle = J_{xx} + J_{yy} = \langle E_x E_x^* \rangle + \langle E_y E_y^* \rangle \tag{3.24}$$

$$\langle S_1 \rangle = J_{xx} - J_{yy} = \langle E_x E_x^* \rangle - \langle E_y E_y^* \rangle \tag{3.25}$$

$$\langle S_2 \rangle = J_{xy} + J_{yx} = \langle E_x E_y^* + E_y E_x^* \rangle \tag{3.26}$$

$$\langle S_3 \rangle = i(J_{yx} - J_{xy}) = i\langle E_y E_x^* - E_x E_y^* \rangle \tag{3.27}$$

It has been shown that correlation function for the scattered electric field is given by [72],

$$g(\mathbf{r},t) = \frac{\langle E(0)E^*(t)\rangle}{\langle |E(0)|^2\rangle} = \frac{\int \mathbf{G}(\mathbf{r},n)e^{-2nt/\tau_0}dn}{\int \mathbf{G}(\mathbf{r},n)dn} \tag{3.28}$$

where $\mathbf{G}(\mathbf{r},n)$ denotes Green's function representing the number of scattering paths of lenghs nl, τ_0 is the time it takes for a scatterer to move one optical wavelength, n is the number of scattering events. It has been shown that degree of polarization can be expressed as [71],

$$DoP_i = \frac{\int G(\mathbf{r},n)f_i(n)dn}{\int G(\mathbf{r},n)dn} \tag{3.29}$$

where function $f_i(n) = f_C(n)$ and $f_i(n) = f_L(n)$ (L for linear and C for circular state of polarization) represent the dependences of the output DOPs for a number of scatterings equal to $n+1$ as $f_L(n) = \frac{3}{2}e^{-n\frac{l}{\Im_L}}$, $f_C(n) = \frac{3}{2}e^{-n\frac{l}{\Im_C}}$, where $\Im_i$ denotes characteristic length of depolarization for $n+1$ of scattering paths, and they are given by $\Im_L = \frac{l}{ln(10/7)}$ and $\Im_C = \frac{l}{ln(2)}$, respectively [72]. l is the transport mean free path of the photon, $l = 1/(N\sigma)$, and it is related to the scattering coefficient by $l = \frac{1}{\mu_s(1-g)}$, where g is the mean cosine of the scattering angle ($g = 1$ for forward scattering, $g = 0$ for isotropic scattering, hence g decreases as the particle size decreases). N is the concentration of the scatterers and σ is the scattering cross section. In the weakly scattering limit, $kl \gg 1$, which means the mean free path is much greater than the wavelength of the radiation, where k is the wave number in the scattering medium. Following [71] to integrate Eqn 3.28, we obtain the degree of polarization as,

$$DoP_C = \frac{d}{l}\frac{sinh(l/\xi_C)}{sinh(d/\xi_C)} = \frac{d}{l}\frac{sinh(\sqrt{3ln(2)})}{sinh(\frac{d}{l}\sqrt{3ln(2)})} \tag{3.30}$$

$$DoP_L = \frac{d}{l}\frac{sinh(l/\xi_L)}{sinh(d/\xi_L)} = \frac{d}{l}\frac{sinh(\sqrt{3ln(10/7)})}{sinh(\frac{d}{l}\sqrt{3ln(10/7)})} \tag{3.31}$$

Hence for a scattering slab with thickness $d \gg \xi_{L,C}$, the degree of polarization in the far field can be approximated by,

$$DoP_C \approx \frac{2d}{l}sinh\Big(\frac{l}{\xi_C}\Big)e^{-\frac{d}{\xi_C}} = \frac{2d}{l}sinh(\sqrt{3ln(2)})e^{-\frac{d}{l}\sqrt{3ln(2)}} \tag{3.32}$$

$$DoP_L \approx \frac{2d}{l}sinh\Big(\frac{l}{\xi_L}\Big)e^{-\frac{d}{\xi_L}} = \frac{2d}{l}sinh(\sqrt{3ln(10/7)})e^{-\frac{d}{l}\sqrt{3ln(10/7)}} \tag{3.33}$$

where $\xi_{L,C} = (\Im_{L,C} l/3)^{1/2}$ denotes the characteristic lengths of depolarization for the slab geometry. From Eqn 3.32, it can be seen that the depolarization characteristic length for linearly polarized light is greater than that of circularly polarized incident light by a factor of $\sqrt{2}$. Here, I plot the results to obtain more insights into the depolarization of the different incident polarizations in the scattering medium. In Figure 3.4, DoP_L and DoP_C are compared as a function of number of transport mean free path l for a scattering slab with thickness between 0 and 26 scattering lengths. The scattering coefficient is within $[1mm^{-1}, 100mm^{-1}]$. The anisotropic factor $g = 0.3$ corresponds to particle size of about 0.205μ for non-fat milk particles (which will be presented in 3.5). We see both the initially linearly and circularly polarized light become depolarized as the number of scattering lengths increase. However, we see the DoP_L is greater than DoP_C after going through a single scattering length. As the photons experience higher number of scattering events, both DoP_L and DoP_C approach zero and the light eventually becomes completely depolarized.

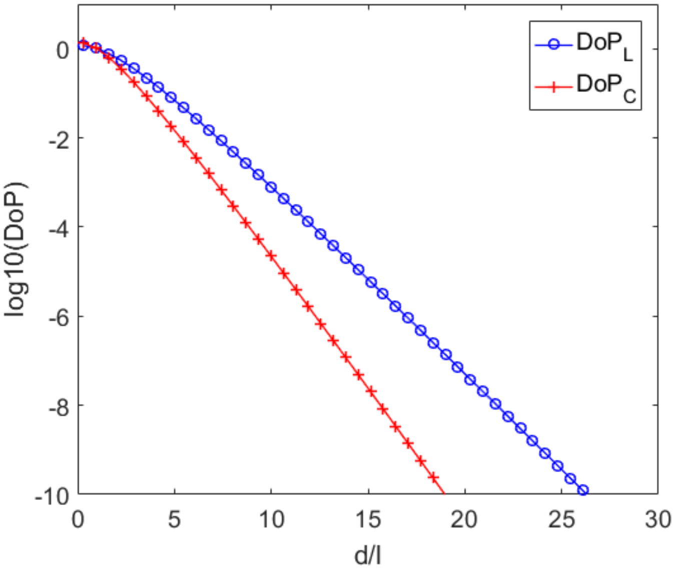

Figure 3.4: Degree of polarization for linearly and circularly polarized light in the Non-fat scattering medium (small scattering particle size of 0.205μm). The MATLAB simulation is based on Rayleigh scattering using Eqn 3.32. x-axis is number of scattering lengths, y-axis is in log_{10} scale for degree of polarization. DoP_L is plotted as circles, and DoP_C is plotted as crosses.

However, as pointed out in [73, 2], In the forward scattering Mie regime (i.e. large particles), the depolarization characteristic length is greater for circularly polarized light than linearly polarized light. To depolarize circularly polarized light, it requires both randomization of the helicity and the direction, this is related to the polarization memory effect of circularly polarized light investigated recently, which may explain the DoP of circularly polarized light is maintained over more scattering lengths. As described in Figure 2.8 in Chapter 2, the polarization memory effect related to circularly polarized light, M_{44} can be calculated from 4 measurements involving only circularly polarized light, it is essentially a description of the efficiency of flipping the helicity of the scattered light. We can see in the Mie scattering regime, the flipping of helicity becomes more efficient hence the probability of preserving the degree of polarization becomes greater for larger particles with circularly polarized light. Therefore it is possible to better maintain the DoP_C in a Mie scattering medium than in a Rayleigh scattering medium, and this may improve light propagation in scattering medium with larger particles (compared to the wavelength) that involves relying on using polarization as the sensing or imaging method.

3.2 Experiment: Characterization of scattering tissue phantom

Experimentally, the polarization gating can be achieved by using polarimetry by recording orthogonally polarized images through a linear polarization analyzer setup, and then subtracting orthogonally polarized images. In my experiment, the scattering coefficient μ_s will be measured for a tissue phantom consists of non-fat milk solution. In specific, the decay of the intensity of the ballistic signal after exiting the scattering medium is measured. Note since the milk solution scatters the incident light, depolarization happens while light travels inside the scattering medium. Additionally, polarized scattering can also rotate the polarization, however the polarization rotation of the signal is assumed to be negligible because the milk solution is generally isotropic and non-birefringent.

To perform the polarization gating experiment, I need to characterize the scattering medium. I will use cow's milk as the scattering medium which is commonly used in biomedical imaging experiments. However, cow's milk usually has a known average particles sizes depending on the

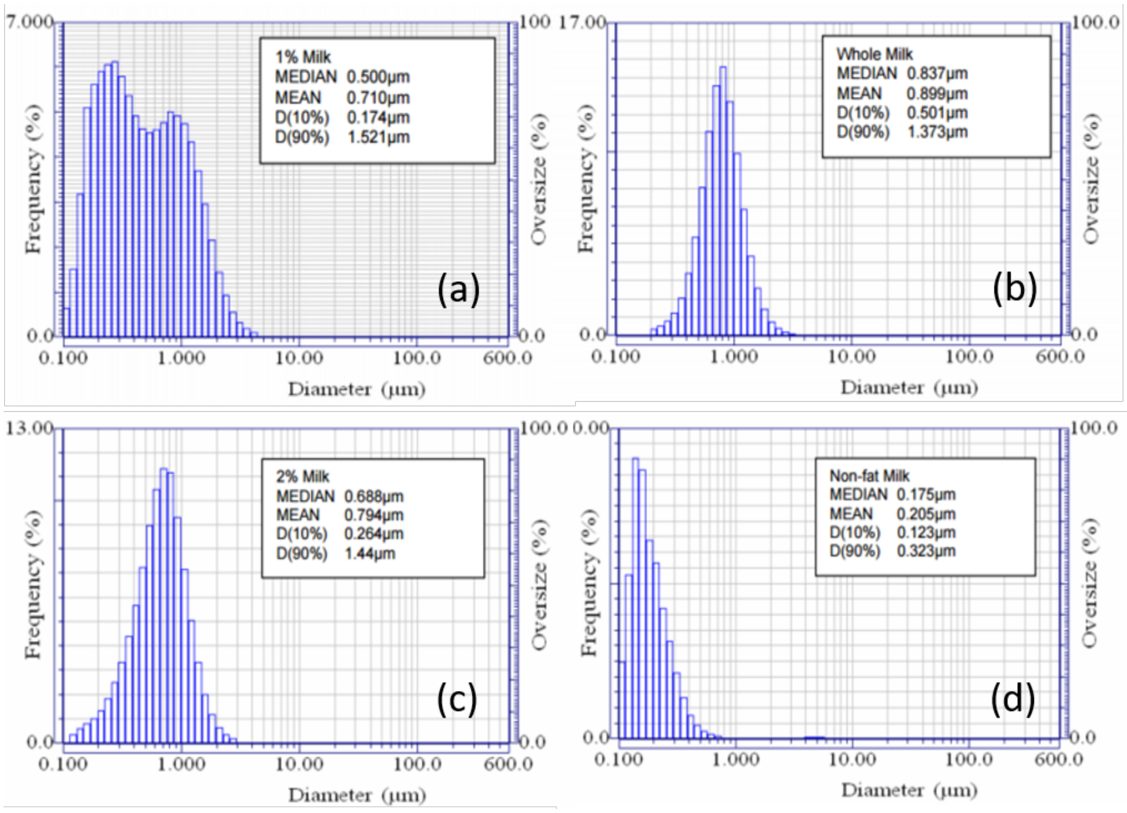

Figure 3.5: Reference measured particle size for various type of milk scattering mediums. (a) 1% milk sample with mean particle size of 0.710 μm. (b) whole milk sample with mean particle size of 0.899 μm. (c) 2% milk with mean particle size of 0.794 μm. (d) Non-fat milk with mean particle size of 0.205 μm. Courtesy of [74]

sizes of fat globules, such as a milk size study in [74] (and their results are shown in Figure 3.5). This result provides me a reference for the average milk particle sizes for my experiment. As seen in Figure 3.5, various types of milk scattering samples are compared in terms of the measured particle sizes. Their data were obtained from samples of whole milk, 1% milk, 2% milk and non-fat milk [75]. We can see non-fat milk have the smallest particle size ($mean = 0.205\mu$m) with a very narrow frequency distribution. (The frequency in the plots represents percentage of a particle particles size in the total population). To compare the samples and gain insights of the scattering characteristics, I used the scattering function tool discussed in Chapter 2.

The scattering probability functions of different types of milk scattering samples are plotted in Figure 3.6 for the various milk types analyzed in Figure 3.5. The refractive index of milk

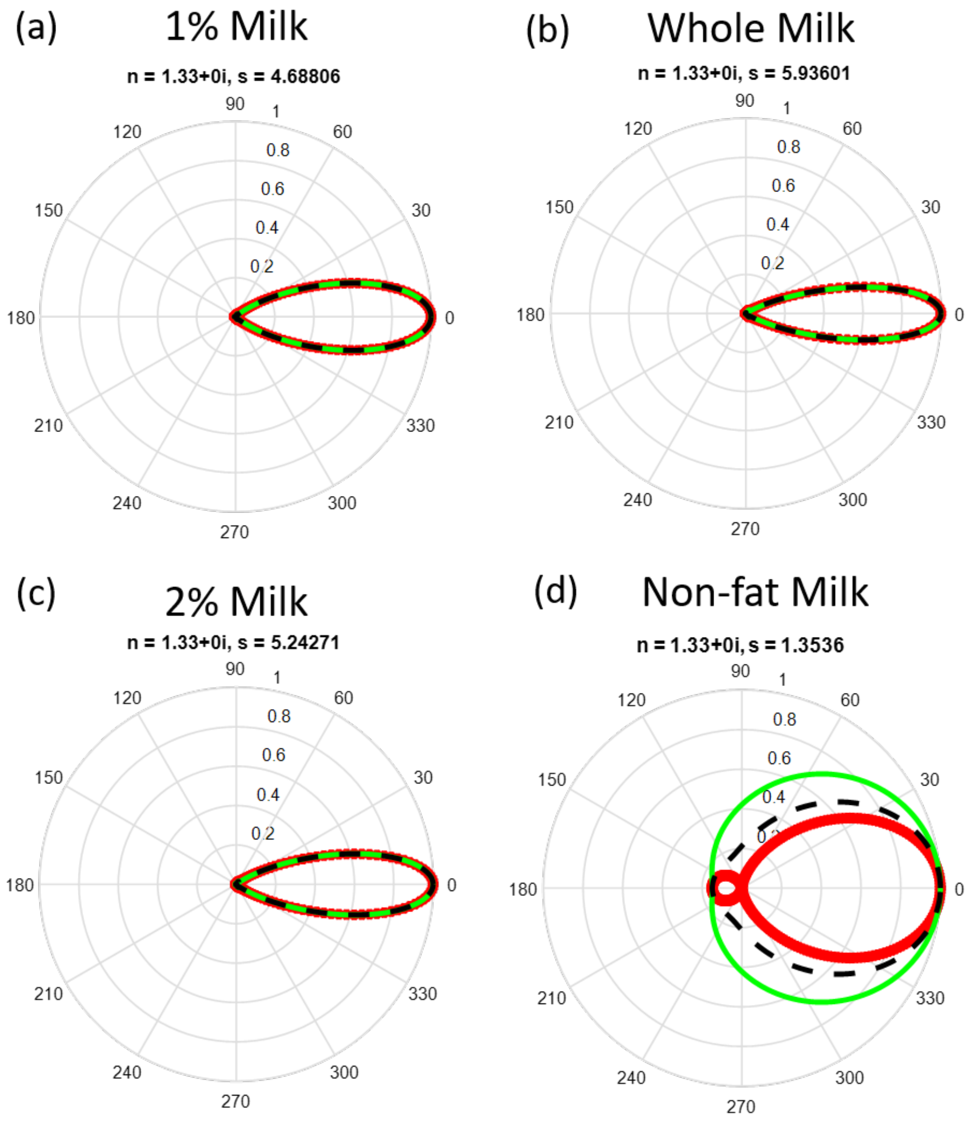

Figure 3.6: Scattering probability functions for various type of milk scattering particles. (a) 1% milk sample with mean particle size of 0.710 μm. (b) whole milk sample with mean particle size of 0.899 μm. (c) 2% milk with mean particle size of 0.794 μm. (d) Non-fat milk with mean particle size of 0.205 μm. Wavelength of illumination is assumed to be $633nm$.

particles at room temperature is assumed to be 1.338 [76] for the simulation. As demonstrated previously in Figure 3.4, for isotopic scattering medium (Rayleigh scattering regime) with small particles, DoP_L is greater than DoP_C after multiple scattering events, linear polarization persists better for an isotropic scattering medium. Because I will investigate polarization gating using linear eigen-polarization states, non-fat milk is selected as the scattering phantom which has an average measured particle diameter of 0.205 μm, shown in Figure 3.5. (Note this is similar to atmospheric LiDAR, where the wavelength of the radar signal is much longer than the size of the atmospheric particles resulting in Rayleigh scattering dominance.) In MATLAB I simulated the DoP_L and DoP_C for Rayleigh scattering using Eqn 3.32 presented previously for the non-fat milk particle of 0.205μm in size (g = 0.3), the results were shown in Figure 3.4. The plot shows a greater DoP_L than the DoP_C radiation for the non-fat milk particle size considered in Figure 3.6 (d).

Also note, by choosing to work in the Rayleigh scattering regime, the transmission of ballistic photons can be maximized among the multi-scattered photons compared to the Mie regime, since the wavelength of 632.8 nm for the HeNe laser is large compared to the 200 nm particles in the non-fat milk solution. The number of scattering depth can be on the order of 1 to 10 before the direction of propagation is randomized. However, if larger particles are used as the scattering medium, an anisotropic scattering situation will dominate hence the ballistic light which travels in straight lines is minimized. For this experiment, as shown in Figure 3.7 (b), the non-fat milk is diluted to 20% by volume by adding an appropriate amount of distilled water. Gelatin power is added to support and suspend the milk particles for a solid form of the scattering medium. We used solid scattering medium because if a liquid form of scattering medium is used (for example, diluted milk or intralipid solution), the particles will move around randomly in time and space and is sensitive to external motion turbulences and perturbations. In addition, the gain of the camera is fixed at 4 dB and the pixel frame rate is set at 30 frames/second, while the exposure times are increased for low light signals during the experiment.

The setup of the experiment is shown in Figure 3.7 (a). A 6 mW HeNe laser is used as the light source with a polarizer (P1) and a half-wave plate (HWP) to rotate the polarization linearly. P1 is fixed and HWP can be rotated for two angles in order to give orthogonally linearly polarizated illumination to the scattering tissue phantom that follows. The reason the combination of P1 and HWP are used for the input light linear polarization rotation, instead of using only P1 and P2 (P2 as analyzer), is to avoid the issue of imaging shifting seen during the experiments due to a slightly wedged polarizer. So instead of rotating P2 for $I_{||}$ and $I_{\perp}$ states, the HWP is rotated before the light is illuminated on the scattering medium. Note the input polarization of the light without the milk solution is measured to be 0.2% orthogonally polarized (which could also be due to polarization leakage from the polarizer).

The pencil laser beam propagates in the milk solution and becomes more scattered as the propagation distance increases. As shown in Figure 3.7 (b), the container for the scattering solution is made by microscope slides glued together. The top view has a V shape filled with the milk solution that allows the propagation length to continuously be varied inside the scattering medium along with an increasing $\mu_s L$ product by simply translating the sample transversely. The other side has a compensating V shape and is filled with solidified gelatin and water in order to compensate for the beam deflection caused by the wedge from the V shape milk solution side. The scattered and ballistic light coming out from the scattering medium box are passed through a second polarizer P2 which is fixed in its angle. Then the light is focused by a 250 mm focal length lens F1 into the CMOS camera. The lens should focus the ballistic light but the multi-scattered light should remain randomly distributed as seen in Figure 3.7 (c). The images are captured by a 12-bit Point Grey grey scale CMOS camera with a 70 dB dynamic range. The camera captures two images ($I_{\perp}$ and $I_{||}$ by rotating the HWP only) for each propagation length in the scattering medium. For low light experiment, the camera is shielded with a black-out cloth as shown in the setup.

The laser response intensities captured by the camera are shown in Figure 3.7 (d). As the propagation distance increases in the scattering medium, we increase the camera exposure time because the signal becomes weaker due to Beer's law. Note the exposure time is kept the same for recording the images of $I_{||}$ and $I_{\perp}$. As we can see, the initial $I_{||}$ and $I_{\perp}$ images become filled with more noise-like intensity fields which is due to the laser speckles from the narrow bandwidth HeNe laser. (This coherent laser speckle field is due to the spatial coherency of the narrow band HeNe.) For a long propagation length of 26 mm seen in Figure 3.7 (d) m)-o), which corresponds to a 21 scattering path lengths, the intensities of the laser speckle fields becomes more comparable between the $I_{||}$ and $I_{\perp}$ images. Meanwhile, the ballistic intensity peaks seen before are almost washed out

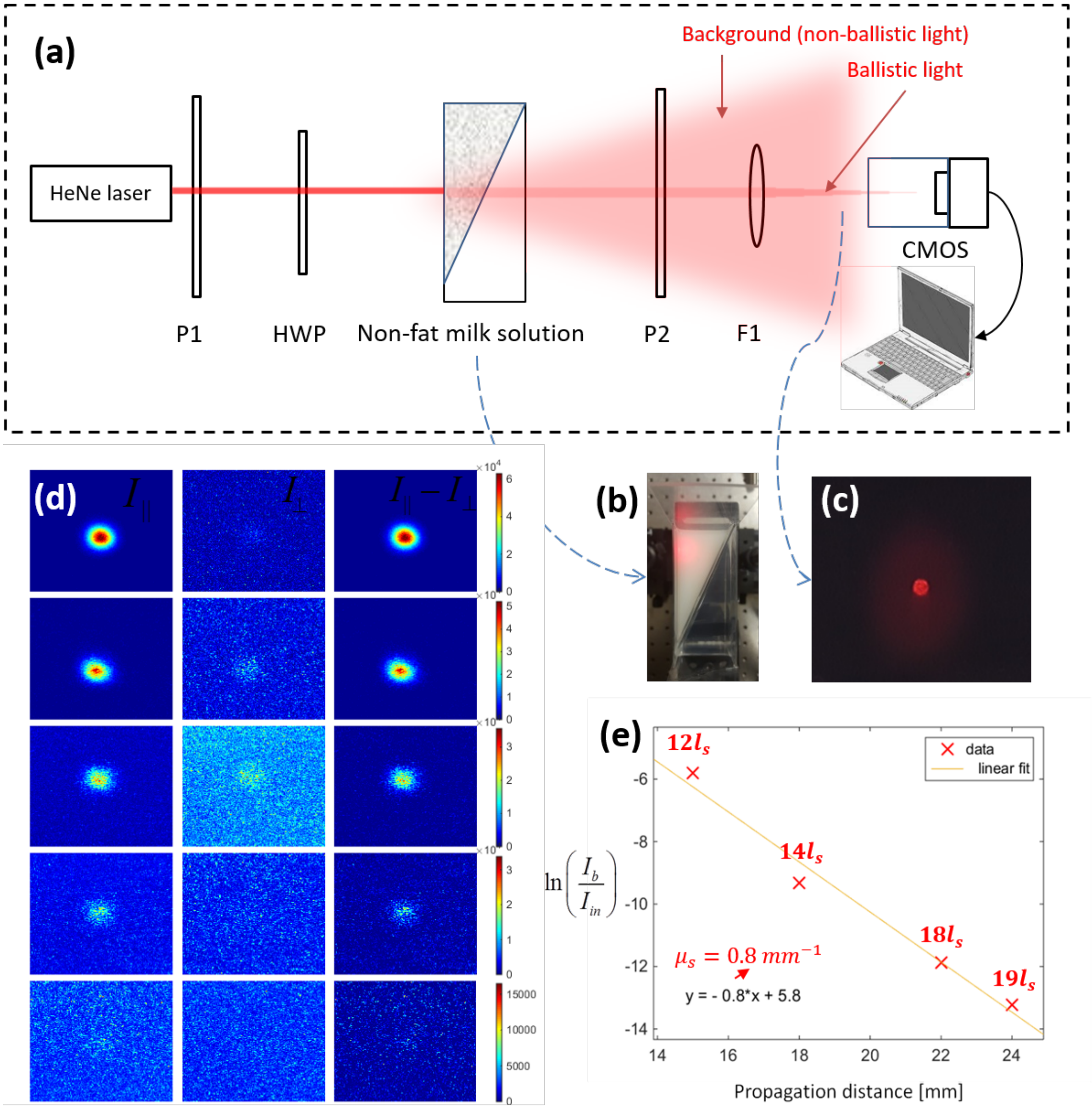

Figure 3.7: Measurement of scattering coefficient and de-polarization of ballistic light. a) Experiment setup. b) non-fat milk solution, 20% by volume, illuminated by linearly polarized HeNe laser light. c) Ballistic and multi-scattered light recorded before the Fourier transform lens F1 (focal length 250 mm). d) Images for the orthogonally input polarization light fields for different propagation distances inside the scatter medium. Rows: a) - c) 15 mm, d) - f) 18 mm, g) - i) 22 mm, j) - l) 24 mm, m) - o) 26 mm.First column are images captured for $I_{\parallel}$ field, second column are images for $I_{\perp}$ field, and third column are the differences $I_{\parallel} - I_{\perp}$, respectively. e) Computed scattering coefficient from experimental data in d): the log ratio between ballistic signal and input signal and the linear fit as a function of propagation length.

by the intense laser speckles.

However, as seen in the third column in Figure 3.7 (d), by subtracting the two response fields, the image quality of the laser does not seem to be improved much. This is because the randomly distributed laser speckles are polarized or partially polarized and they have a relatively higher intensity than the multiple-scattered light field. Hence, polarization-gated imaging technique is not efficient in this experiment setup due to the laser speckle noise caused by the spatially coherent light source. However, since my goal in this experiment was to quantitatively characterize the scattering coefficient of the tissue phantom, I continued with the experiment. The issue will be addressed in the experiment in the next section for polarization gating in the same scattering milk solution medium. (In that experiment, instead of the HeNe laser I used a Halogen lamp as light source to illuminate the scattering sample. As will be seen, the laser speckle noise is dramatically reduced for polarization gating imaging.)

In Figure 3.7 (e), I compute the scattering coefficient from the experimental data using an algorithm by fitting the $ln(I_b/I_{in})$ function with a linear line, where I_b is the peak value of the ballistic signal and I_{in} is the peak value of the input signal, both obtained from the data shown in Figure 3.7 (d). The slope of the linear fit corresponds to the value of scattering coefficient $\mu_s = 0.8mm^{-1}$, therefore the scattering length of the milk solution is $l_s = 1/\mu_s = 1.25mm$. From the calculation of scattering length based on the experiment data, this 20% milk solution is highly scattering, because for propagation lengths of 15 mm, 18 mm, 22 mm, 24 mm and 26 mm, the light experienced approximately 12, 14, 18, 19 and 21 scattering path lengths in the medium.

Referring to Figure 3.7 (d), as the exposure time is increased, the overall intensities of the laser speckle field increases with propagation length in the scattering medium. In the mean time, we see the ballistic peak intensities especially in the $I_{||}$ images decreases as the propagation length increases, while the laser speckles in the $I_{||}$ images becomes the dominating noise-like signal. Notice the ballistic peak disappears faster than the de-polarization of the ballistic light even in the highly scattering milk solution. The majority of the ballistic light remains polarized while the polarization of multi-scattered light is randomized. However, the random speckle fields persist because they are polarized. Hence, from the third column of Figure 3.7 (d), the subtraction does not efficiently result in the cancellation of the noise-like speckle fields. However, in the mean time, I can simultaneously estimate the scattering coefficient and the de-polarization character of the ballistic light with the described experimental setup. Because I obtained the μ_s measurements for the highly scattering milk sample in the Rayleigh scattering regime, the description of the polarization gating imaging in a highly scattering medium can be continued next using linear eigen-states polarimetry. (Although polarization difference imaging was previously investigated in the literature, the scattering probability function was not been considered as I analyzed in Figure 3.6 and the DoP (both circular and linear state of polarizations) was also not been considered as I computed in Figure 3.4. Hence, after thesis analysis and the scattering sample characterizations, I can perform a new polarization difference imaging experiment to analyze the image improvement specifically for small particles in the Rayleigh scattering regime.)

3.3 Experiment: Polarization-gated imaging in scattering tissue phantom

A detailed investigation of polarization-gating imaging is conducted for a highly scattering medium consists of gelatin and non-fat milk solution in the Rayleigh scattering regime, whose scattering properties were characterized in the previous experiment. The experiment setup is shown in Figure 3.8. A 250 Watt Halogen lamp (Light Ports Quartz Halogen, fiber optic bundle) is used as the illumination source. This Halogen light source is both spatially and temporally incoherent. We use non-fat milk as scattering medium as shown in the setup. The milk solution fills half of the rectangular container, hence the thickness of the scattering region decreases along the y-direction. Note polarization rotation is neglected because the milk solution is isotropic and non-birefringent. The lamp light is filtered by a 633 nm optical bandpass filter (40 nm at 3dB bandwidth) to operate in a similar and consistent wavelength regime in which the milk sample was previously characterized.

As seen in Figure 3.8, the filtered red light passes through a polarizer (P1) and a HWP before illuminating the milk scattering sample. The measured polarization extinction ratio of the system for linearly polarized light exceeds 0.26%. The object is a knife edge that is mounted in front of

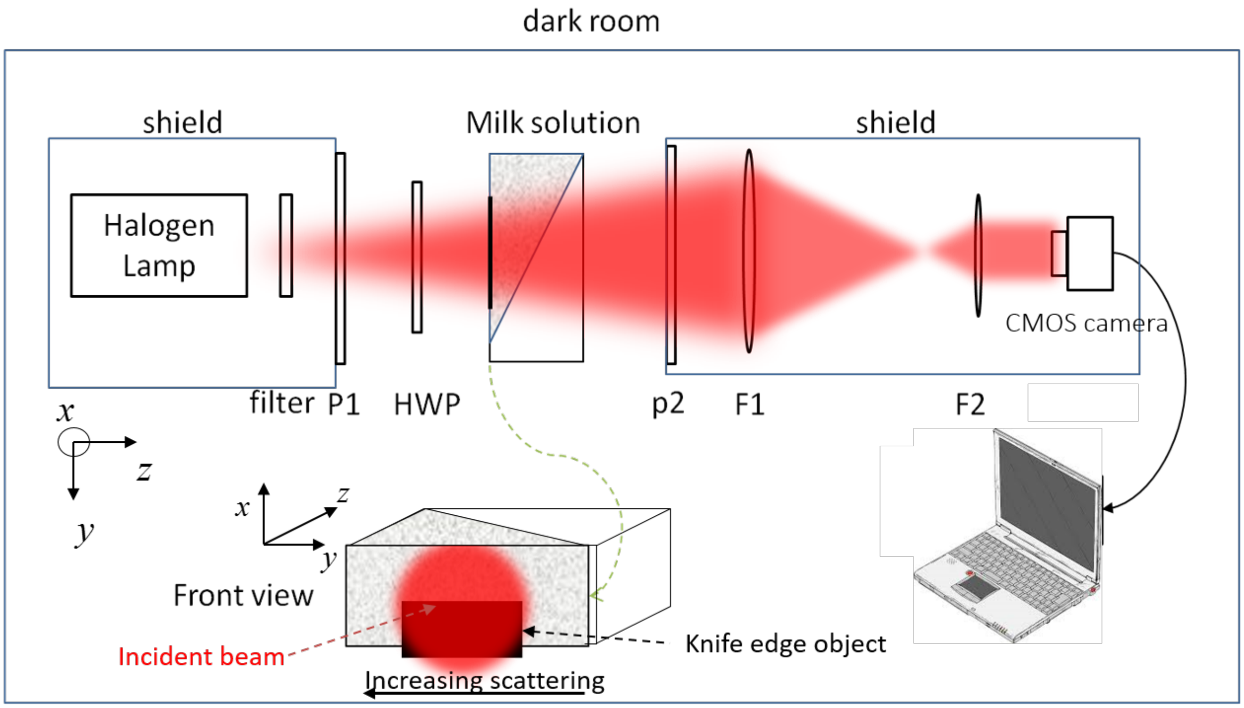

Figure 3.8: Experiment setup for polarization gating in a scattering medium.

the milk scattering sample with the front view shown in the inset. Note that the knife is along the y-direction of the increasing sample thickness (hence increasing $\mu_s L$ product). The light from the milk solution passes through polarizer P2. The imaging system consists of two lenses F1 (focal length = 250 mm) and F2 (focal length = 50 mm), yielding an magnification of $M \approx -\frac{1}{5}$. The CMOS camera is controlled by the computer for exposure time, gain and frame rate. Additionally, both the CMOS and the Halogen lamp are shielded with dark clothes to block stray light in the room that can interfere with the measurements.

Figure 3.9 shows the images obtained from the polarization gating experiment with the milk solution medium. The images a) and b) are captured with the CMOS camera (2 dB gain, 113.04 ms exposure time, 30 frames/second frame rate and 100-frames averaging). In these cases, the center of the y-direction of the image corresponds to about 15 mm of propagation distance inside the scattering medium, resulting in 12 scattering lengths l_s (l_s = 1.25 mm for this milk solution from the characterization). In the $I_{\|}$ component of the total response light field shown in Figure

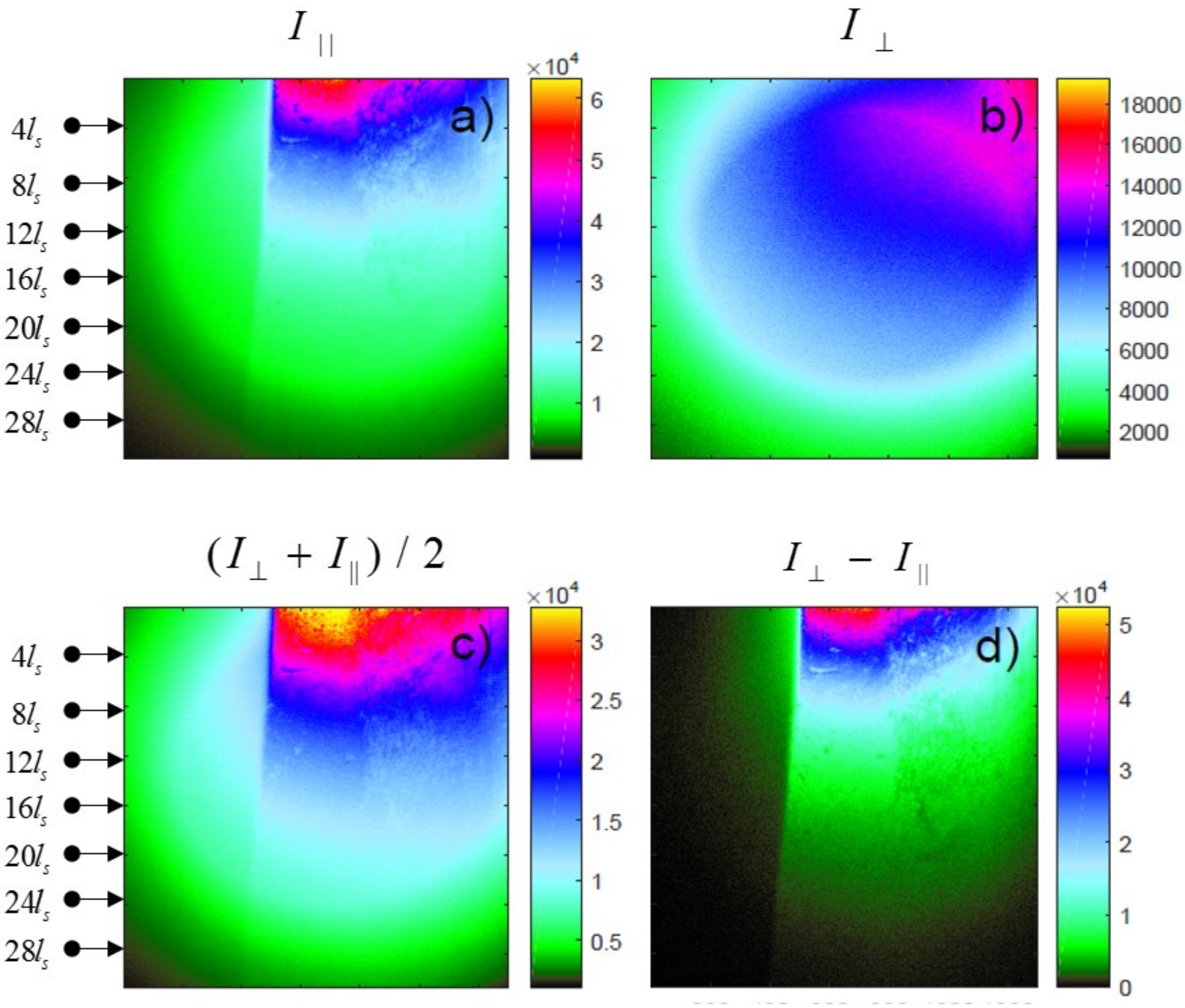

Figure 3.9: Image results for polarization gating experiment in a milk scattering medium captured by CMOS camera. a) $I_{\|}$ response light field, b) $I_{\perp}$ response light field, c) c) $I_{\|} + I_{\perp}$ polarization sum light field and d) $I_{\|} - I_{\perp}$ polarization difference light field, respectively.

3.9 a), as propagation in the scattering medium increases, the contrast of the imaged knife edge decreases as a result of the increasing $\mu_s L$ product. This represents the best case scenario for conventional imaging. However, since the $I_{\|}$ component includes both ballistic light and half of the randomly polarized multi-scattered light, the image is blurred by a strong background caused by the scattered light. On the other hand, the $I_{\perp}$ component of the total response light field shown in Figure 3.9 b) represents half of the randomly polarized multi-scattered light, hence no image of the knife edge can be observed because the image information in the multi-scattered light is similar in all states of polarizations.

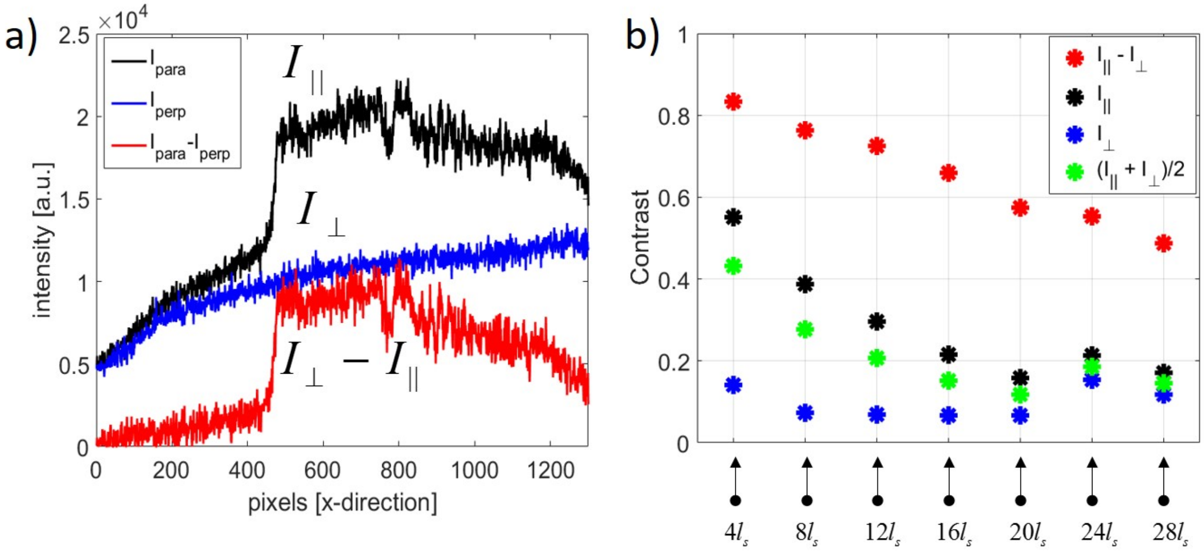

Figure 3.10: a) cross-section line plots at $12l_s$ for $I_{\|}$ (black line), $I_{\perp}$ (blue line) and $I_{\|} - I_{\perp}$ (red line), respectively. b) Image contrast comparison for $I_{\|} - I_{\perp}$ (red dots), $I_{\|}$ (black dots), $I_{\perp}$ (blue dots) and $(I_{\|}+I_{\perp})/2$ (green dots), respectively, as a function of propagation length in the scattering sample.

As seen in Figure 3.9 d), we obtain an approximate estimate of the ballistic light in the image with an improved visibility of the knife edge object through a highly scattering medium. With this simple polarization gating technique, the randomly polarized multi-scattered background is eliminated in the image by the subtraction operation. Compared with the $I_{\|}$ and $I_{\perp}$ images, the polarization-gated image shows a significantly improved contrast hence better visibility of the knife edge object after the light field propagates through a highly scattering medium with approximately 12 scattering path lengths. In addition, to gain a better view of the contrast improvement using this polarization difference imaging technique, the cross-sectional lines are plotted in Figure 3.10 a) for $12l_s$ through the scattering milk solution. The polarization difference image $I_{\|} - I_{\perp}$ improves the image contrast compare to either $I_{\|}$ or $I_{\perp}$ images. The contrast for the $I_{\|}$, $I_{\perp}$ and polarization-gated $(I_{\|} - I_{\perp})$ images are calculated and plotted in Figure 3.10 b) for comparison. The polarization difference image containing high contrast information is extracted by subtracting the $I_\perp$ from the $I_\parallel$ response field, while the randomly polarized multi-scattered light is suppressed. The edge contrast are calculated for the scattering region between $4l_s$ and $28l_s$.

The polarization gated image (indicated by red dots) yields the best contrast among these three detection schemes. Note that although the contrast decreases for all three cases as the propagation length increases in the scattering medium, the contrast ratios jump at $24l_s$ for both the $I_\parallel$ and $I_\perp$ components. This is due to the influence of the intensity profile of the multi-scattered light around the region of $24l_s$, which is subtracted away in the $I_\parallel - I_\perp$ case. In this experiment, the image contrast improvement is demonstrated for a knife edge object using polarization gating for optical imaging in a highly scattering milk sample. The results were compared with conventional imaging. Hence, we can use polarization-gating to improve the image contrast because the ballistic light is enhanced while some of the multi-scattered light is suppressed in the gating process.

3.4 Discussion

There also has been theoretical predictions showing that circularly polarized light can maintain its state of polarization longer than other state of polarizations in a highly scattering medium for larger particles in the Mie scattering regime [57, 52, 53, 54]. To perform polarization gating in scattering medium such as the brain, an polarized, bright and tunable light source is desired. This provides part of our motivation for investigating the Raman soliton in supercontinuum generation that provides a polarized, broadband and tunable light source for polarization gating in scattering medium. Hence, a circularly polarized Raman soliton output could be used as a tunable and stable light source for investigating polarization gating in a scattering medium. In Chapters 6 and 7, the detailed investigations of the broadband supercontinuum light source will be described.

In summary, the visibility improvement of polarization-gated imaging using polarimetry of linear eigen-states in a highly scattering medium was experimentally demonstrated. The concept was originally inspired biologically during animal behavior studies of certain fish and insects that relies on polarization difference signals generated in the double cones to navigate in scattering environments.

A theoretical framework for polarization difference technique was developed by computing the point spread function of the Rayleigh and Mie scatterers. The theoretical resolution improvement is very similar for the two types of scatterers by comparing my simulation results with the published results for single scattering case. A photon-tracking Monte Carlo simulation can be used to simulation the PSFs for multiple scattering situations. I also analyzed the depolarization characteristics of multiple scattered light using coherency matrix method developed previously. The degree of polarization can be computed and the simulation results indicate that the DoP of linearly polarized radiation out-performs the DoP of circularly polarized radiation for Rayleigh scattering particles. In addition, a method measuring the scattering coefficients of the non-fat milk sample operating in Rayleigh scattering regime for polarization gating experiment was developed. In the experiment, polarization-gating technique was demonstrated to have up to 11 times improvement of image contrast for a knife edge object comparing to conventional imaging techniques. The ballistic light which contains high contrast information is extracted by subtracting the $I_{\perp}$ from the $I_{\|}$ response field, while the randomly polarized multiple-scattered light is eliminated from the background.

Chapter 4

Dynamic structured illumination microscopy

4.1 Background of structured illumination microscopy in scattering medium

Imaging in multi-scattering medium is highly challenging because the lateral and axial localization of objects suffers from scrambled light propagation effects caused by the scattering particles. In recent years, there is major progress for optical imaging in scattering medium using structured illumination technique. Sample illumination is one of the most important aspect in optical imaging to achieve high quality images. In history, the field of illumination has evolved significantly in the past century. Nelsonian illumination (or critical illumination), developed by microscopist Edward Nelson, was predominantly used to create a bright illumination by using a condenser to focus the image of the light source onto the object. However, as a trade-off, Nelsonian illumination usually suffers from unevenness of the illumination due to the inclusion of the image of the light source that becomes visible in the final image plane. Köhler illumination was proposed in 1893 by August Köhler [77] for creating an extremely uniform sample illumination to reduce image artifacts such as glare in the case of Nelsonian illumination. Since then, Köhler illumination has been widely used in modern scientific microscopy. Image qualities can be further improved by aberration corrections through superior lens design and manufacture. Over the years, we have seen significant developments in sample illumination to reduce background light and to improve image resolution. Examples include oblique illumination microscopy using an optimum illumination angle to see more details in a sample, light sheet microscopy using side line-scanning illumination to block out-of-focus background light and confocal microscopy (an established standard microscope) using a pinhole or a focused laser beam to achieve high resolution imaging.

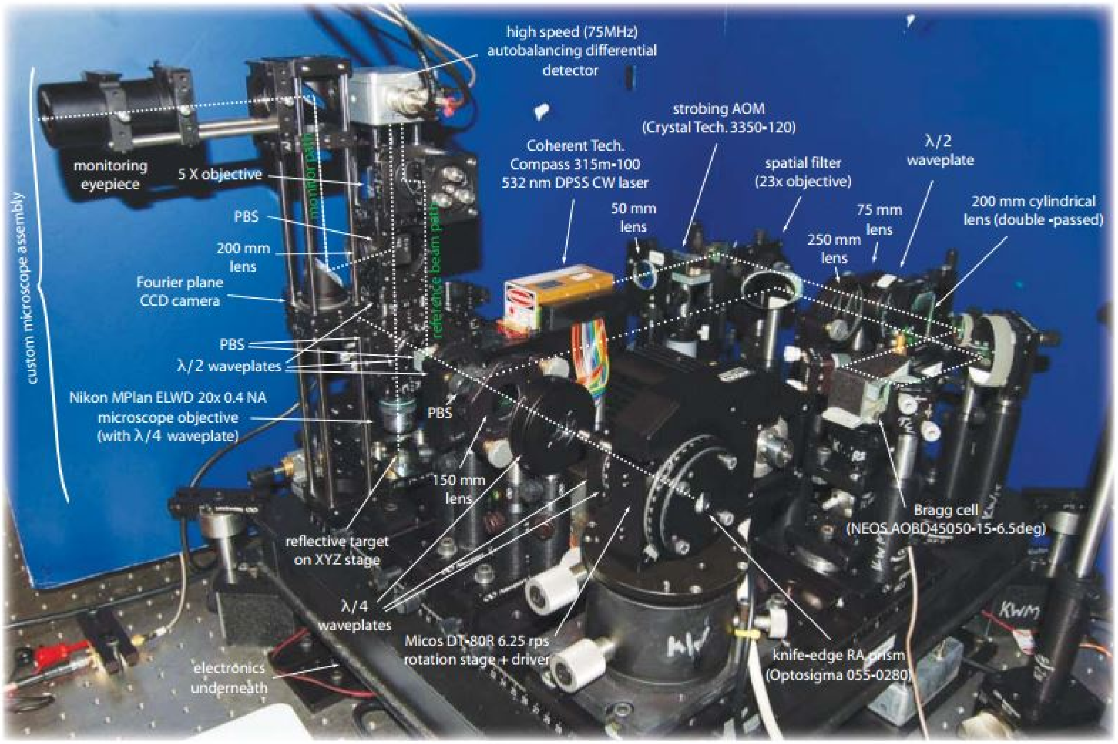

Figure 4.1: Experiment setup of DEEP developed in our laboratory. Adapted from Dr. Daniel Feldkhun's thesis [78]

Recently, research has focused on modifying uniform illumination to create a variety of structured illuminations. Structured illumination evolved from synthetic aperture imaging, which was first demonstrated fifty years ago [79, 80]. In 1997, sinusoidal structured illumination was incorporated into a conventional microscope to obtain optical sectioning [81]. In 2000, a revolutionary sinusoidal structured illumination microscopy (SIM) was proposed, breaking Abbe's diffraction limit by a factor of two [82]. The field of SIM has since experienced major advances in optical sectioning for thick specimens [81, 83, 84, 85], super-resolution microscopy [82, 86, 87, 88, 3, 89, 90, 91, 92], whole-field non-contact surface topography [93, 94, 95, 96, 97, 98, 99, 100, 101, 102] and phase imaging [103, 104, 105, 106, 107, 108]. The rapid development of SIM also attracted significant efforts to enhance image contrast and spatial resolution in scattering media such as deep biological tissue [109, 110, 111, 112, 113, 114, 115].

Recently, a novel Fourier synthesis imaging method called doppler encoded excitation pattern microscopy (DEEP) was demonstrated [116]. This wide-field imaging technique employs moving structured illumination patterns generated by an acousto-optic deflector (AOD) and tomographic image reconstruction algorithm and is capable of detecting both fluorescent and scattered light [78]. A thousand-fold improvement of the depth of field is achieved for two-dimensional high resolution proof-of-concept experiments compared with conventional microscopy. In the following section, the concept of a dynamic structured illumination microscope for Fourier domain imaging will be presented, followed by analysis of the principles of AOD for moving illumination pattern generation.

4.1.1 Fourier synthesis of objects and Moiré pattern formation

The Fourier decomposition of spatial frequencies combined with the theory of Moiré pattern forms the basis of the dynamic structured illumination microscopy (DSIM). Abbe's image formation theory implies that an object's spatial information can be decomposed into a number of interference patterns with different spatial frequencies. A Moiré pattern is a beating effect due to the interference between two spatial patterns. It is often seen in fabrics, computer graphics, and digital images. Spatially structured excitation light was used in a wide-field and non-confocal microscope [117, 86, 82] to extract normally inaccessible high frequency information encoded in the form of Moiré patterns. Hence, for an object with a high spatial frequency variation across its shape, if we superimpose (multiply) it with another high spatial frequency pattern, the product will contain an interference beating in the form of the Moiré pattern. The Moiré pattern is a signal with low spatial frequency detectable to reconstruct a high spatial frequency object. Note that the temporal analogy of the Moiré pattern is a heterodyne mixing method in signal detection.

DEEP microscopy developed in our research group is a Fourier domain imaging method that probes the Fourier component of an object to form a synthetic wide-field image [116]. It is similar to SIM but also fundamentally different in terms of illumination generation and signal detection.

Figure 4.2 illustrates the general concepts of a standard SIM versus a DEEP microscope. The stationary illumination patterns of SIM can be generated by a spatial light modulator (SLM)

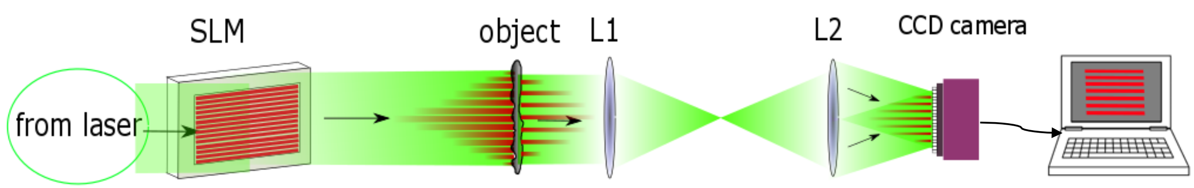
Conventional structured illumination microscopy

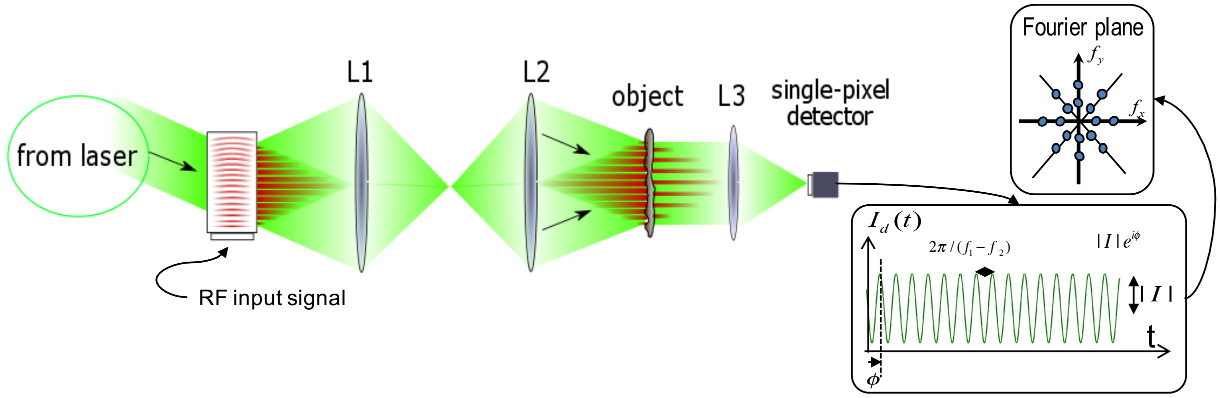
Dynamic structured illumination microscopy

Figure 4.2: Comparison of conventional (top) and dynamic structured illumination microscopy for illumination pattern generation and signal detection techniques (bottom).

or a digital light projector. Usually three different projection patterns with different phases of 0^o, 120^o, and 240^o are needed to reconstruct the SIM signal. A CCD camera can be used to detect and collect the three images. Instead of a stationary illumination pattern, DSIM uses AOD that generate moving patterns running across the object at the acoustic velocity scaled by the magnification factor of the optical imaging system. The correlation signal between the object and the illumination pattern is then collected by a lens and can be detected by a single-pixel camera or a high speed photodiode detector. As illustrated in Figure 4.2, the spatially integrated detected signal sinusoidally oscillates in time, and its spatial Fourier transform corresponds to a pair of dots on the Fourier slice oriented at an angle determined by the angle of illumination pattern.

If the object is illuminated by patterns with different spatial frequencies generated by the

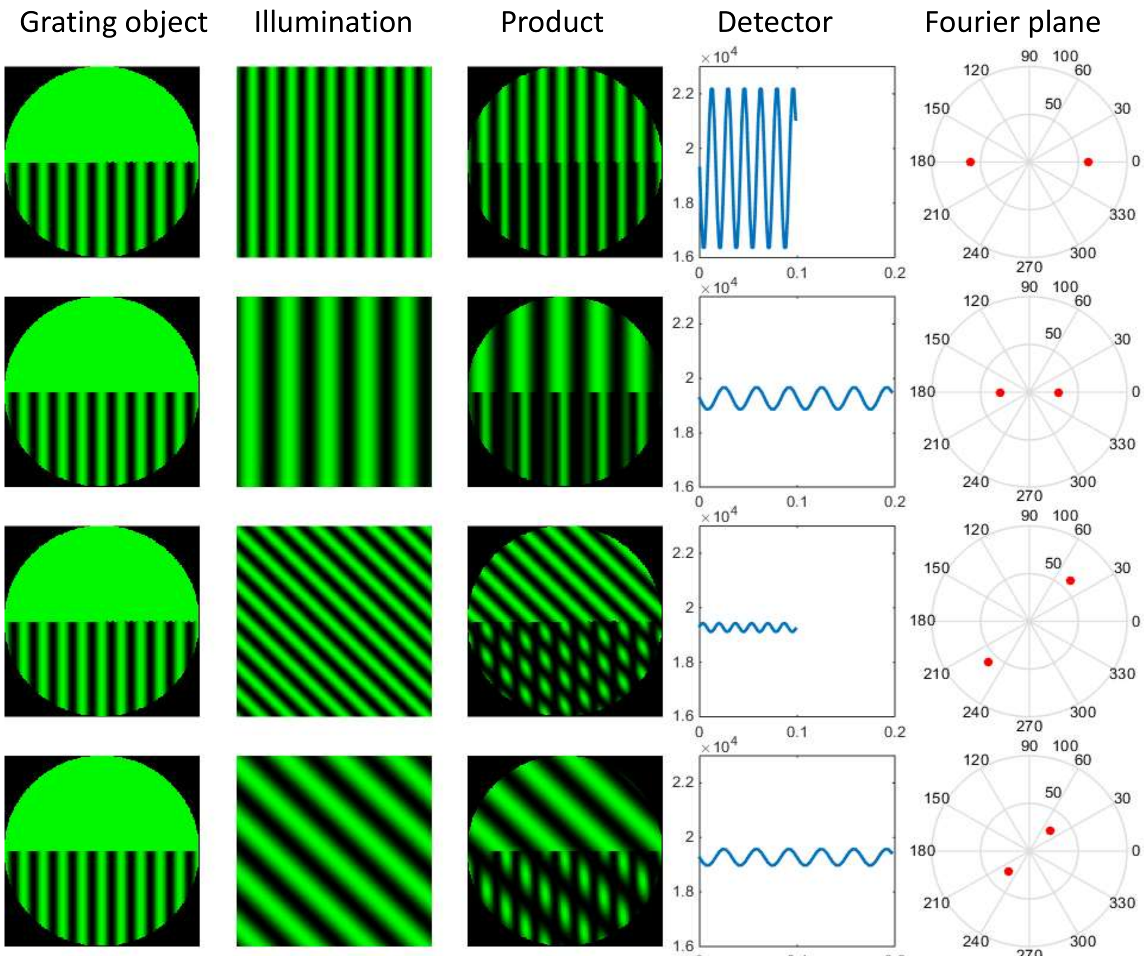

Figure 4.3: Graphical illustration of the dynamic structured illumination microscopy from the illumination to signal detection process. First column: amplitude object patterns; second column: illumination patterns generated by an AOD; third column: product between the object pattern and the illumination pattern; fourth column: time domain detector signal; fifth column: Fourier transform of the detector signal represented in the Fourier domain.

AOD, the detector signal varies in both amplitude and phase. To illustrate the process of illumination pattern generation to signal detection in DSIM, a graphical simulation is performed using MATLAB. As shown in Figure 4.3, the object is half-transmissive and half-filled with amplitude grating lines. The four moving illumination patterns shown in column 2 generated by the AOD have different spatial frequencies and orientations. When the patterns are illuminated on the grating object, the products between the moving pattern and the object are shown in the third column.

If the grating frequency exactly matches the illumination frequency, we observe a beating between the two, which is a Moiré pattern that blinks on and off as the illumination moves across the object. The detector, being either a single-pixel camera or a photodiode, integrates the intensity response spatially and can be measured with an oscilloscope. A sinusoidal signal can be observed on the scope, and its Fourier transform corresponds to a pair of dots on the Fourier slice with its angle defined by the orientation of the illumination. Note that the amplitude of the temporal detector signal corresponds to the strength of matching between the illumination signal and the Fourier component of the object, while the relative phase shift between the illumination and the object Fourier component is represented by the phase of the complex Fourier points in the Fourier domain slice. To differentiate the measured temporal signals in row 2 versus row 4, the phase information and the illumination orientation angle are required. The reference point of phase for the measurements can be chosen at a point where the first set of acoustic signal has just completed its propagation inside the Bragg crystal cell, which would be on the order of several μs. The principles of the AOD will be described in the next section.

4.2 Acousto-optic devices for active illumination pattern generation

The acousto-optic effect is one of the most interesting phenomenons associated with light and sound interactions. The acousto-optic interactions allow the manipulation of laser beams and high speed signal processing without mechanical moving parts [118]. It can be modeled by the coupled-mode equations, and it is used for applications such as acousto-optic modulators (AOM), acousto-optic deflectors (AOD), and acousto-optic tunable filters (AOTF). The AOD can be used to generate a moving illumination pattern for DSIM. Hence, it is essential to understand the principles of AOD as a novel illumination pattern generator. In this section, the principles of AOD will be investigated mathematically and will be represented in K-space.

The AOD consists of a piezoelectric transducer and a photoeleastic material. When an RF signal within the acoustic bandwidth of the crystal is launched into the AOD through the transducer, the acoustic waves generated by the transducer travel through the photoeleastic material.

A traveling volume grating due to the periodic refractive index modulation will diffract the collimated input optical wave that satisfies the Bragg alignment condition. For applications involving the diffraction of laser beams using AOD driven by an RF signal, the time-bandwidth product (TBP) becomes important because it determines the maximum number of resolvable Fourier spots in the far field of the AOD along the linear slice through the Fourier domain. The TBP is equal to the product between the acoustic propagation time across the laser beam and the frequency bandwidth of the AOD.

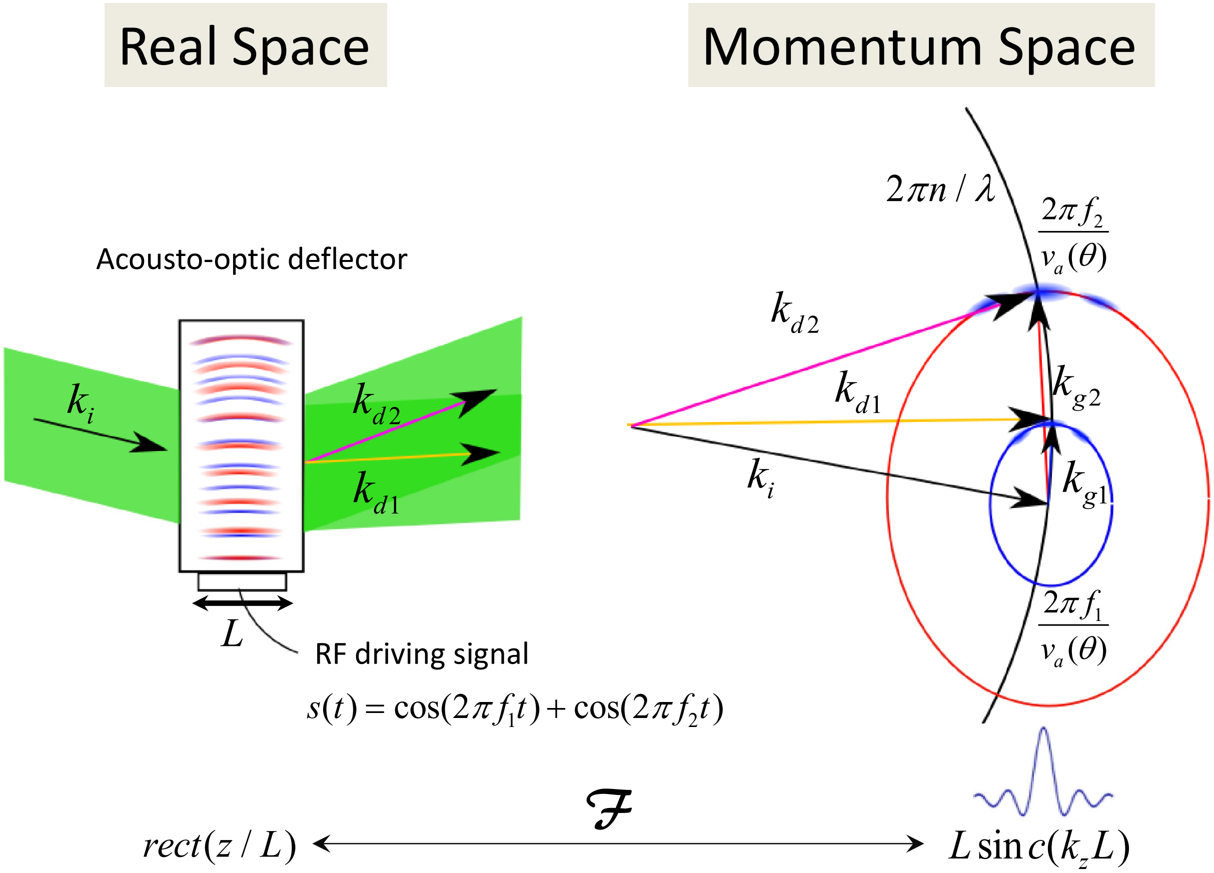

Figure 4.4: Momentum space (scaled K-space) representation of the principles of AOD for moving illumination pattern generation. Color-codings for k-vectors: black arrow: input light beam; pink and yellow arrows: first-order deflected beams from the AOD; red and blue arrows: grating waves generation from Bragg matching in the AOD. L: aperture width of crystal inside the AOD. s(t): RF driving signal with two tones f_1 and f_2.

As shown in Figure 4.4, when an RF driving signal is applied to an AOD, the piezoelectric transducer that is bonded to a crystal inside the AOD launches an acoustic wave. Due to the photoelastic effect, the acoustic wave induces periodic perturbation of the refractive index in the form of a wave. A traveling-wave volume grating perturbation is created inside the crystal. Light can be efficiently diffracted if the input light is launched into the AOD at the appropriate Bragg diffraction angle, which is determined by the Bragg matching condition,

$$\sin\theta_B = \lambda/2\Lambda_a \tag{4.1}$$

where λ is the wavelength of the input light in the crystal, Λ_a is the wavelength of the acoustic wave, $\Lambda_a = v_a/f_a$, and θ_B is the Bragg matching angle as illustrated in Figure 4.4. v_a is the velocity of the acoustic wave in the crystal, and f_a is the frequency of the acoustic wave and $f_a = \frac{\Omega_a}{2\pi}$. Note that Ω_a is the acoustic angular frequency. The Bragg condition is derived from the momentum and energy conservation principles, which can be better understood in k-space (wave vector space) and K-space (momentum/grating space) for an isotropic crystal for simplicity (the anisotropic case will be illustrated in the following section). Because the Bragg matching angle is given by,

$$\theta_B = \sin^{-1}\lambda/2(v_a/f_a) \approx \lambda f_a/2v_a \tag{4.2}$$

The Bragg angle θ_B is proportional to the frequency of the acoustic wave. This result is important for the generation of the diffraction signal. As shown in Figure 4.4, if the AOD is driven by an RF signal $s(t)$ consisting of two temporal frequencies f_1 and f_2,

$$s(t) = \cos(2\pi f_1 t) + \cos(2\pi f_2 t) = \frac{1}{2}(e^{i2\pi f_1 t} + e^{i2\pi f_2 t}) + c.c. \tag{4.3}$$

where *c.c.* represents the complex conjugate. The width of the crystal inside the AOD is L. When a collimated laser beam k_i illuminates the AOD at the Bragg angle, the beam is diffracted into a pair of two first order beams, represented in k-space by k_{d1} and k_{d2}, respectively. In k-space, two traveling wave gratings k_{g1} and k_{g2} that satisfy the Bragg condition are generated. Each diffracted beams's vector tip distributes in a *sinc* uncertainty box due to the finite crystal size L and Fourier uncertainty principle. The uncertainty of the movement of the k-vector tip is $2\pi/L$. In the K-space (grating space), which is represented in the blue curves in Figure 4.4 on the right, the shape of the *sinc* box is printed on the K-space curves. The grating vectors k_{g1} and k_{g2} distribute in where the printed *sinc* and the k-space circle intersect. The pair of grating vectors interfere and generate a traveling wave beat signal: $B(x,t) = \cos(2\pi f_b(\frac{x}{v_a} - t))$, where the beat frequency $f_b = |f_1 - f_2|$.

In DSIM, the spatial fringes are generated by an AOD and then optically projected to the object through an optical imaging system. When probed by a moving fringe, a matching Fourier component of the object can be probed through the spatial convolution with the illumination fringe. An object can be probed by a number of moving interference patterns with a range of orientations and periods. These patterns can be considered as fringes with different periods moving in different directions. Since the object is a coherent sum of gratings/fringes, by probing the object with a succession of moving gratings, we are essentially performing spatial Fourier domain convolutions between the probing Fourier components and the object Fourier components. Additional Fourier slices can be measured by rotating the illumination pattern or the object as illustrated in Figure 4.3.

The beat signal is encoded on the laser carrier and optically projected on the object through an imaging system. The signal is a moving fringe pattern with a velocity of v_a. As shown previously, the temporal frequency of the fringes depends on the RF driving frequencies. In summary, the AOD diffracts the input light into a pair of coherent first-order beams when the Bragg condition is satisfied. The interference of the two beams is a running fringe pattern with a beat frequency f_b. The fringe pattern is illuminated on the object to spatially probe its Fourier components spatially. By driving the AOD with a range of RF frequencies, we generate fringe patterns with a succession of spatial frequencies, hence a wide range of Fourier components of the object can be probed. The voltage power is given by $P(t) = |s(t)|^2 = Acos^2(2\pi(f_1 - f_2)t) = Acos^2(2\pi f_b t)$. The detector signal received by a single element detector (a single-pixel camera or fast photodiode detector) can be written as the following,

$$\begin{aligned} I_d(t) &= \iint\limits_A I_{obj}(x,y)cos^2(2\pi(f_1-f_2)(t-\frac{x}{v_a}))\,dx\,dy \\ &= \iint\limits_A I_{obj}(x,y)e^{i2\pi\left(f_1-f_2\right)\left(t-\frac{x}{v_a}\right)}\,dx\,dy + c.c. + DC \\ &= e^{i2\pi f_b t}\mathcal{I}_{obj}(f_x,f_y)\star\delta(f_x\pm\frac{f_b}{v_a},f_y)\Big|_{f_x=0,f_y=0} + DC \\ &= e^{i2\pi f_b t}\mathcal{I}_{obj}(\frac{f_b}{v_a},f_y) + e^{-i2\pi f_b t}\mathcal{I}_{obj}(-\frac{f_b}{v_a},f_y) + DC \end{aligned} \tag{4.4}$$

From Eqn. 4.4, we see that the detector signal is the spatial integration of the product between the object and the moving sinusoidal illumination pattern. In the Fourier domain, this corresponds to the convolution between the complex spatial Fourier transform of the object $\mathcal{I}_{obj}(f_x,f_y)$ and the complex spatial Fourier transform of the moving illumination pattern $\delta(f_x\pm\frac{f_b}{v_a},f_y)$. Hence if we illuminate the object with a series of spatial frequencies, the Fourier coefficients can be probed and measured using Fourier synthesis, and the images of the object can be reconstructed.

4.3 Experiment: Dynamic structured illumination microscopy by interfering two first order beams

The previous polarization interferometric DSIM experiment utilizes the interference between the 0^{th} and the 1^{st} order diffracted beams from the AOD. However, we can modify the setup for the interference between the two 1^{st} order beam for double sideband chirped-mode operation, to enable a frequency sweep down to DC level for improved object detection. In this experiment, we change the light source from the low power HeNe laser to a 665 nm laser diode (Mitsubishi Electric Corp, 101J8-01), which has a maximum average output power of 40 mW. The laser diode is configured, the temperature is stabilized and it operates in the constant current mode. The RF input signal to the AOD is generated by a DDS (Analog Devices, AD9910). The DDS is configured to generate a phase coherent chirp signal of 10 MHz/2 ms, resulting in a beat frequency of 20 MHz.

As shown in Figure 4.5, the output of the DDS is split into two channels using an RF splitter with one channel sent to the digital oscilloscope and the other sent to an RF attenuator and then to

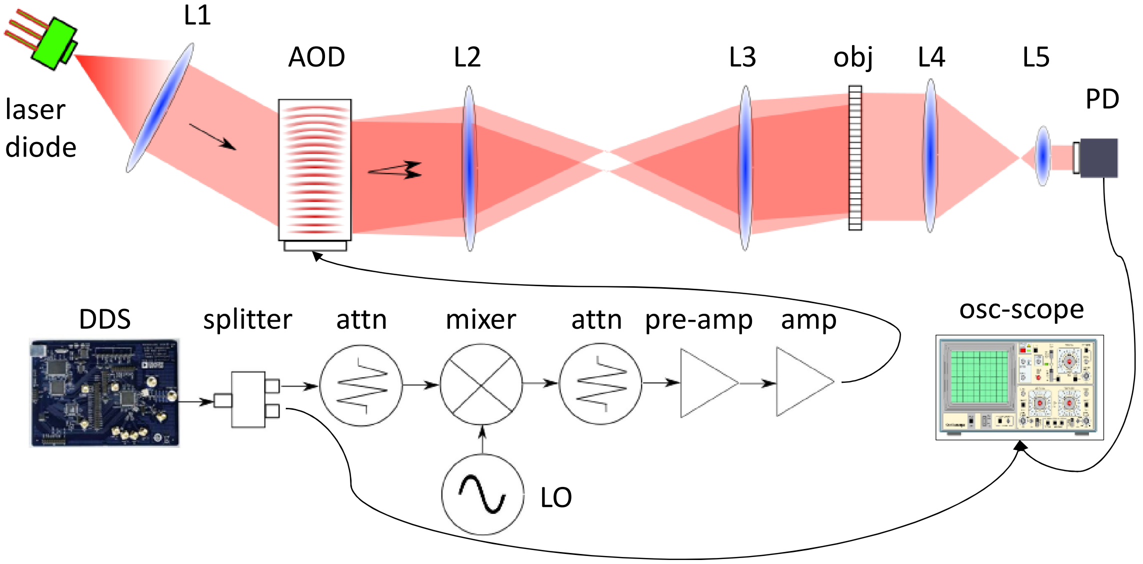

Figure 4.5: DSIM experiment setup by interfering two first-order diffracted beams from the AOD. The DDS is configured to output a phase-coherent chirp signal. DDS: direct digital synthesizer, Attn: RF attenuator, LO: RF local oscillator, pre-amp: RF pre-amplifier, amp: RF amplifier, obj: Ronchi ruling grating object, PD: high speed photodiode detector, osc-scope: digital oscilloscope.

the IF port of the RF mixer. A 7 dB RF attenuation is configured to avoid nonlinearities in the RF mixer because it is a nonlinear device, and we observed saturation behavior of the mixer previously. For the RF mixer to operate in the linear regime, the LO and IF input powers are adjusted to obtain minimum harmonics monitored by an RF spectrum analyzer for a 10 MHz single-tone signal from the DDS.

Then we switched to the chirp mode setup on the DDS and used the digital oscilloscope to check the shape of the chirp signal after the RF pre-amplifier. The local oscillator sends a 50 MHz single-tone signal to the LO port of the mixer, and the RF output port of the mixer is a 50 MHz carrier modulated by the 10 MHz / 2 ms frequency chirp. The output of the RF amplifier is then coupled to the AOD. The two 1st order diffracted beams are overlapped in the optical system and imaged onto the Ronchi ruling grating object by a 4F imaging system formed by L_2 and L_3 with a magnification factor of -1. The product of the moving illumination signal and the grating object is then collected by a pair of lenses L_4 and L_5 to a fast photodiode detector with a 60 MHz bandwidth.

The temporal output signal of the photodiode detector is then sent to the digital oscilloscope and is synchronized by the trigger output signal from the DDS. Additionally, the detector signal, the DDS trigger signal and the chirp signal are recorded by the oscilloscope and imported to MATLAB for post-data processing and signal reconstruction, which will be discussed in the next section.

4.3.1 Signal reconstruction using the Matched-filtering algorithm

As shown in Eqn. 4.4, the temporal detector signal can be considered a convolution between the spatial Fourier transform of the object and the Fourier transform of the chirp signal. Hence, to reconstruct the shape of the amplitude grating object, the detector signal needs to be convolved with the conjugated chirp signal. The double sideband chirp signal from the DDS can be expressed as the following,

$$c(t) = cos(2\pi bt^2) + D.C. \tag{4.5}$$

The double sideband detector signal can be written as,

$$s(t) = cos(2\pi 2b(t-t_0)^2) + D.C. \tag{4.6}$$

where b is the chirp rate (MHz/ms), t is the time delay, and t_0 is the time delay constant due to the acoustic propagation delay in the AOD crystal. The algorithm I developed for reconstructing the signal using the matched filter can be summarized as follows:

(1) Frequency double the chirp signal $c(t)$:

$$c(t)|_{2f} = c(t)^2 = (e^{i2\pi bt^2} + e^{-i2\pi bt^2})^2 = e^{i2\pi 2bt^2} + e^{-i2\pi 2bt^2} + D.C. = cos(2\pi 2bt^2)$$

(2) Fourier transform the double sideband chirp signal:

$$C(f)|_{2f} = F\{c(t)|_{2f}\} = F\{cos(2\pi 2bt^2) + D.C.\}$$

(3) Fourier transform the detector signal:

$$S(f) = F\{s(t)\} = F\{cos(2\pi 2b(t-t_0)^2) + D.C.\}$$

(4) Correlation between the spectrum signals $C(f)$ and $S(f)$ to obtain the Fourier transform of the grating object:

$$G(f) = F\{g(t)\} = C^{*}(f)|_{2f}S(f)$$

(5) Inverse Fourier transform the correlation signal to obtain the reconstructed object:

$$g(t) = F^{-1}\{F\{g(t)\}\}$$

After performing the matched filter algorithm on the measured detector signal in MATLAB, the reconstruction results are summarized in Figure 4.6. Figure 4.6 a) is the truncated version of the 10 MHz/2ms chirp signal measured by the oscilloscope for the DDS output signal. The corresponding Fourier transform of the chirp signal is shown in Figure 4.6 b). The detector signal measured by the oscilloscope is plotted in Figure 4.6 c), where we see multiple harmonic frequency peaks representing the Fourier harmonic orders for the rectangular-shaped grating object. As shown in Figure 4.6 d), the Fourier transform of the detector signal consists of multiple peaks with amplitudes depending on the inverse of the order of the harmonics. The inverse Fourier transform of the correlation between the conjugated chirp spectrum and the DSIM signal spectrum is shown in Figure 4.6 e), which represents the matched-filter reconstruction of the grating object. To confirm the signal reconstruction, an image of the grating object illumination by the laser diode is recorded by a CCD camera. The comparison of the CCD image and the reconstruction of the grating object is shown in Figure 4.7. The CCD camera has 1280×960 pixels, and the image shown in Figure 4.7 a) is a truncated version of the original raw image. The grating lines can be clearly seen in the CCD image and the intensities are summed vertically to generate the intensity projection shown in Figure 4.7 b).

We can observe the number of grating lines in the CCD image (Figure 4.7 a)) and the vertical intensity summation (Figure 4.7 b)) equals the number of grating lines in the signal reconstruction in Figure 4.7 c). In addition, we can see that the general amplitude profile in the CCD image qualitatively agrees with the amplitude of the reconstructed signal. From the comparison between

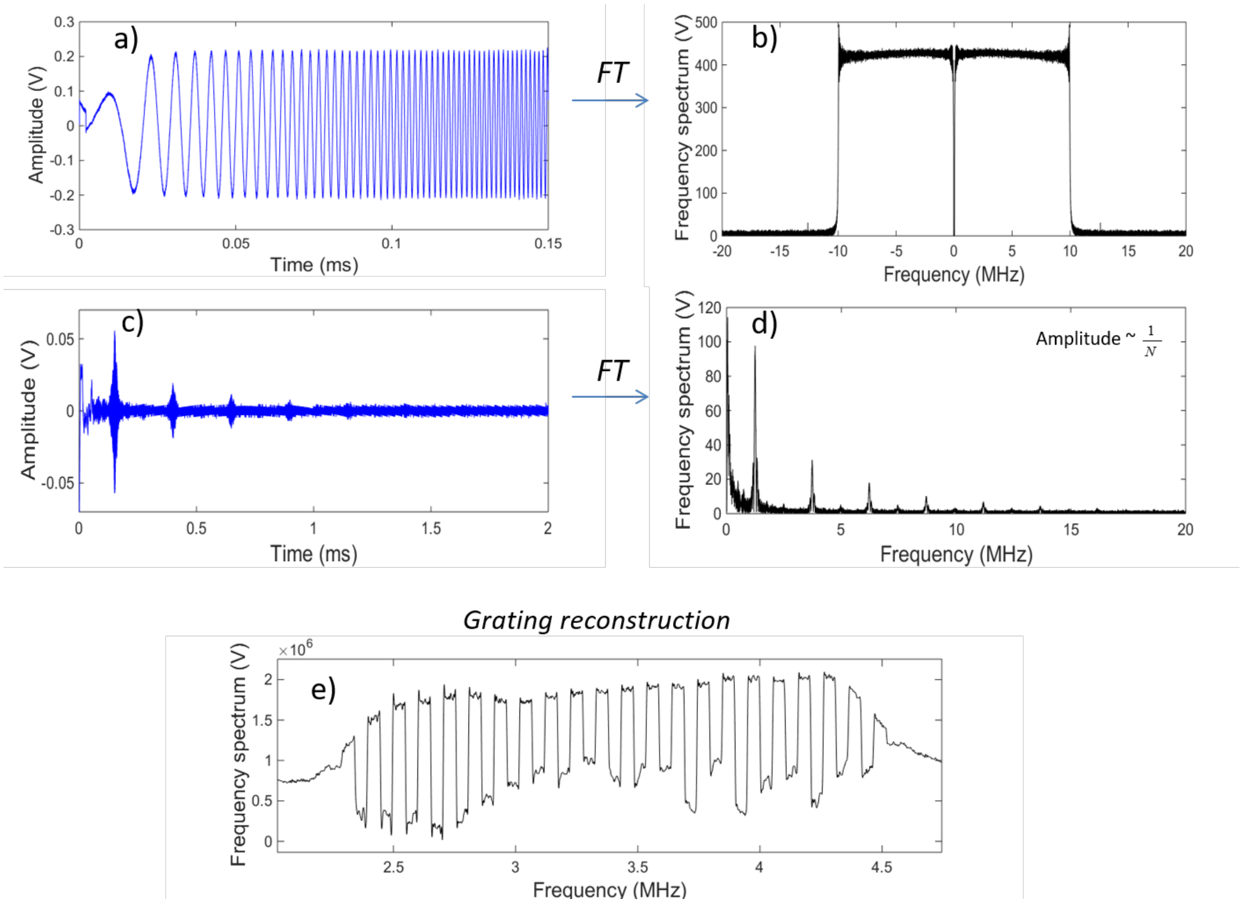

Figure 4.6: Signal reconstruction using the matched-filter algorithm.

the CCD image of the object and the reconstruction, we can safely conclude that the grating signal reconstruction matched the grating object well, and the matched filter signal reconstruction algorithm is successful.

4.4 Experiment: Polarization-interferometric structured illumination microscopy

In this section, I will describe the first experiment on polarization-interferometric SIM using a birefringent and optically active AOD. In Figure 4.4, an example of isotropic AOD crystal was described in momentum space. For isotropic diffraction, incident and diffractive optical waves make

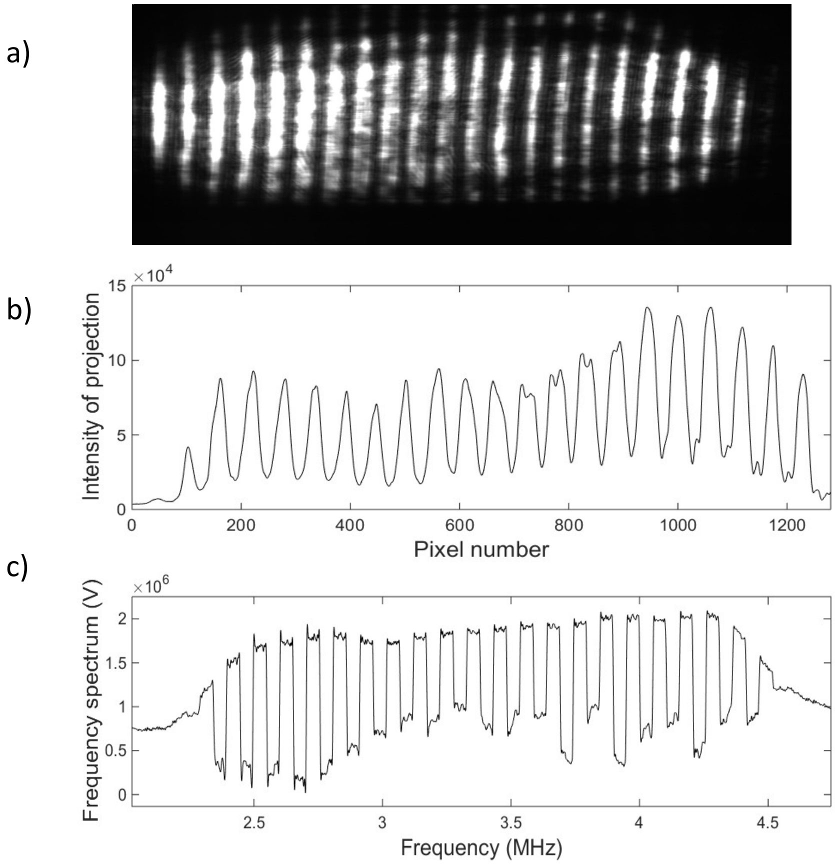

Figure 4.7: Comparison between the reconstructed signal using the matched filter algorithm and the CCD image of the grating object.

the same angle with respective to the acoustic wave ($\sin\theta_B = \lambda/2\Lambda_a$). Hence, the phase-matching condition is critical for the angle of the incident optical wave. Optically active positive uniaxial crystals only account for about 5% of natural crystals. If an external electric field is applied to an optically active crystal, it not only produces polarization but also induces a magnetic field as a result of the helical motion of the electrons. Optical activity splits the n_e and n_o surfaces, however the introduced birefringence is usually very small. Therefore the birefringence effect due to the optical activity can be considered when the optical wave is propagating close to the optical axis of the crystal. For positive uniaxial crystals with optical activity, the index surfaces are given by

[119],

$$\frac{n_1^2(\theta)cos^2(\theta)}{n_o^2(1+\sigma)^2}+\frac{n_1^2(\theta)sin^2(\theta)}{n_o^2} \tag{4.7}$$

$$\frac{n_2^2(\theta)cos^2(\theta)}{n_o^2(1+\sigma)^2}+\frac{n_2^2(\theta)sin^2(\theta)}{n_e^2} \tag{4.8}$$

The Bragg matching condition for the birefringent crystal [119] also depends on the extraordinary and ordinary refractive indices given by

$$\sin\theta_i=\frac{\lambda_0}{2n_i\left(\theta_1\right)v_a\left(\theta_a\right)}\left(f_a+\frac{v_a^2\left(\theta_a\right)}{\lambda_a^2 f_a}\left(n_i^2(\theta_1)-n_d^2(\theta_2)\right)\right) \tag{4.9}$$

$$\sin\theta_d=\frac{\lambda_0}{2n_d\left(\theta_2\right)v_a\left(\theta_a\right)}\left(f_a-\frac{v_a^2\left(\theta_a\right)}{\lambda_a^2 f_a}\left(n_i^2(\theta_1)-n_d^2(\theta_2)\right)\right) \tag{4.10}$$

where θ_i and θ_d are the angle of incident and diffraction, respectively. θ_1 and θ_2 are angles between the incident and diffracted light with respect to the optical axis for the unrotated crystal (in the [001] direction). λ_0 is the wavelength of incident light, f_a is the acoustic frequency, and v_a is the acoustic velocity in the crystal. Additionally, the direction of acoustic propagation is represented by θ_a. The angle are illustrated in k-space as seen in Figure 4.8 a). However, note that the elliptical eigen polarizations only remain for about a few degrees away from the optical axis [120]. Note that optical activity is indicated by the split between the two index surfaces of n_e and n_o. (As an exmaple, if $n_i = 2.27$, $n_d = 2.26$, $v_a = 600m/s$, then $\theta_i = 1.4$ and $\theta_d = 1.3$).

Because TeO$_2$ is an optically active positive uniaxial crystal, tangential birefringent diffraction becomes possible, hence there exists a wide range of acoustic frequencies that satisfy the phase-matching condition. The tangential matching case is shown in Figure 4.8 b). This increased acousto-optic interaction region improves the bandwidth for acousto-optic devices, which should be taken into design consideration. If the incoming light makes an angle with the optical axis of the crystal, the state of polarization will be split to orthogonal polarizations defined by the eigen-polarization states on the n_e and n_o index surfaces. Hence, polarization switching happens between incident and diffracted optical waves satisfying the Bragg matching condition in Eqn. 4.9. Because the polarization of the diffracted wave is different from the incident wave, if the 0^{th} and 1^{st} order beams are made to interfere, the modulation depth of the interference pattern will not be optimized. However, by interfering 0^{th} and 1^{st} order beams from the crystal, we can obtain higher spatial frequency fringes that lead to better spatial resolution for optical imaging. Another important aspect is that the diffraction efficiency can be improved by operating the birefringent crystal at an angle that gives the optimum state of polarization. Hence to generate polarization interferometric DSIM using the 0^{th} and 1^{st} order beams, it is necessary to consider the input and output state of polarizations in this polarization-switching geometry.

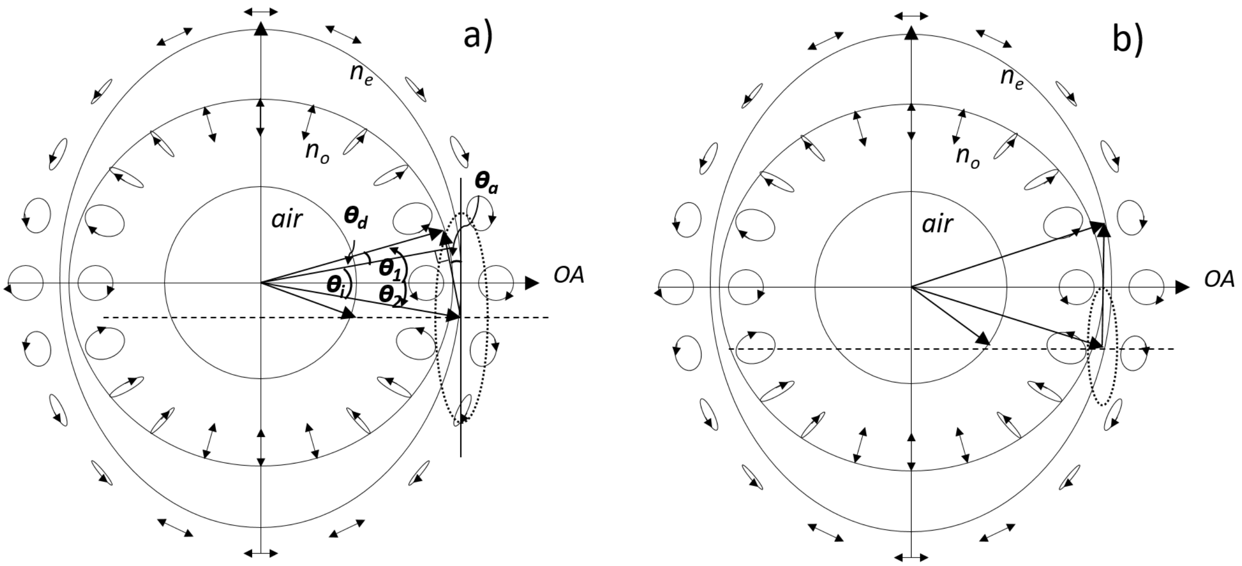

Figure 4.8: Momentum space representation of a uniaxial optically active TeO_2 crystal with state of polarizations maps for n_e and n_o index surfaces. a) non-tangential matching condition b) tangential matching condition.

The polarization inteferometric experiment setup is shown in Figure 4.9. The emerging laser beam from the HeNe laser (10 mW avaerage power) is focused by a 50.8 mm focal lens to the center of the crystal of an AOM. The AOM is driven by two amplified RF signals from LO2 and LO3, respectively, and the diffraction efficiency of the AOM measured with an optical power meter is 46%. The RF signals are a 164 MHz and a 225 MHz sinusoidal signal, which gives a beat frequency of 61 MHz when the two diffracted 1^{st} order beams are overlapped. The 0^{th} order beam from the AOM is blocked while the two 1^{st} order beams are sent to the AOD by two folding mirrors and a collimation lens because the AOD requires plane wave illumination to deflect input beams. The total power in the 1^{st} order beams from the AOM is about 3 mW. The AOD which has a positive uniaxial and optically active TeO_2 crystal inside is driven by an amplified 61 MHz RF signal generated from LO1. When the Bragg matching condition is satisfied, the 0^{th} and 1^{st} order diffracted beams from the AOD are imaged onto the surface of a Ronchi ruling target (Edmund Optics, 500 lines/inch) using an $M = 10$ magnification 4F imaging system. Note that the Ronchi ruling needs to be positioned at the image plane of the illumination patterns, which is generated at the center of the AOD. This image plane is found by using the trick of the diffusing scotch tape alignment method taught in the Advanced optics lab. In this strobing mode experiment, the Moiré patterns become visible in a dark room due to the multiplication between the illumination pattern and the Ronchi ruling.

The high speed photodiode detector sends the integrated intensity SIM signal to a digital oscilloscope. From the setup shown in Figure 4.9 a), we then switch from the strobe mode to SIM mode because the Moiré patterns are confirmed as a successful step. Hence, the three LOs are replaced with a direct digital synthesizer (DDS). The AOM now simply passes the laser beam through without diffraction. The system is realigned to the laser beam to be Bragg-matched in the AOD, which is driven by a phase-coherent chirp similar to the RF setup section shown in Figure 4.5. The 0^{th} and 1^{st} order diffracted beams from the AOD are imaged onto the target using the same 4F imaging system described before. Then a polarizer is inserted between the object and the 4F imaging system, and its orientation is selected for maximum SIM signal amplitude, which is monitored by the osc-scope. As shown in Figure 4.9 b), the maximum peak-to-peak amplitude of the SIM signal is 40 mV with a low frequency background, which is the Fourier transform of the Ronchi ruling aperture illuminated by the laser beams. Then the polarizer is removed from the system, and the peak-to-peak amplitude of the SIM signal is increased to 150 mV.

The result suggests that the polarization interferometric SIM signal has a lower amplitude as a sacrifice for polarized illumination. However, several insights can be learned from the results

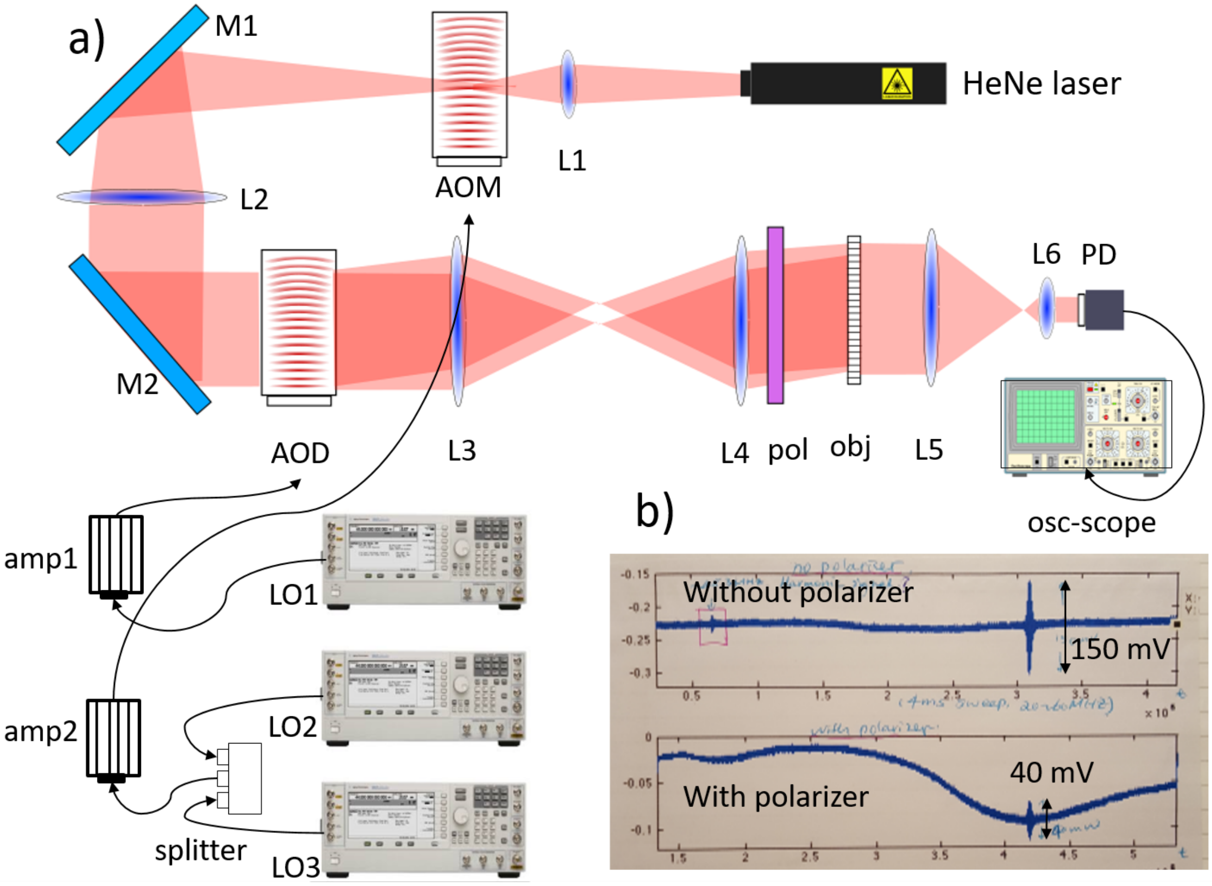

Figure 4.9: Polarization interferometric SIM experiment setup by interfering 0^{th} and 1^{st} order diffracted beams from the AOD. a) is experiment setup and b) are SIM signals obtained from osc-scope with and without polarizer in the setup. LO1-3: RF function generators/local oscillators, AOM: acousto-optic modulator, AOD: acousto-optic deflector, amp: RF amplifier, obj: Ronchi ruling grating object, PD: high speed photodiode detector, osc-scope: digital oscilloscope, pol: polarizer.

obtain in the first polarization interferometric SIM experiment. Because our HeNe laser is assumed to be linearly polarized, it will be projected and decomposed to the eigen-polarizations of the n_e and n_o index surfaces determined by the Bragg angle. Because the 1^{st} order beam diffracted from the AOD diffracts up following the phase-matching condition, the polarization will switch to approximately another elliptical state, which can be significantly different from the 0^{th} order beam. Hence upon interference, the modulation contrast of the illumination pattern may be reduced due to the difference between the state of polarizations. Therefore for future improvements, the polarizations of the 0^{th} and the 1^{st} order diffracted beams from the TeO_2 crystal can be optimized systematically to enhance photon budget of the system. Another method is to use a wollaston prism with a differential detection scheme that detects the extraordinary and ordinary polarization components separately to maximize the photon budget.

The significance of polarization interferometric SIM is its potential for creating dynamic, fast, and switchable polarized illumination based on AOD diffractions to perform polarization-sensitive imaging in a scattering medium. The process can be electronically controlled instead of using mechanically moving system components such as a MEMs device. Compared to a spatial light modulator which is also capable of generating dynamic illumination fringes, AOD is faster (MHz rather than KHz) and more cost effective. For unknown objects embedded in a scattering medium, it is possible to simultaneously combine polarization interferometric imaging with the concept of Fourier domain imaging to obtain high resolution images of the object using the 0^{th} and the 1^{st} order diffracted beams from the AOD. Using a high power laser instead of the HeNe laser opens new paths to unexplored territories in optical imaging using polarization inteferometric SIM. On the other hand, instead of using a narrow-band HeNe laser, a polarization-sensitive and spatially coherent broadband light source can be applied in the polarization interferometric SIM system to enable coherence gating and possible adaptive tunable polarization interferometric imaging. Therefore, the feasibility results in this experiment motivates the investigation of high power, polarization-controlled and ultra-broadband light source.

In summary, a dynamics structured illumination microscope (DSIM) is designed and constructed for Fourier domain imaging using moving illumination patterns generated from an acousto-optic defelctor (AOD). The microscope using AOD for moving illumination pattern generation using a frequency sweep from the direct digital synthesizer (DDS) with photodiode detection is demonstrated. The DDS is configured to generate a phase-coherent chirp signal for the experiment. To reconstruct the object from the DDS chirp and the photodiode detector signal, a matched-filter algorithm is developed, and the reconstructed signal agrees well with the image of the object recorded by a CCD camera. Polarization interferometric DSIM was explored using the polarization switching feature due to the optically active birefringent TeO_2 crystal. Insights were gained from the experiment that the polarizations of the diffracted beams can be optimized to enhance diffraction efficient hence the photon budget of the optical system. The advantage of the polarization interferometric DSIM is its potential in creating rapid, dynamic, and switchable polarized active illumination to perform polarization-sensitive imaging in a scattering medium. The process can be electronically controlled without mechanical moving parts. Compared with conventional SIM techniques, DSIM based on DEEP uses moving illumination patterns generated through a uniaxial crystal in the AOD and only requires a single-pixel camera or photodiode detector for Fourier domain imaging. The advantage of using AOD to generate dynamic illumination patterns is the fast speed (MHz/ms) compared to spatial light modulator (on the order of 10 kHz). Although the power efficiency of AOD can be improved with better design, AOD is more cost-effective than SLM for Fourier domain imaging requiring only a single-pixel detector.

4.5 Broadband light source for optical imaging in scattering medium

The previous experiments describe a dynamic structured illumination microscope for optical imaging using Fourier synthesis and interferometric illumination patterns generated by an acousto-optic deflector. As discussed in Chapter 2 and 3, multiple scattering degrades the optical image quality and limits the penetration depth of light propagation. Using broadband illumination with DEEP was proposed recently as a type of coherence gating to enhance the ballistic photons and increases penetration depth for optical imaging in scattering medium [116].

The coherence gating proposed uses the fact that the optical path length induced by scattered light which is longer than the temporal coherence length of the illumination is suppressed while the ballistic light is enhanced. Note for DEEP, the coherence-gated interference happens at the object rather than at the detector. The conventional approach for simulating the light propagation in scattering medium is Monte Carlo method mentioned in Chapter 2 for solving the radiative transfer equation, however, the coherence and interference effects cannot be included in this intensity based diffusion model. Although finite-difference time-domain (FDTD) method is employed by many researchers to numerically solve Maxwell's equations, it is not appropriate for large scale imaging problems because of its computational inefficiency. Split-step Fourier beam propagation method was selected to model DEEP in scattering medium because is it much faster and efficient in solving forward propagating fields [78, 116].

The algorithm was developed and described in details in [78]. However, in the following section I will review the main steps used in the algorithm in order to provide a clearer theoretical explanation for the simulation results that follows. Basically, the method involves using the scalar Helmholtz wave equation for a coherent wave propagating in the scattering medium. In a 2-D cross section the Helmfoltz equation in an inhomogeneous region is [78],

$$\frac{\partial^2 \mathbf{E}(y,z)}{\partial z^2} + \frac{\partial^2 \mathbf{E}(y,z)}{\partial y^2} + k^2 n^2(y,z)\mathbf{E}(y,z) = 0 \tag{4.11}$$

where $k = \frac{2\pi}{\lambda}$ is the wave number in free space, $\mathbf{E}(y,z)$ is the electric field in phasor format which can be defined as,

$$\mathbf{E}(y,z,t) = \mathbf{A}(y,z)e^{ikn_m z}e^{i\omega t} \tag{4.12}$$

where $\mathbf{A}$ is the slowly varying field to be solved for, $n(y,z)$ is an inhomogeneous refractive index distribution which can be express as,

$$n(y,z) = n_m + \delta n(y,z) \tag{4.13}$$

where n_m is the mean refractive index and $\delta n(y,z)$ is the small refractive index perturbation due to the scattering inhomogeneity. The scattering medium is represented as a mean refractive index distribution with a perturbation characterized by a small standard deviation. The slowly varying envelope approximation yields,

$$i2kn_m \frac{\partial \mathbf{A}(y,z)}{\partial z} + \frac{\partial^2 \mathbf{A}(y,z)}{\partial y^2} + k^2(n^2(y,z) - n_m^2)\mathbf{A}(y,z) = 0 \tag{4.14}$$

For small perturbation in the refractive index, $n^2(y,z) - n_m^2 \approx 2n_m\delta n(y,z)$, then substitute the approximation into Eqn 4.14 we obtain the inhomogeneous evolution equation,

$$\frac{\partial \mathbf{A}(y,z)}{\partial z} = -j(2kn_m)^{-1}\frac{\partial^2 \mathbf{A}(y,z)}{\partial y^2} - ik\delta n(y,z)\mathbf{A}(y,z) \tag{4.15}$$

$$= \mathscr{L}\left\{\mathbf{A}(y,z)\right\} + \mathscr{N}\left\{\mathbf{A}(y,z)\right\} \tag{4.16}$$

where $\mathscr{L}$ denotes a linear operator for electric field propagation in a homogeneous medium, and $\mathscr{N}$ denotes an operator describing the index perturbation. This first order evolution equation can be integrated over a small step Δz,

$$\mathbf{A}(y,z+\Delta z) = e^{(\mathscr{L}+\mathscr{N})\Delta z}\mathbf{A}(y,z) \approx e^{\mathscr{N}\Delta z}e^{\mathscr{L}\Delta z}\mathbf{A}(y,z) \tag{4.17}$$

Since the linear diffraction step is easier computed in the Fourier space we can rewrite $\mathbf{A}(y,z+\Delta z)$ as the following,

$$\mathbf{A}(y,z+\Delta z) = e^{-ik\delta n(y,z)\Delta z}\mathscr{F}^{-1}\left\{\mathscr{H}(k_y;\Delta z)\mathscr{F}\left\{\mathbf{A}(y,z)\right\}\right\} \tag{4.18}$$

where δn is given in Eqn 4.13, and $\mathscr{H}(k_y;z)$ is the transfer function of the homogeneous medium for propagation over a distance Δz, which can be expressed as [121],

$$\mathscr{H}(k_y;z) = e^{-i\Delta z\sqrt{k^2n_m^2-k_y^2}} \tag{4.19}$$

This simulation included a time variation due to the slowly propagating signal in the AOD, which was simulated as a stepped RF frequency producing a pair of Doppler shifted plane waves interfering at the top of the sample, and then stepping through average of frequencies. These then propagated through the scattering to various depths where the light was modulated by an amplitude grating. This modulated light was detected at each depth and each RF frequency to produce the DEEP signals whose Fourier transforms are indicated at each depth. The single peak in the center encoding the grating spatial modulations are seen to be eliminated by scattering as the depth increases. Then the simulation were repeated with polychromatic sources simulated by incoherently summing the separately beam propagated results at each wavelength across the band. As the fractional bandwidth increased, the desired peak measuring the spatial grating is seen to persist to deeper depth, thereby improving the ability to image into scattering medium.

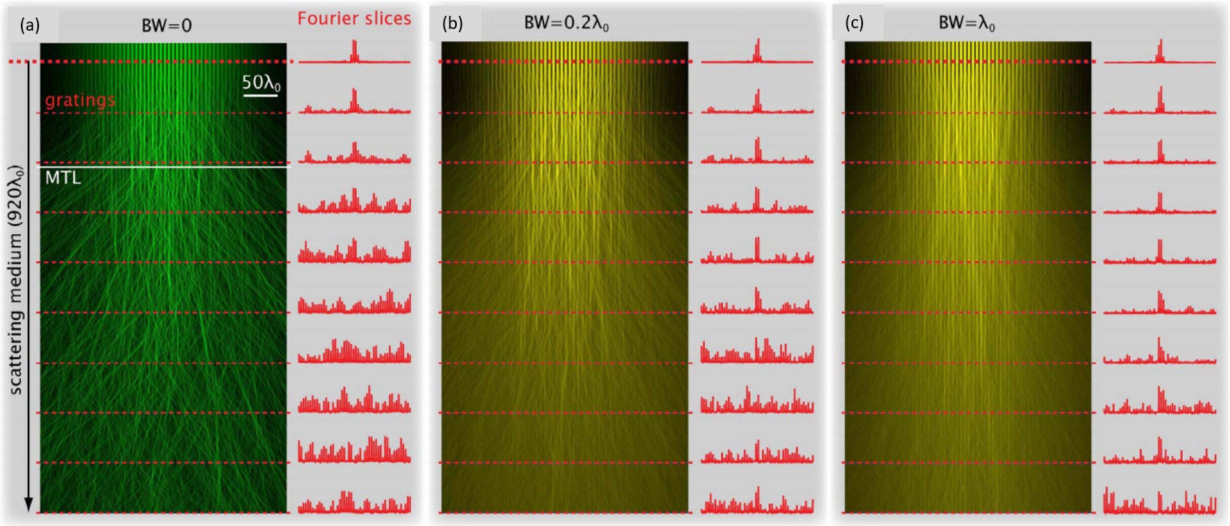

Figure 4.10: Fourier split-step simulation of interference patterns in a highly scattering medium for coherence gating effects. (a) monochromatic light source, (b) broadband light source with 0.2λ fractional bandwidth, and (c) broadband light source with λ bandwidth. Adapted from Dr. Daniel Feldkhun's thesis [78]

The model assumes an average scattering cosine angle of $g = 0.87$, hence the medium is mostly forward scattering. The mean refractive index is assumed to be $n_m = 1.33$ with a small perturbation represented by a standard deviation of 0.017 and a mean transport length of $200\lambda_0$. The numerical simulation results using Fourier split-step method are displayed in Figure 4.10. The broadband interference patterns are generated by summing the monochromatic interference patterns at a number of wavelengths within the designed bandwidth incoherently. There is a grating structure with a period of $6\lambda_0$ placed at 10 different depths indicated by the dashed red lines in the figures. The detector signal is generated by spatially integrating the product between the interference pattern at the grating and the grating structure. Note the process is repeated for 50 spatial periods of the interference pattern from $4\lambda_0$ to $12\lambda_0$ to simulate chirp signals generated from the Bragg grating. The detector signal is then Fourier transformed to obtain a Fourier slice at each different depth shown in the figures. For this highly scattering medium, we see substantial improvement in penetration depth using the coherence gating technique because the detectable grating structure signal is 3 or 4 times better using the broadband illumination in Figure 4.10 (c).

From the published results in Figure 4.10, I'm motivated to investigate a broadband light source for coherence gating that can be a light source for the dynamic structured illumination technique discussed in this chapter to increase penetration depth in a scattering medium. The investigation of a supercontinuum broadband light source using a photonic crystal fiber and a high repetition rate ultrafast Ti:Sapphire laser will be discussed in details in Chapter 5

Chapter 5

Polarization-controlled supercontinuum generation in birefringent photonic crystal fiber

5.1 Supercontinuum generation in optical fiber

Traditionally, nonlinear fiber optics and biophotonics have been two unrelated areas. However, in recent years, the fiber-based supercontinuum light source has emerged as a versatile and potentially portable optical source that can provide spatial coherence, broad bandwidth, and wavelength for biophotonic imaging applications [122], including optical sensing [123], diffuse optical tomography [124], confocal microscopy [125], optical tweezers [126], fluorescence spectroscopy [127], optical coherence tomography [128] and flow cytometry [129]. Compared to thermally based broadband light sources, supercontinuum laser sources using PCF are spatially coherent and partially temporally coherent. Supercontinuum laser sources can cover a wide spectrum range from UV, to visible, to infared, which is the ideal light source for many scientific applications. It has the bandwidth of sunlight but is at least 10^4 brighter [122]. Furthermore, soliton self-frequency shift (SSFS) generated in the supercontinuum process has recently been demonstrated to enhance the signals in fluorescent imaging and enable deeper penetration in brain imaging as a novel tunable light source.

Supercontinuum generation in microstructured PCF has been investigated extensively since the late 1990s [21, 23, 130]. The unique dispersion engineering capability and high effective nonlinearity have made the PCF an excellent medium for broad supercontinuum generation[131, 132]. Dispersion engineering can be achieved by changing the periodic structure of the PCF cladding to vary the group velocity dispersion (GVD). Because the microstructured PCFs typically have extremely small core diameters, the effective nonlinear coefficient of PCF is usually many times higher than standard fibers. In this chapter, I will review nonlinear effects in supercontinuum generation and polarization evolution in birefringent fibers. Then supercontinuum light source generated in a birefringent PCF will be discussed and experimental results will be presented for different input state of polarizations. Furthermore, an optical delay line experiment is designed and demonstrated using off-the-shelf broadband dielectric mirrors to rotate the polarization without special achromatic wave plates to double the repetition rate for applications requiring high bandwidth, high repetitation and polarized light as illumination source.

5.1.1 Nonlinear effects in supercontinuum generation

Nonlinear effects arise in supercontinuum generation due to intense light-matter interactions, which then leads to spectral broadening of the original input light. Typically, the nonlinear effects include self-phase modultion (SPM), four wave mixing (FWM), cross-phase modulation (XPM), stimulated Raman scattering (SRS), and optical shock [130, 132, 133]. The excited nonlinear effects interplay with dispersion and diffraction during light propagation inside the supercontinuum medium, and the output spectrum can be extremely complicated. Numerical simulation was performed using the symmetric split-step Fourier method to solve the coupled-nonlinear wave propagation for supercontinuum generation in a PCF. The results are presented in Figure 5.1.

While the details of the simulation model will be described in the next chapter, from this simulation, we see when an optical pulse is launched into a piece of PCF, the spectrum of the pulse is symmetrically broadened due to SPM as the pulse is compressed during the initial propagation in the PCF shown in the temporal evolution plot. However, as the pulse is compressed, the intensity becomes even higher to the extent that additional nonlinear effects in the PCF become evident, such as optical shock, XPM, and Raman self-frequency shift. In the short wavelength regime, dispersive wave generation is responsible for spectrum broadening while Raman-induced self-frequency shift is responsible for the spectrum shifting into the longer wavelength regime. The wave ejected during

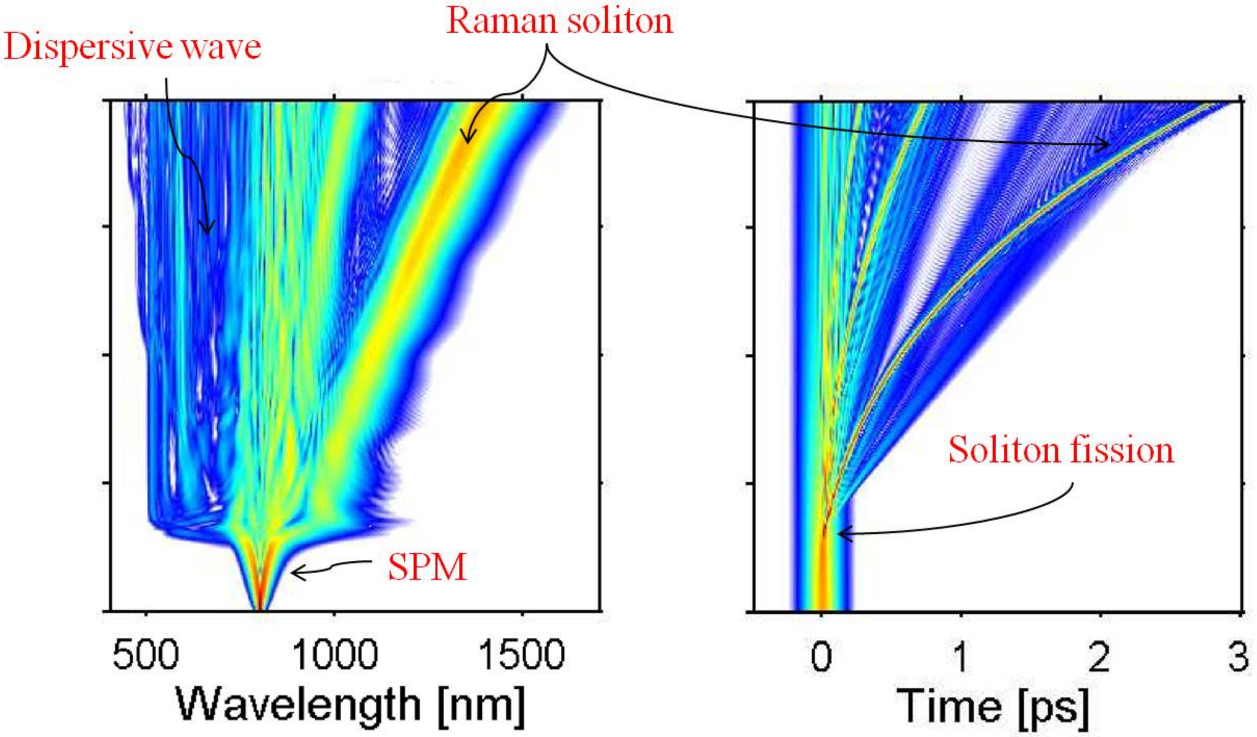

Figure 5.1: Numerical simulation of supercontinuum generation for spectral and temporal evolution as a function of propagation distance in a photonic crystal fiber.

the complex fusion process sheds excessive energies and eventually evolved into a fundamental soliton. Then the soliton begins to frequency down-shift due to the Raman effect, so it is termed a Raman soliton. Higher order Raman solitons can be seen in the temporal domain evolution as the optical wave is further propagated in the PCF. The Raman soliton part of the supercontinuum generation is particularly interesting because it not only can carry more than 70% of the total energy, but also its polarization is uniform across the soliton pulse, which can be useful for imaging and sensing applications requiring a tunable light source with uniform polarization. Note that the numerical simulation was performed using vectorized generalized nonlinear Schrödinger equations. The result plotted in the temporal field evolution is the linear sum of the x and y polarization components.

5.2 Polarization evolution in birefringent fibers

Polarization effects in supercontinuum generation were largely ignored until 2005 when the polarization dependence of supercontinuum in a tapered birefringent PCF was investigated [134]. Supercontinuum light source generated in a nonlinear birefringent fiber medium is one of the most fascinating applications for both light interaction with nonlinear birefringent material and nonlinear optics. In the previous section, we saw the numerical simulation of supercontinuum generated in a PCF. Although the numerical results of the the temporal and spectral evolution along the PCF are plotted in the total intensity domain, the numerical model was constructed using coupled nonlinear Schrödinger equations, which considers the coupling of the two polarization eigenmodes for the PCF. Hence, in this section, polarization evolution in birefringent fibers and birefringence will be discussed in the context of light propagation in anisotropic crystals.

During light propagation in the anisotropic crystals, interesting phenomena arise, including optical rotation, polarization, acousto-optics, electro-optics, and birefringence phenomenon. (Birefringence refers to the double refraction of light when interacting with anisotropic crystals, which has orientation-dependent differences in the refractive index due to its non-symmetric crystalline lattice structure.) Examples of anisotropic crystals include calcite, quartz, KDP and liquid crystals. Light interactions with birefringent material been applied in a wide range of exciting areas in optics. Stokes parameters can be used to describe polarization of light fields in a birefringent medium. The stokes vector $[S_0, S_1, S_2, S_3]$ gives the complete information of the intensity and the state of polarization (DoP) of the plane wave [135]. For a monochromatic wave, the Stokes vector should satisfy the relationship of $S_0^2 = S_1^2 + S_2^2 + S_3^2$. The theory of Stokes vectors has been well presented in the literature. Stokes vectors can be measured experimentally and represented on the Poincaré sphere.

The Poincaré sphere is a useful geometrical representation of state of polarizations in the polar coordinate, where the axes are represented by $\sigma_1 = S_1/S_0, \sigma_2 = S_2/S_0$, and $\sigma_3 = S_3/S_0$. Each point on the sphere represents a unique state of polarization $[S_1, S_2, S_3]$. For polarization evolution

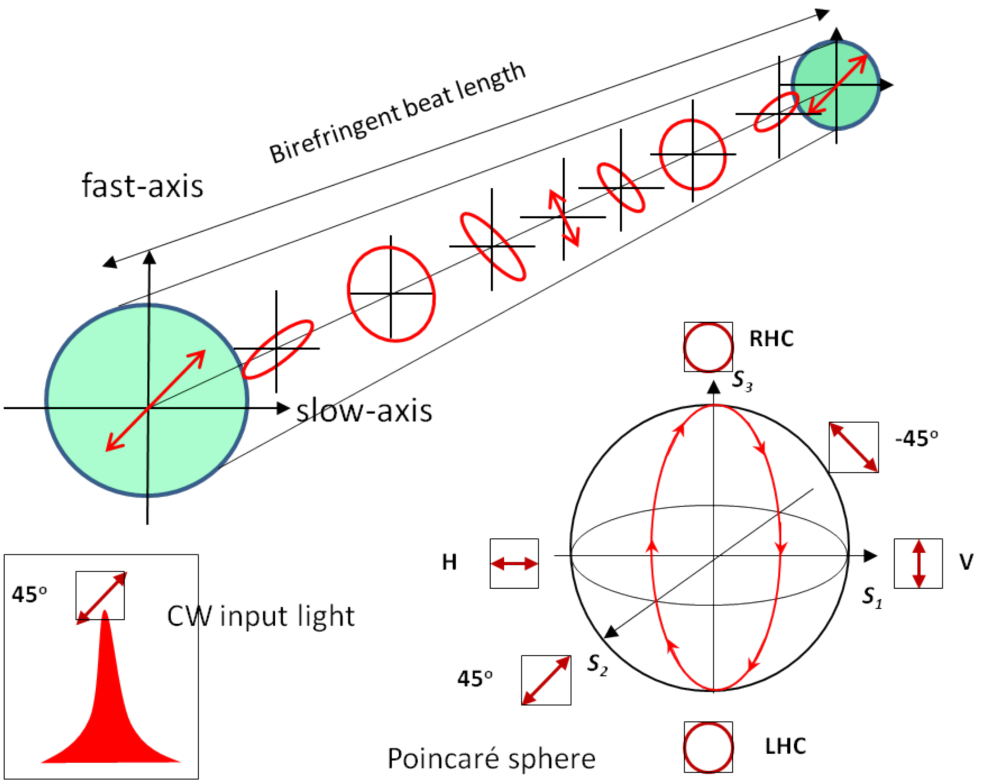

Figure 5.2: Polarization evolution in polarization maintaining fiber showing the eigen-axis and birefringence beat length and the Poincaré sphere representation for linear polarization rotation with CW input light.

in birefringent fiber, the Stokes parameter can be visualized on the Poincaré sphere, which is shown on the right of Figure 5.2. For linearly birefringent fiber, the polarization trajectories rotate on the Poincaré sphere around the S1 eigen-axis while for circularly birefringent fiber, the trajectories rotate around the S3 axis. (The numerical study of polarization dynamics of supercontinuum generation using Poincaré sphere representation will be discussed in detail in the next chapter. In the following section, I will describe the supercontinuum generation experiment that provides the motivations to the investigation of the numerical simulations.)

Birefringent crystals can be either uniaxial or biaxial depending on the crystal structure. Examples of commonly used uniaxial crystals include calcite, lithium niobate, and quartz. For these types of crystals, the birefringence is intrinsic. Some long-chain polymers and biological tissue fibers also have intrinsic birefringence. For naturally non-birefringent (i.e., isotropic) materials, birefringence can be externally induced by applying stress, strain, bending or force to lose isotropy in one particular dimension. One good example is plastics under mechanical stress, such as scotch tape that acts as a half-wave plate at 632 nm. Note that stress-induced birefringence can be as high as 10^{-4}. Another type is form birefringence where a structure is artificially created in a carrier medium with a different refractive index, one example is PCF, and another interesting example is metamaterial when the lattice spacing is much smaller than a wavelength. Through this structural design modification of an isotropic material, a large amount of form birefringence can be achieved so the undesired small and random fluctuations of birefringence is suppressed.

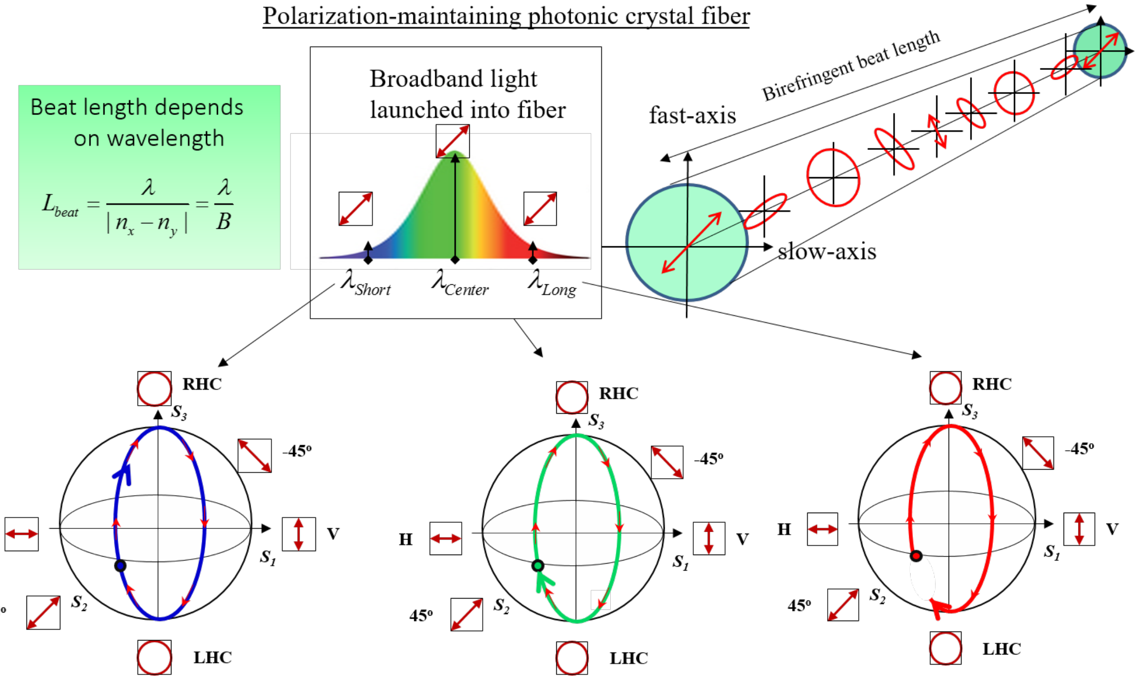

Figure 5.3: Polarization evolution in polarization-maintaining fiber showing the eigen-axis and birefringence beat length and the Poincaré sphere representation for linear polarization rotation with broadband input light.

In fact, even a single mode fiber can support two orthogonally polarization modes [133]. Because all fiber has some intrinsic birefringence due to stress, strain, or environmental perturbations, polarization-maintaining fibers were designed to suppress small unwanted variations of birefringence. Polarization-maintaining fiber follows the same principle for light to transmit through without change of polarization given the input polarization is aligned to either the slow or fast axis of the fiber. However, as shown in Figure 5.2, if the input polarization makes angle with the eigen-axis of the fiber, the state of polarization changes continuously during propagation with a period equal to the beat length $L_{beat} = \frac{2\pi}{|\beta_x - \beta_y|} = \frac{\lambda}{B}$, where B represents fiber birefringence, $B = |n_x - n_y|$, and n_x and n_y are the refractive indices for the two orthogonal polarization eigen axes respectively. Slow axis has a larger refractive index (group velocity is smaller) while fast axis has a smaller one (group velocity is larger). After integer numbers of beat length, the original input polarization is recovered. The Poincaré sphere shown in Figure 5.2 corresponds to integer number of cycle of polarization rotations around the horizontal and vertical eigen-axis. For broadband input light to the polarization-maintaining fiber, because the polarization beat length L_{beat} depends on the wavelength, as shown in Figure. 5.3, for the same 45^o input polarized light, the polarization trajectory rotates slower for the long wavelength wave than the short wavelength wave. Hence, for supercontinuum generation with an input light of a certain bandwidth, the polarization evolves differently across the spectrum which should be taken into account when analyzing the polarization dynamics of the supercontinuum process.

Nonlinear birefringence can also be generated by nonlinear Kerr effects during intense light propagation in the fiber. The coupling between the two polarization eigen modes are induced by XPM which was introduced in the previous section. Nonlinear polarization rotation on the Poincaré sphere will be very different from the linear one, the former rotates around the circular eigen-axis ($\pm s_3$) while as shown in Figure 5.2, the latter rotates around the linear eigen-axis ($\pm s_1$) for a low-power CW input light. The principles of linear and nonlinear birefringence of polarization rotation and their Poincaré sphere representations will be further discussed using numerical simulations of the nonlinear coupled wave equations in the next chapter.

5.3 Experiment: Polarization-controlled supercontinuum generation using high repetition rate ultrafast laser

In this experiment, I demonstrate an octave-spanning supercontinuum generated in a PCF pumped with a 2 GHz Ti:Sapphire laser and investigate the behaviors of the output spectrum as the input polarization is rotated. The schematic of the experiment is shown in Figure 5.4. The PCF used is a highly nonlinear polarization-maintaining fiber with a high linear birefringence of $B = 3 \times 10^{-4}$ which can suppress the effect of the random and undesired polarization variations along the fiber if a polarization eigen-mode is input to the fiber. The GiGaJet 30s Ti:Sapphire laser is pumped with a 5.5 W all-solid-state Verdi V8 operating at 532 nm. The laser is tuned to mode lock in clock-wise direction with a repetition rate of 2 GHz. Any residual beam in the counter-clock-wise direction is blocked from leaving the laser enclosure. The laser output pulses are compressed by a pair of ultra-fast dispersion compensation mirrors (DCM). The measured laser pulse and spectra outputs are shown in Figure 5.5. The full width half maximum (FWHM) pulse width measured by an interferometric autocorrelator is 28 fs assuming a hyperbolic secant pulse profile. The spectrum of laser output is centered around 810 nm with a FWHM of 70 nm. The typical average output power is 636 mW measured after the DCM.

The dechirped pulses are then propagated through a half-wave plate (HWP) and coupled into the PCF by an objective lens (Newport Precision Objective lens, 20X, NA: 0.35). The laser beam spatially fills the aperture of the objective lens, the spot size at the focal of the objective lens is 1.78 μm for a 5.2 mm clear aperture. The coupling to the PCF is optimized by a six-axis NanoMax alignment stage. The PCF (NL-PM-750, Crystal Fibre) has a small core diameter of 1.8 μm and a short zero dispersion wavelength at 750 nm. A coupling lens collimates the PCF output beam to monitoring devices including a power meter and an optical spectrum analyzer. The input pulse is coupled to the eigen-axis of the PCF at a particular orientation of the HWP.

Figure 5.6 shows the picture of the experiment of the supercontinuum generation through a PCF. At the output of the PCF, a symmetric intensity pattern is observed that reflects the

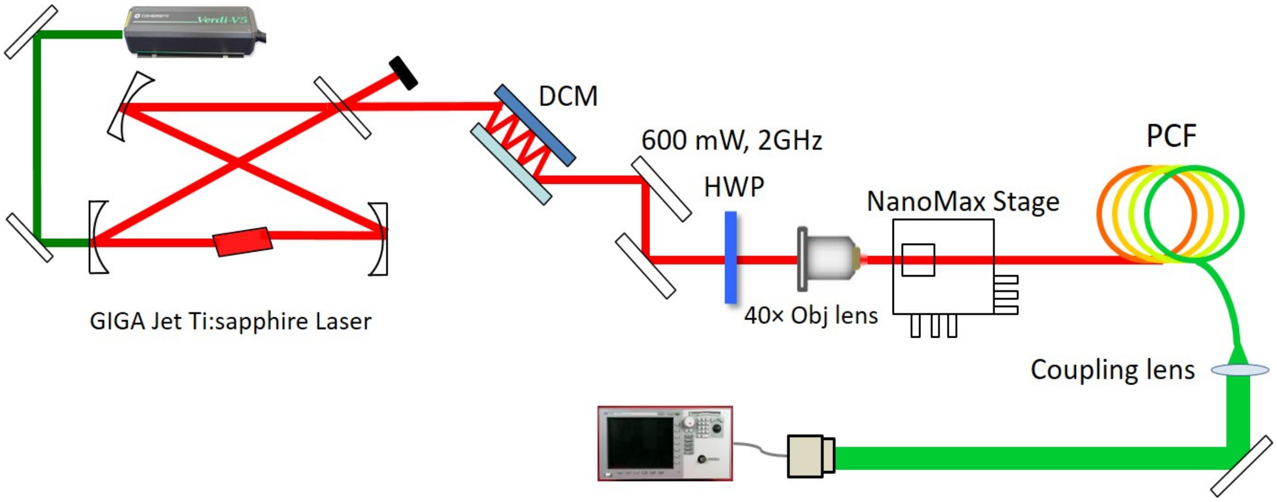

Figure 5.4: Experiment setup for supercontinuum generation in a photonic crystal fiber. DCM, dispersion compensation mirror; HWP, half-wave plate; PCF, photonic crystal fiber.

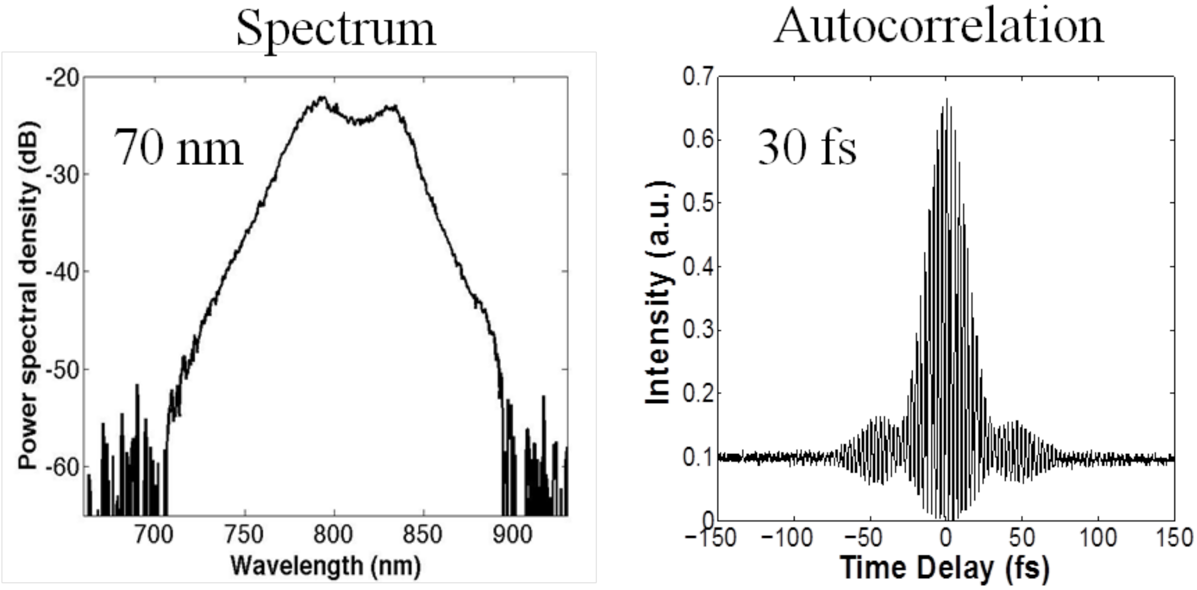

Figure 5.5: Interferometric autocorrelation trace of the dechirped pulses and spectrum of output pulses from the GiGa laser.

hexagonal shape of the PCF cross-sectional mode. We study the behavior of supercontinuum when the input polarization is rotated with respective to the eigen axis of the PCF. The eigen-axis of the PCF is identified by using a wollaston prism and a power meter at the output of the fiber. By rotating the HWP in 5^o steps and recording the power for each of the two polarization components at the output of the PCF, we found the peaks and dips of roughly sinusoidally oscillating power outputs, which corresponds to locations of the eigen axis. This became the lookup table for the readings of the HWP for aligning the input light to the eign-axis of the PCF. The HWP can be rotated from its eigen axis position by steps of 22.5^o then the output supercontinuum spectra are recorded using an optical spectrum analyzer.

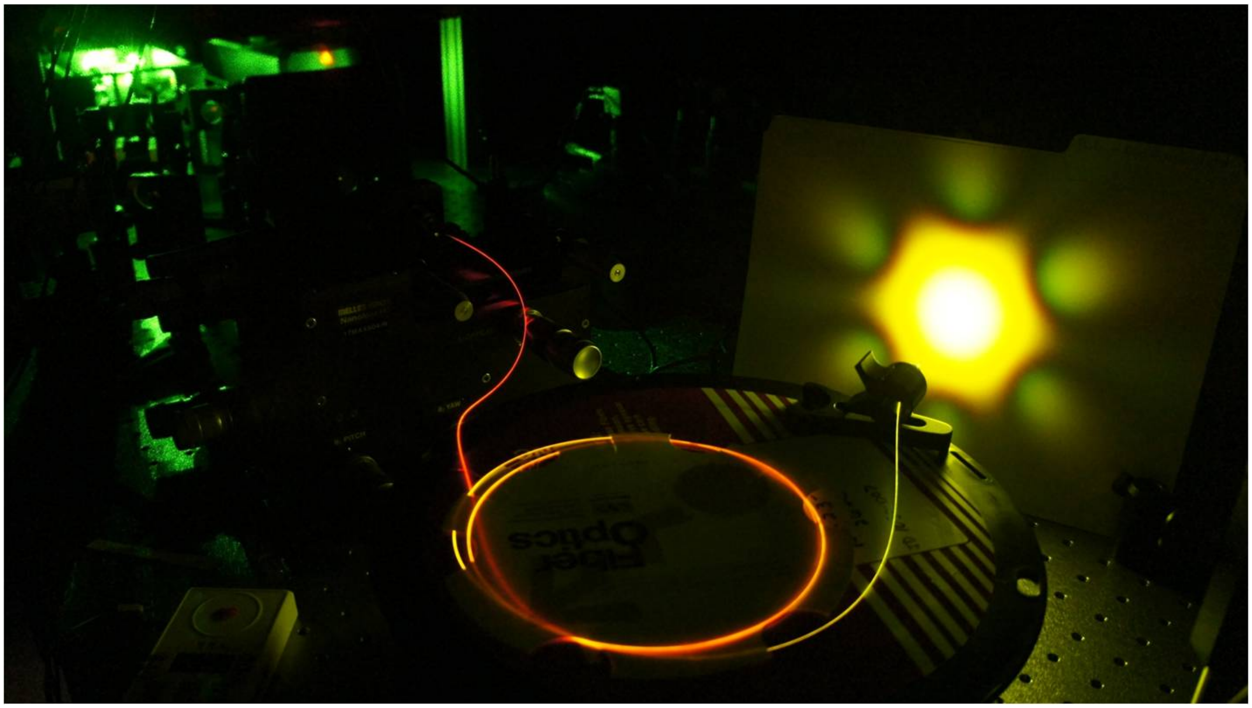

Figure 5.6: Picture of the supercontinuum generation experiment from a PCF.

The resulting supercontinuum spectra are shown in Figure 5.7 (a) to (e). By changing the input pulse polarization, different reshaped spectra with different output beam colors are observed and are shown in Figure 5.7 (f) to (j). A symmetric beam color pattern is observed for input polarizations varying from the fast to slow axis. At a 45^o HWP angle, the supercontinuum output is visibly the greenest, shown in Figure 5.7 (h). All spectra in Figure 5.7 show UV light generation from around 350 nm perhaps due to frequency tripling. However, in the long wavelength regime, we observe that the Raman soliton shift is asymmetric, showing a narrowest supercontinuum width in Figure 5.7 d) at 67.5^o HWP angle. This spectrum asymmetry of the Raman spectrum with respective to the HWP angle (input polarization) will be further explained using the polarization instability phenomenon numerical simulation in the next chapter. The experimental observations motivated us to conduct these numerical simulations. In addition, the results shown in the experiment qualitatively agree with the numerical simulations.

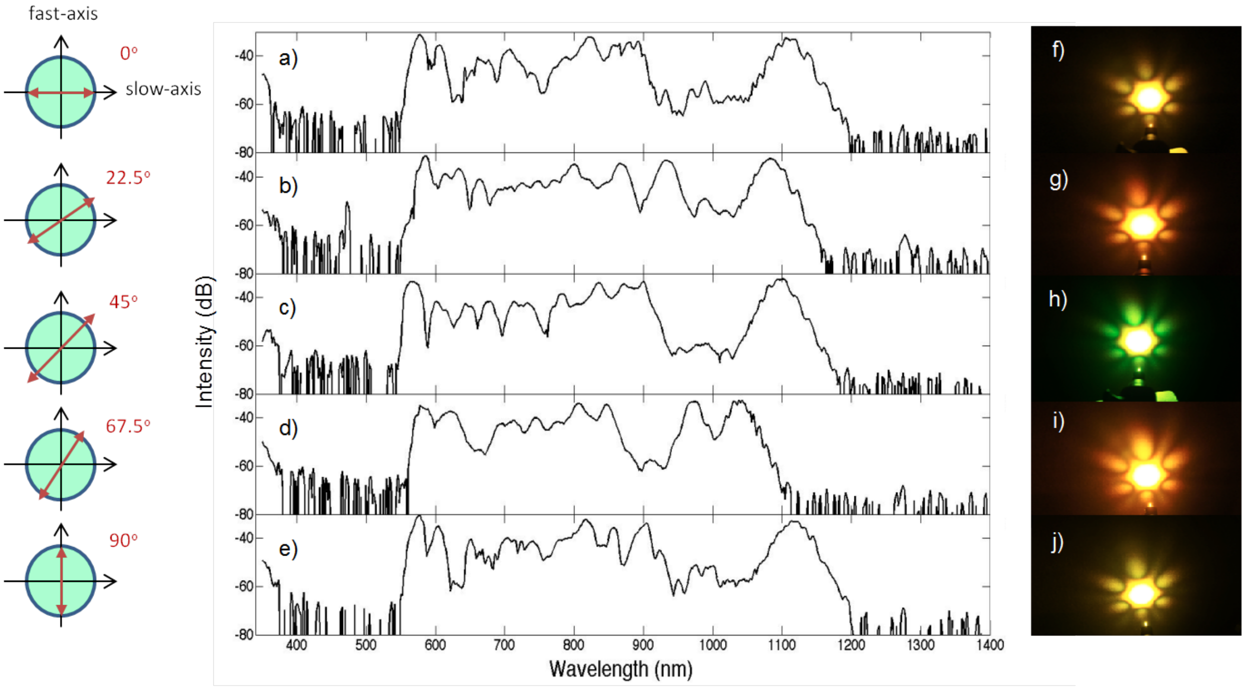

Figure 5.7: Experimental results of supercontinuum generation in a PCF. Supercontinuum spectra with HWP angle at: (a) 0^o, (b) 22.5^o, (c) 45^o, (d) 77.5^o and (e) 90^o to eigen axis of PCF; (f) to (j) show the corresponding photographs of supercontinuum output beams.

In this experiment, we demonstrated a polarization-controlled supercontinuum generation in a linearly birefringent PCF using the pulses from a dispersion-compensated 2 GHz repetition rate Ti:Sapphire laser. The octave-spanning spectra is reshaped with difference input polarizations controlled by an HWP. We observed the polarization dependence of the output supercontinuum spectrum. Note this polarization-controlled supercontinuum laser can be used as a versatile broadband light source for optical imaging in scattering medium. The Raman solitons near 1100 nm shown in the spectra plots in Figure 5.7 can be wavelength-tuned by simply changing the input power to the photonics crystal fiber. As will be shown in the numerical simulations, the Raman soliton evolve as a whole unit and its state of polarization stays constant across the pulse. This unique constant polarization and wavelength-tunable feature can benefit optical imaging as a powerful broadband light source as discussed in the introduction chapter. The detailed numerical simulations investigating the polarization dynamics of the Raman solitons will be discussed in the next chapter.

5.4 Experiment: Repetition rate doubling of the supercontinuum laser for optical delay line using the polarization rotation technique

For many applications such as polarization-sensitive 2D scanning experiments [116], we need to have a polarized cost-effective supercontinuum laser source with a high repetition rate. Although supercontinuum lasers with 80 MHz repetition rate are available, this can only Nyquist sample a 40 MHz bandwidth, while we need more bandwidth for our 2D scanning system. For this reason, we desire to double the repetition rate of an 80 MHz supercontinuum laser to 160 MHz. Without active optical devices, it is inevitable to lose half the power of the laser. But if the laser is unpolarized, we already lose half the power when polarizing the laser is required, so we can use the other polarization for pulse rate doubling without any additional loss.

An optical delay line is designed and built to double the repetition rate of the NKT supercontinuum laser in the lab using commercially available optical components. To double the repetition rate of a laser, the output pulse train is split into two orthogonally polarized sets, with one set of the pulse train delayed by exactly half of the time period and polarization rotated. Then the two pulse trains can be interleaved to double the pulse repetition rate. As illustrated in Figure 5.8, the original pulse train has a time period of t_0, corresponding to a repetition rate of f_0. It is interleaved with a delayed version of the pulse train with the same amplitude, resulting in an effective time period of $t_0/2$, and a repetition rate of $2f_0$.

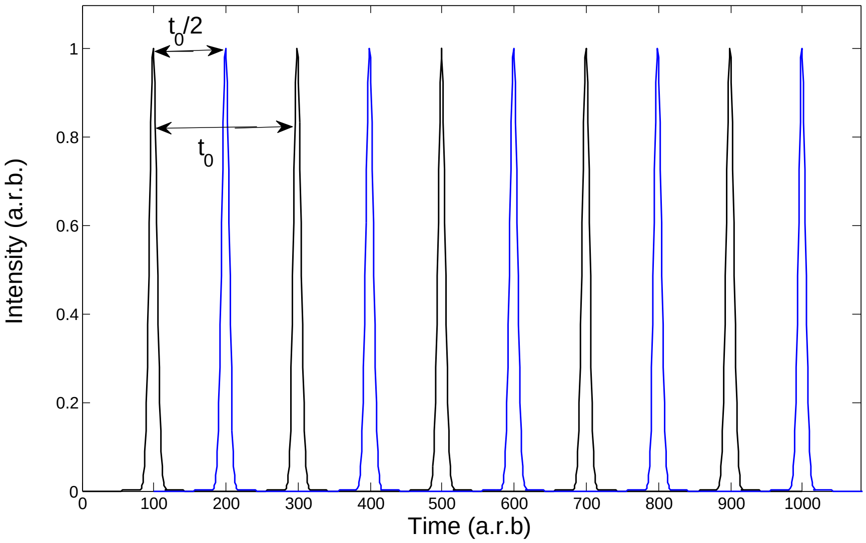

Figure 5.8: Pulse train interleaving for repetition rate doubling.

5.4.1 Broadband polarization rotation using a dielectric mirror system

Since a polarized laser beam is desired for our applications, we need to incorporate a polarization rotation system into the design of the optical delay line. A wave plate can be used to rotate the polarization of an input beam. However, even for a perfectly manufactured wave plate, there will be loss in polarization purity due to the undesired birefringence caused by heating from the high input power laser beam [136, 137]. In addition, for a supercontinuum laser source, an expensive broadband wave plate is required to rotated the polarization across the several hundred nanometers broad spectrum. An achromatic polarization cell design for polarization rotation was proposed [138] for the visible wavelength range, and can be used with multiple wavelengths or tunable lasers. However, this device requires accurate cutting angles of three prisms at mutually perpendicular edges and the thick glasses could introduce dispersion to time domain pulses. Alternatively, we propose using commercially available broadband dielectric mirrors to rotate the polarization of high power supercontinuum laser beams.

Figure 5.9 illustrates the concept of polarization rotation of an incoming beam by tactically

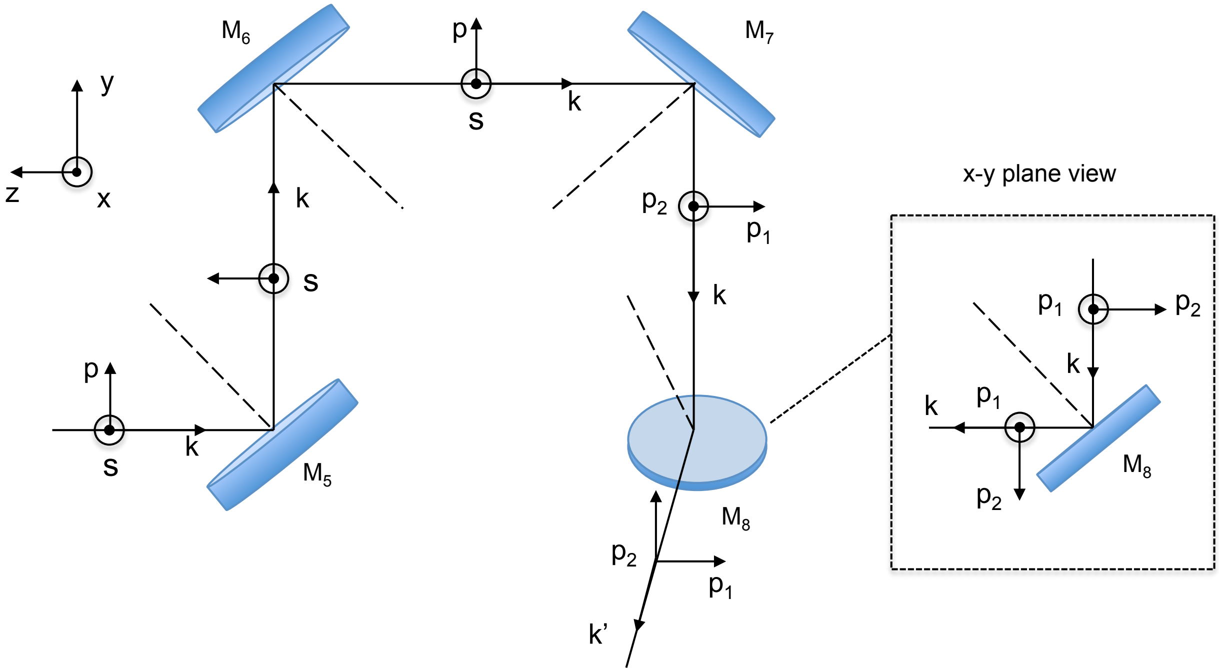

Figure 5.9: Broadband polarization rotation system using four dielectric mirrors. The picture of the system is shown in the insect of Figure 5.10

arranging four broadband dielectric mirrors. The coordinate of the system is shown in the upper left corner. The laser beam propagates in the direction of the k-vector. The normals (dashed line) of the first three mirrors $M_{5,6,7}$ lie in the same y-z plane. The p-polarization changes direction upon reflection from a mirror, whereas the direction of s-polarization remains the same. Therefore, there is a π phase shift between the p and s polarization vectors upon mirror reflection. Since the normal of the fourth mirror M_8 lies in the x-y plane, it is easier to analyze the polarization in that plane, shown in the inset in Figure 5.9. Let's change the notation of the polarization due to the switch of the plane. Let p_1 represent p-polarization and p_2 represent s-polarization. As we can see, the output polarization switches from p to p_1 and s to p_2, respectively. Therefore, if we compare the input and output polarizations in the same x-z plane, we see that eventually at the output of M_8, s-polarization is switched to p-polarization, and vice-versa. Hence, the polarization rotation of the supercontinuum laser beam can be theoretically achieved in the geometry as designed in Figure 5.9 without using broadband wave plates.

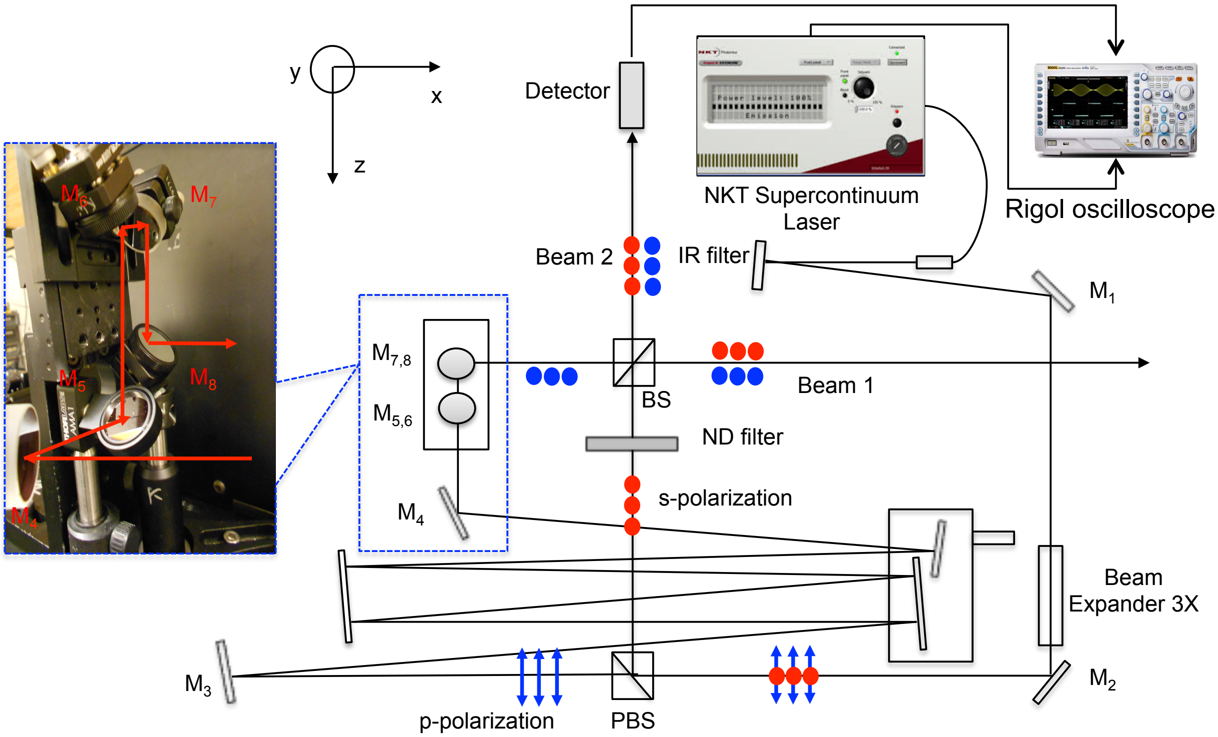

Figure 5.10: Optical delay line setup. The insect shows the picture of the broadband polarization rotation system using four dielectric mirrors (M_5, M_6, M_7 and M_8). BS: beam splitter. PBS: polarization beam splitter.

Figure 5.10 shows the optical delay line experiment setup. An NKT supercontinuum laser is used as the pulse source. This laser emits picosecond pulses at a repetition rate of 78.35 MHz. The output beam of the laser has a diameter of about 1 mm. An IR filter (Optosigma, cold mirror, 034-3110) is used in reflection mode to block the strong infared power, directing the visible spectrum to the optical delay line experiment. Since the laser output beam is about 1 mm in diameter, a 3X beam expander (Melles Griot, 2001-10089) is used to increase the beam diameter to about 3 mm. The focal tuning of the beam expander helps to optimize the beam sizes of the two interleaved pulse trains so that they match and overlap at the output. The polarization beam splitter (Melles Griot, 003PBB007) splits the unpolarized incoming beam to *s*- and *p*-polarizations. The *s*-polarized beam is then sent directly to the non-polarization beam splitter (Thorlabs, BS013), while the *p*-polarized beam travels a longer path by bouncing twice on each of the high reflectivity $2''$ mirrors

(Newport, 20D20BD.1). The total path difference between s and p-polarized beams should equal to $c \times t_0/2 = 3e8m/s \times 6.38ns = 1.905m = 6.25$ feet. The high reflectivity Newport mirrors folds the p-polarized beam in order to create an optical path length difference to about 6.25 feet from the s-polarized beam.

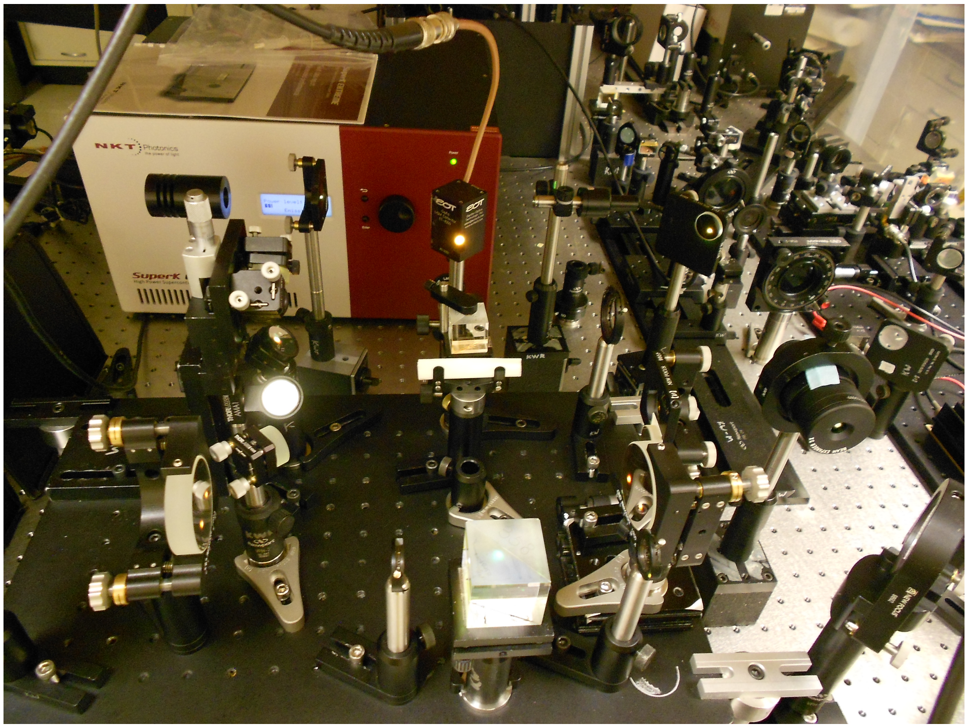

Figure 5.11: Photograph of the optical delay line setup using the broadband polarization rotation system.

Coarse tuning of the path length difference is achieved by translating one of the cavity mirrors mounted on the translation stage that is tunable in the x direction, while fine tuning is achieved by translating mirror 6 and 7 mounted on a trumpet-like stage in the y direction simultaneously. As illustrated in the previous section in Figure 5.9, upon reflections on mirrors M_{5-8}, the polarization of beam 1 is rotated from p to s, co-linear with the polarization of beam 2. Although the input laser beam is unpolarized, we have an s-polarized output beam from the optical delay line as a result of the polarization rotation mirrors. Finally, the two co-linearly polarized beams recombine at the non-polarizing beam splitter (BS), and a detector can be placed at either port of the BS to observe the output pulse train. Figure 5.10 shows a photograph of the optical delay line setup. The output repetition rate from an optical delay line can be measured by either an RF spectrum analyzer (Hewlett Packard, 8560E), or a modified digital oscilloscope (Rigol, DS2072, 200MHz, 1 Gb/s). A GaAs fast photodiode (Electro-optics, ET-4000, bandwidth 8 GHz) is used to detect the output beam. Although the oscilloscope used to observe the time domain data only has a bandwidth of 200 MHz, it is sufficient to see the 160 MHz pulse train. The seed pulse output from the NKT laser is used as an external trigger for the oscilloscope. We detect beam 2 and use beam 1 in the far field as an alignment aid. Figure 5.12a shows time signals measured by the oscilloscope: the trigger signal, the long path signal (beam 1), the short path signal (beam 2) and the interleaved signal. Each set of data is averaged 512 times on the scope to eliminate the unexpectedly large pulse-to-pulse fluctuations of the laser amplitude and polarization. The interleaved beam has a repetition rate of 156.7 MHz. The time delay between the two sets of pulse trains is 6.38 ns. As can be seen, there is a slight imbalance of the interleaved pulse amplitudes and pulse-to-pulse fluctuations.

The single-sided RF output spectrum is calculated by Fast Fourier transform (FFT), and the pulse train is measured by the Rigol oscilloscope. The RF spectrum in Figure 5.12b shows the fundamental interleaved frequency of 156.7 MHz, and the harmonic frequencies 313.4 MHz and 470.1 MHz are also evident. The amplitudes of the harmonic frequencies correspond to the weighting factors of the Fourier series of the periodic waveform. The repetition rate of a picosecond supercontinuum laser is doubled with an optical delay line from 78.35 MHz to 156.7 MHz. At the same time, the unpolarized output beam from the laser is transformed to an s-polarized beam. This experimental result is a promising step for doubling the repetition rate of a future unpolarized laser that would be used for microscopy experiments requiring high bandwidth and polarized input light without the need of a specially designed broadband wave plate. In the previous section, the polarization-controlled supercontinuum light source was experimentally demonstrated, the concept of the optical delay line could be used to double the repetition rate of the supercontinuum light for polarization microscopy requiring high bandwidth and variable states of polarization.

The experimental investigations of supercontinuum generation in a birefringent photonic

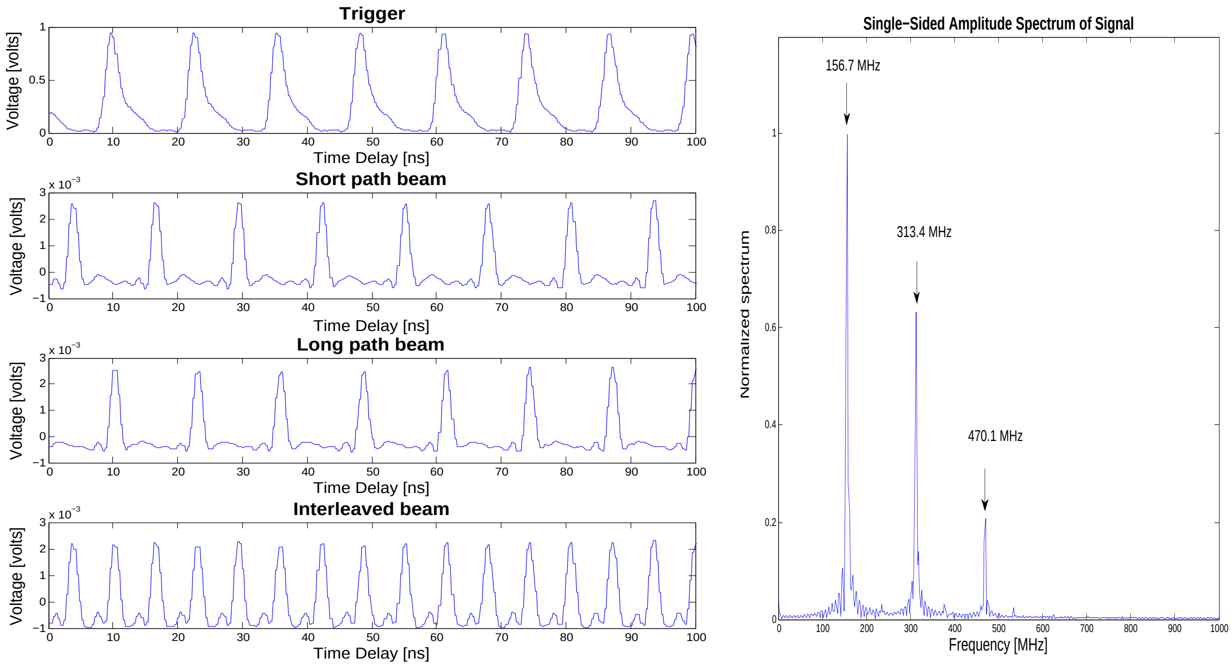

(a) (b)

Figure 5.12: Results for the optical delay line experiment. (a) Output signals measured by oscilloscope. From top to bottom: trigger signal, short optical path beam (s-polarization), long optical path beam (p-polarization) and interleaved beam measured by an oscilloscope, (b) RF spectrum of the output signal.

crystal fiber (PCF) is presented in this chapter. The ultrashort pulse from an ultrafast Ti:Sapphire laser was compressed to 28 fs and was coupled into the highly nonlinear PCF to generate an octave-spanning supercontinuum. The output supercontinuum was observed to be dependent on the input state of polarizations. In particular, the wavelength shift of the Raman soliton depends on the angle of the HWP at the input of the PCF. The observation of the polarization dependence of the supercontinuum provided the motivation to conduct detailed numerical simulations to investigate the underlying physics of the polarization dynamics of the Raman soliton which will be discussed in the next chapter. In addition, an optical delay line experiment was demonstrated to double the repetition rate of a supercontinuum laser. This is potentially useful for optical imaging applications such as broadband 2D polarization-sensitive laser scanning microscopes. Instead of using specially designed broadband wave plate cells, a polarization rotation system is developed using commercially available dielectric mirrors to rotate the polarization of the laser beam and recombine the two beams to double the repetition rate of the supercontinuum laser.

Chapter 6

Polarization dynamics of broadband supercontinuum light source generated in a photonic crystal fiber

In the previous chapter, polarization dependence of supercontinuum generation in a photonic crystal fiber (PCF) was observed experimentally which provided the motivation to study the underlying physics of the polarization dynamics for the octave-spanning broadband light source. In this chapter, I numerically investigate polarization instability of soliton fission and the polarization dynamics of Raman solitons ejected during supercontinuum generation in a photonics crystal fiber using the coupled vector generalized nonlinear Schrödinger equations (GNLSE) for both linear and circular birefringent fibers. The background of supercontinuum generation and the numerical simulation method will be described in details, as well as the investigations of an appropriate Raman response function to be included in the coupled GNLSE simulation for supercontinuum generation. In addition, the numerical algorithm for solving the coupled GNLSE by switching the eigen-polarization basis will be presented.

6.1 Introduction to polarization instability in birefringent fiber

Polarization instability (PI) of solitons in birefringent fiber has been the subject of numerous investigations because of its fascinating underlying physics and potential for practical applications in nonlinear optics. In a birefringent nonlinear fiber, the intensity-dependent refractive index leads to PI for intense continuous-wave (CW) laser fields polarized along the fast-axis [139, 140]. The state of polarization (SOP) of the light during propagation along the birefringent fiber can be represented on a phase plane graph which reveals a polarization separatrix, at which the nonlinear index is commensurate with the birefringence. Similarly, interesting optical bifurcation phenomena associated with this fast-axis instability have been reported [141], and the SOP trajectories were represented on the Poincaré sphere [142].

Unlike the case of CW light, optical solitons require lower average pulsed laser power to observe PI [143, 144]. Unlike quasi-CW light, optical solitons evolve as a unit [145, 146] that can be characterized by a single SOP qualitatively following the CW theory except the soliton stabilizes due to the interplay of dispersion and nonlinearity [147]. The propagation of solitons in birefringent fibers was investigated [148, 147] considering the interactions of its two orthogonal polarization components. Subsequently, vector solitons in birefringent nonlinear fiber were theoretically demonstrated using coupled GNLSE [149]. Almost a decade later, the experimental observation of PI of vector solitons in a weakly birefringent fiber was reported [144].

Since the discovery of supercontinuum generation, soliton fission based supercontinuum in birefringent PCF was found to have polarization-dependent properties [150, 151, 22, 152, 153, 154, 155, 133, 156], indicating a nonlinear coupling between the two orthogonally polarized components [133]. PI and the vectorial nature of soliton fission and Raman solitons produced during SC have been demonstrated in a nearly isotropic tapered PCF for a slightly elliptical input polarization [157]. Localized mode solutions continuously down-shift due to the Raman terms in the generalized nonlinear Schrödinger equation, so they should be referred to as “Raman solitary waves” since they are not true soliton due to the continuous Raman frequency down-shift. However, following the convention in the optics literature, in this thesis, we refer to them as “Raman solitons” [133]. Complex PI of Raman solitons can significantly impact not only the general spectrum but also the output SOP across the SC spectrum.

While the previous investigation laid the groundwork for the study of PI of Raman solitons generated by SC in a birefringent fiber, we extend these results to different linear and elliptical input SOPs for both linear and circular fiber birefringence. In this work, we investigate numerically the polarization dynamics of SC soliton fission and the ejected Raman soliton by systematically varying the input SOP and fiber birefringence. We numerically solve the coupled GNLSE using a vector beam propagation algorithm, in which the dispersion evolution in Fourier space is performed in the fiber eigenmode basis, and the nonlinear evolution is performed in a circular basis. The detailed discussion of this algorithm will be presented in Section 3.6.1. We analyze the SOP evolution of the first emitted Raman soliton after the soliton fission as it propagates down the fiber as a function of input SOP and fiber birefringence. To comprehensively understand the complex nature of PI in SC, the polarization evolution of the soliton fission process and Raman soliton are represented on the Poincaré sphere. Much of the previous work was focused on nonlinear polarization dynamics in linearly birefringent fibers, in this work, we also demonstrate Raman soliton polarization evolution in circularly birefringent PCF using the Poincaré sphere representation.

6.2 Theoretical background of supercontinuum generation

When a short optical pulse propagates along a fiber, dispersion and nonlinear effects influence the temporal shape and frequency spectra. To model the propagation of such short pulses inside a fiber, we start with the wave equation obtained from the Maxwell equations,

$$\nabla \times \nabla \times \mathbf{E} = -\frac{1}{c^2}\frac{\partial^2 \mathbf{E}}{\partial t^2} - \mu_0 \frac{\partial^2 \mathbf{P}}{\partial t^2} \tag{6.1}$$

where $\mathbf{E}$ is the electric field vector, and $\mathbf{P}$ is the induced polarization field vector. The induced polarization and the applied electric field satisfies the general relation,

$$\mathbf{P} = \varepsilon_0(\chi^{(1)}\mathbf{E} + \chi^{(2)}\mathbf{EE} + \chi^{(3)}\mathbf{EEE} + ...) \tag{6.2}$$

where c is the speed of light in vacuum, and ε_0 is the permittivity in vacuum. $\chi^{(\mathrm{i})}$ is the ith order susceptibility, and it is a tensor of rank $i+1$. The linear susceptibility $\chi^{(1)}$ represents the dominant contribution to the polarization $\mathbf{P}$. Its effects are manifested through the refractive index and loss coefficient given by the following,

$$n(\omega) = 1 + \frac{1}{2}Re[\tilde{\chi}^{(1)}(\omega)] \tag{6.3}$$

$$\alpha(\omega) = \frac{\omega}{nc}Im[\tilde{\chi}^{(1)}(\omega)] \tag{6.4}$$

$\chi^{(2)}$ governs the second-harmonic generation and sum-frequency generation [158]. Because SiO_2 is a symmetric molecule, $\chi^{(2)} = 0$ for silica. $\chi^{(3)}$ represents the lowest-order nonlinear effect in a silica fiber such as four-wave mixing, nonlinear refraction and third-harmonic generation [158]. Note that for supercontinuum generation, the effective refractive cladding index strongly depends on the wavelength and the periodic structure of the waveguide. Short optical wavelengths are more confined in the core region, hence the effective refractive cladding index decreases as a function of the wavelength. If only the third-order nonlinear effects governed by $\chi^{(3)}$ are considered, the induced polarization can be written as [133]

$$\mathbf{P} = \mathbf{P}_{NL} + \mathbf{P}_L \tag{6.5}$$

where $\mathbf{P}_{NL}$ and $\mathbf{P}_L$ represent the nonlinear and linear polarization, respectively. They are given by the following,

$$\mathbf{P}_L(\mathbf{r},t) = \varepsilon_0 \int\limits_{-\infty}^{t} \chi^{(1)}(t-t^{'}) \cdot \mathbf{E}(\mathbf{r},t)\, dt^{'} \tag{6.6}$$

$$\mathbf{P}_{NL}(\mathbf{r},t) = \varepsilon_0 \iiint\limits_{-\infty}^{t} \chi^{(3)}(t-t_1, t-t_2, t-t_3) \cdot \mathbf{E}(\mathbf{r}_1,t)\mathbf{E}(\mathbf{r}_2,t)\mathbf{E}(\mathbf{r}_3,t)\, dt_1 dt_2 dt_3 \tag{6.7}$$

The equation of $\mathbf{P}_{NL}(\mathbf{r},t)$ describes a variety of third-order intensity-dependent nonlinear effects. The above equations can be simplified with several approximations.

For silica glass, the third-order susceptibility can be written in terms of three independent elements [133]

$$\chi^{(3)}{}_{ijkl} = \chi^{(3)}{}_{xxyy}\delta_{ij}\delta_{kl} + \chi^{(3)}{}_{xyxy}\delta_{ik}\delta_{jl} + \chi^{(3)}{}_{xyyx}\delta_{il}\delta_{jk} \tag{6.8}$$

where δ_{ij} can be defined as $\delta_{ij} = 1$ for $i = j$ and $\delta_{ij} = 0$ otherwise. We get $\chi^{(3)}{}_{xxxx} = \chi^{(3)}{}_{xxyy} + \chi^{(3)}{}_{xyxy} + \chi^{(3)}{}_{xyyx}$ because of the rotational symmetry of isotropic silica glass. For silica glass, the three components of $\chi^{(3)}{}_{xxxx}$ have almost the same magnitude, hence they can be assumed to be the same. In general, the third-order susceptibility in the equation of $\mathbf{P}_{NL}(\mathbf{r},t)$ can be written as [159]

$$\chi^{(3)}(t-t_1, t-t_2, t-t_3) = \chi^{(3)}R(t-t_1)\delta(t-t_2)\delta(t-t_3) \tag{6.9}$$

where $R(t)$is the nonlinear response function normalized such that $\int\limits_{-\infty}^{\infty} R(t)dt = 1$. Note $\chi^{(3)}$ affects the polarization of the optical field through nonlinear birefringence, which will be discussed in this chapter. The derivations of electronic and resonant nuclear susceptibility parts ${\chi^{\mathrm{E}}}_{ijkl}$ and ${\chi^{\mathrm{R}}}_{ijkl}$ will be discussed in Section 6.4. In the slowly varying envelope approximation, we can separate the rapidly varying part of the electric field. The electric field $\mathbf{E}(\mathbf{r}, t)$ can be written as

$$\mathbf{E}(\mathbf{r}, t) = \frac{1}{2}\hat{x}[F(x, y)A(z, t)e^{i\beta_o z - i\omega_0 t} + c.c.] \tag{6.10}$$

where $\hat{x}$ is the polarization unit vector, $A(z, t)$ is the slowly varying pulse envelope, $F(x, y)$ is the modal distribution and the fundamental mode which can be approximated by a Gaussian in a single mode fiber, hence we can have $F(x, y) \approx e^{-(x^2+y^2)/w^2}$, where w is the width of Gaussian [133]. The details of the fiber mode are covered in several resources for interested readers [160, 161, 162]. Assuming the slowly varying optical field Eqn. 6.10, we can then substitute Eqn. 6.9 into $\mathbf{P}_{NL}(\mathbf{r}, t)$, assuming a linearly polarized optical field so that one component of ${\chi^{(3)}}_{xxxx}$ of the fourth-rank tensor contributes to the refractive index, the scalar form of the nonlinear polarization can be written as

$$\mathbf{P}_{NL}(\mathbf{r}, t) = \frac{3\varepsilon_0}{4}{\chi^{(3)}}_{xxxx} \int\limits_{-\infty}^{t} R(t - t_1)E^*(\mathbf{r}, t_1)E(\mathbf{r}, t_1)dt_1 \tag{6.11}$$

where $R(t)$ is the normalized nonlinear response function which should include both the electronic (instantaneous) and nuclear components,

$$R(t) = (1 - f_R)\delta(t - t_e) + f_R h_R(t) \tag{6.12}$$

The details of the nonlinear response function will be investigated in Section 6.4. Now we can apply the slowly varying envelope approximation and take into account the frequency dependence of wave number β by Taylor series expansion around the center frequency ω_0,

$$\beta(\omega) = \beta_0 + (\omega - \omega_0)\beta_1 + \frac{1}{2}(\omega - \omega_0)^2\beta_2 + ... \tag{6.13}$$

Similarly, Taylor expand the nonlinear coefficient γ and the loss coefficient α around the center frequency ω_0, respectively,

$$\gamma(\omega) = \gamma(\omega_0) + \gamma_1(\omega - \omega_0) + \frac{1}{2}\gamma_2(\omega - \omega_0)... \tag{6.14}$$

$$\alpha(\omega) = \alpha(\omega_0) + \alpha_1(\omega - \alpha_0) + \frac{1}{2}\alpha_2(\omega - \omega_0)... \tag{6.15}$$

where the nonlinear parameter is defined as,

$$\gamma(\omega_0) = \frac{n_2(\omega_0)\omega_0}{cA_{eff}} \tag{6.16}$$

where n_2 is is nonlinear-index coefficient and A_{eff} is the effective mode area defined as,

$$A_{eff} = \frac{\left(\iint_{\infty}^{-\infty}|F(x,y)|^2\,dx\,dy\right)^2}{\iint_{\infty}^{-\infty}|F(x,y)|^4\,dx\,dy} \tag{6.17}$$

The model distribution $F(x, y)$ shown in Eqn. 6.10 can be used to evaluate A_{eff}. For a fundamental Gausian mode in a single mode fiber, since $F(x, y) \approx e^{-(x^2+y^2)/w^2}$, A_{eff} can be approximated as $A_{eff} = \pi w^2$. For highly nonlinear fiber, which will be discussed later, the value of A_{eff} is extremely small and can be on the order of the optical wavelength to increase nonlinearity.

6.2.1 Generalized Nonlinear Schrödinger Equations

Using the slowly varying envelope approximation and retaining the first two erms in the $\gamma(\omega)$ and $\alpha(\omega)$ Taylor expansions, the scalar form of the pulse propagation equation inside a single mode fiber is given by the following [163],

$$\begin{aligned}\frac{\partial A}{\partial z} + \frac{1}{2}(\alpha(\omega_0) + i\alpha_1\frac{\partial}{\partial t})A + \beta_1\frac{\partial}{\partial t} + \frac{i\beta_2}{2}\frac{\partial^2 A}{\partial^2 t} - \frac{\beta_3}{6}\frac{\partial^3 A}{\partial t^3} + ...\\ = i\gamma(\omega_0)(1 + \frac{i}{\omega_0}\frac{\partial}{\partial t})(A(z,t)\int\limits_0^\infty R(t^{'})|A(z,t-t^{'})|^2 dt^{'})\end{aligned} \tag{6.18}$$

This equation accounts for the loss, dispersion and intrapulse Raman scattering-related nonlinear effects. Higher order dispersion terms should be included for the numerical simulation of supercontinuum generation. However, there is some debate about the physical validity of using the slowly varying envelope assumption for short optical pulses (in the order of a few optical cycles)

[164]. Theoretical works such as [165] have shown that the slowly varying envelope approximation can be applied to even the single optical cycle regime. For practical numerical modeling, the equation needs to be transformed to the co-moving frame at the group velocity, that is, the group velocity frame, by making the transformation of the following,

$$T = t - \frac{z}{v_g} = t - \beta_1 z \tag{6.19}$$

Hence, by substituting

$$\frac{d}{dt} = \frac{d}{dT} \tag{6.20}$$

$$\frac{d}{dz} = \frac{d}{dz} - \frac{1}{v_g}\frac{d}{dT} \tag{6.21}$$

into the above derived pulse propagation equation and by adding higher order dispersion terms we get the GNLSE for modeling supercontinuum generation,

$$\begin{aligned} &\frac{\partial A}{\partial z} + \frac{1}{2}(\alpha(\omega_0) + i\alpha_1 \frac{\partial}{\partial T})A + \sum_{n\geqslant 2}^{N} i^{n-1}\frac{\beta_n}{n!}\frac{\partial^n A}{\partial T^n} \\ &= i\gamma(\omega_0)(1 + \frac{i}{\omega_0}\frac{\partial}{\partial T})(A(z,T)\int_0^\infty R(T^{'})|A(z,T-T^{'})|^2 dT^{'}) \end{aligned} \tag{6.22}$$

where n represents the order up to which dispersion effects are included. Notice that β_1 term is eliminated as a result of the transformation to the group velocity frame. The left hand side of the equation models the linear propagation effect. For short fiber propagation length, the loss terms can be ignored.

The right hand side of the equation models nonlinear effects in the fiber, while the time derivative models the dispersion of the nonlinearities. The terms with $\frac{1}{\omega_0}\frac{\partial}{\partial T})$ are responsible for self-steepening and optical shock, which is a key factor in allowing the envelope-based GNLSE to be extended into the single-cycle regime. Note self-steepening is results from the intensity dependence of group velocity and leads to an asymmetric self-phase modulation broadened spectra for short pulses. Optical shock is created by self-steepening of a short pulse. The integral terms represent the delayed Raman response, which plays an important role in supercontinuum modeling and will be discussed in detail.

6.3 Numerical method for solving the coupled generalized Nonlinear Schrödinger Equations

Numerical methods are usually effective in helping us understand the nonlinear effects represented in the GNLSE discussed in the previous section. In the case of supercontinuum generation, the split-step Fourier method [166] and Runge-Kutta method [167] can be used to solve the GNLSE (although the analytical solution of GNLSE can be obtained using the inverse scattering method, the method is only valid for some specific cases [168], we discuss the more often used numerical approaches in this section.) The split-step Fourier method (SSFM) is frequently used in modeling the GNLSE for supercontinuum generation. This method separates the GNLSE into two parts,

$$\frac{\partial A}{\partial z} = [\tilde{D} + \tilde{N}] \tag{6.23}$$

where $\tilde{D}$ is a dispersion operator and $\tilde{N}$ is a nonlinear operator. From the scalar GNLSE, they are given by the following,

$$\tilde{D} = -\sum_{n=2}^{N} i^{n-1} \frac{\beta_n}{n!} \frac{\partial^n}{\partial t^n} \tag{6.24}$$

$$\tilde{N} = i\gamma(\omega_0)(1 + \frac{i}{\omega_0}\frac{\partial}{\partial T})(\int_0^{\infty} R(T^{'})|A(z, T - T^{'})|^2 dT^{'}) \tag{6.25}$$

If a pulse is propagated in a small distance h, then from z to $z + h$ it is carried out in two steps. The advance of the field over a step h can be approximated as the following,

$$A(z, z + h) \approx \exp(h\tilde{D}) \exp(h\tilde{N}) A(z, T) \tag{6.26}$$

In SSFM, the dispersion and nonlinear effects are calculated in two independent steps. The dispersion term is calculated in Fourier domain using the Fast-Fourier transform (FFT). Since the dispersion and the nonlinear terms don't commute, the solution is an approximation to the exact solution. The second-order accuracy of the SSFM can be improved by adopting a more symmetric approach to distribute the step h. This method is the symmetric split-step Fourier method (SSSFM) which is thrid-order accurate in step size h. The solution of SSSFM over a step h is given by

$$A(z, z+h) \approx exp\Big(\frac{h}{2}\tilde{D}\Big)exp\Big(\int_{z}^{z+h} \tilde{N}dz\Big)exp\Big(\frac{h}{2}\tilde{D}\Big)A(z,T) \tag{6.27}$$

In SSSFM, the nonlinear terms represented by an integral can be evaluated by approximating it as $exp(h\tilde{N})$. However, this accuracy can be further improved by approximating the integral term more precisely than approximating it by $h\hat{N}(z)$ [133]. The downside is the process is iterative and will be very time-consuming in computation.

6.4 Raman response function for supercontinuum generation

The Raman effect was discovered by C.V. Raman in 1928 and is well-known for its applications in Raman amplifiers, Raman microscopy, Raman lasers, supercontinuum generation and other high order nonlinear effects. It impacts the ultrashort pulse propagation in an optical fiber and can lead to a number of nonlinear phenomenas, including soliton fission, Raman-induced frequency shift and supercontinuum generation. It is essential to understand the Raman effect for supercontinuum generation modeling.

The Raman effect typically rises from the motion of a molecule inside silica fiber in response to an applied electromagnetic field. It can be derived from harmonic oscillators representing molecule vibrations [169]. On the quantum mechanics level, the Raman effect can be interpreted as the scattering of a photon by a molecule to a lower frequency state. On the optical wave level, Raman effect can be seen as a frequency down-shift of the optical radiation generated by a pump optical wave while interacting with an optical medium such as silica fiber. Due to the Raman effect's impact in ultrashort optics and supercontinuum generation, many efforts has been made to characterize the nonlinear response properties of silica fiber to model the Raman response function. In this section, I will discuss and compare the models of the Raman response function for numerically simulating supercontinuum generation.

6.4.1 Single Lorentzian and 13-peaks Raman response models

In general, the nonlinear response function $R(t)$ has the form [133, 164]

$$R(t) = (1 - f_R)\delta(t) + f_R h_R(t) \tag{6.28}$$

where the first term accounts for the instantaneous electronic response, and the second term accounts for the nuclear response. f_R represents the fractional contribution of the delayed Raman response to the nonlinear polarization $\mathbf{P}_{NL}$. Numerous efforts have been made to estimate an analytical form of the Raman response function $h_R(t)$. One widely adopted form of $h_R(t)$ used in the literature is given by the following,

$$h_R(t) = t_1 \left(\frac{1}{t_1^2} + \frac{1}{t_2^2} \right) e^{-\frac{t}{t_2}} sin \left(\frac{t}{t_1} \right) \tag{6.29}$$

When fit to fused silica, the best fit is given by $t_1 = 12.2$ fs, $t_2 = 32$ fs and $f_R = 0.18$. This form of Raman response function has been frequently used to investigate ultrafast nonlinear effects in optical fibers because of its simplicity. To obtain this analytical Raman response function, a single Lorentzian function is fitted to the Raman gain experimental data measured by Stolen for fused silica [170], shown as the black solid line in Figure 6.1.

The dotted black line represents the single Lorentzian fit. There are five peaks in the frequency range of 0 to 25 THz. Comparing the two curves, we see the single Lorentzian model under-estimates the Raman gain in the frequency range less than 10 THz, while over-estamating it for frequencies greater than 15 THz. One should be careful when using the simplified single oscillator model, because it approximates the Stolen experimental data by fitting a single Lorentzian function, failing to reproduce the hump at frequencies below 5 THz and above 15 THz [133].

In 2002, Hollenbeck and Cantrell developed a model that fits an ensemble of 13 Gaussian and Lorentzian functions to the experimental data [171]. This model extends the one proposed by Walrafen and Krishman in 1982 [172] when the experimental spectroscopic data was not measured yet. Although it is common to use the experimentally determined Raman cross section [170], essentially identical results can be obtained using the sophisticated 13-peaks Hollenback-Cantrell

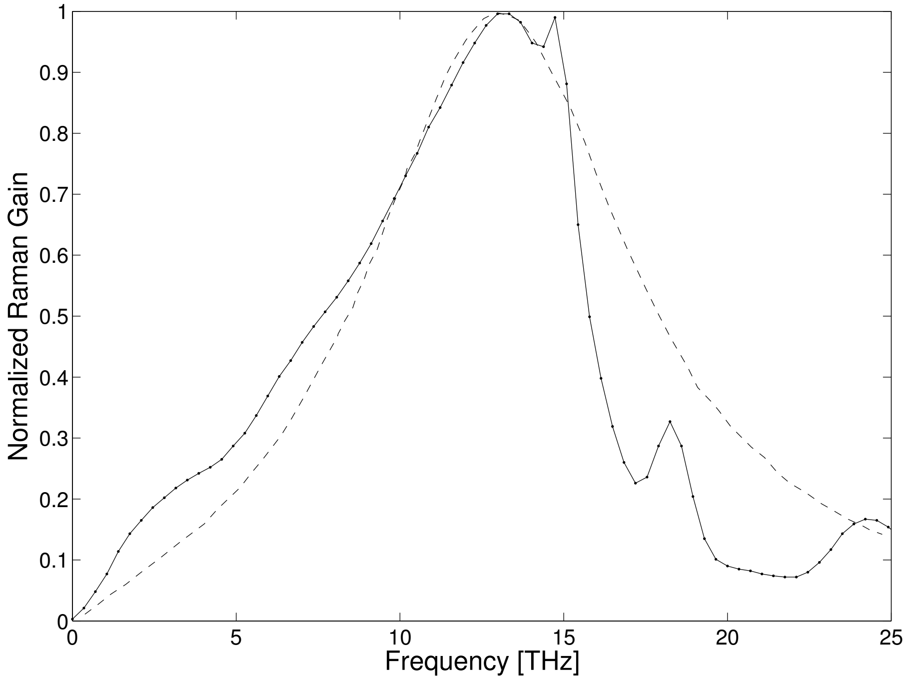

Figure 6.1: Raman gain spectra. Experimental data from Stolen (black solid line) by digitizing Stolen's experimental data; single Lorentzian model (black dotted line).

or the Blow-Wood model [164]. However, owing to its complexity, the 13-peaks Hollenback-Cantrell model is often impractical to model.

6.4.2 Lin and Agrawal Raman response model

While the simple single Lorentzian model and the complicated 13-peaks Hollenback-Cantrell model are two extremes of estimating the Raman response function, an intermediate form of the Raman response function that correctly models the anisotropic response function was proposed by Agrawal and Lin in 2006 [173]. The Agrawal and Lin model considers the anisotropic nature of the Raman scattering effect by including an appropriate but simple anisotropic part of the Raman response function. This section derives the isotropic and the anisotropic parts of the nonlinear response function from the polarization equations.

From the polarization equations $\mathbf{P}_{NL}(\mathbf{r},t)$ and $\mathbf{P}_{L}(\mathbf{r},t)$ 6.6 derived earlier, we can substitute the equation of $\chi^{(3)}$ into $\mathbf{P}_{NL}$,

$$\begin{aligned}\mathbf{P}_{NL}(z,t) &= \varepsilon_0[\iiint\limits_{-\infty}^{t} \chi^{(3)} R(t-t_1)\delta(t-t_2)\delta(t-t_3)\cdot \mathbf{E}(z,t_1)\mathbf{E}(z,t_2)\mathbf{E}(z,t_3)dt_1dt_2dt_3] \\ &= \varepsilon_0[\chi^E_{ijkl}\mathbf{E}_j\mathbf{E}_k\mathbf{E}_l + \mathbf{E}_j \int\limits_{-\infty}^{t} \chi^R_{ijkl}(t-t^{'})\mathbf{E}_k\mathbf{E}_l dt^{'}] \end{aligned} \tag{6.30}$$

where

$$\chi^{(3)}(t-t_1, t-t_2, t-t_3) = \chi^{(3)} R(t-t_1)\delta(t_1-t_2)\delta(t-t_3) \tag{6.31}$$

In isotropic media, the instantaneous electrons obey full Kleinman symmetry [174], so we have the electronic susceptibility, [175]

$$\chi^E_{ijkl} = \frac{1}{3}\chi^{(3)}(\delta_{ij}\delta_{kl} + \delta_{ik}\delta_{jl} + \delta_{il}\delta_{jk}) \tag{6.32}$$

and the resonant nuclear susceptibility is given by the following,

$$\chi^R_{ijkl} = h_a(t)\delta_{ij}\delta_{kl} + \frac{1}{2}h_b(t)(\delta_{ij}\delta_{kl} + \delta_{ik}\delta_{jl}) \tag{6.33}$$

Therefore, substituting χ^E_{ijkl} and χ^R_{ijkl} into $\chi^{(3)}$, we can write the nonlinear response function of silica in tensor form,

$$\begin{aligned} R^{(3)}_{ijkl}(t) = \frac{1-f_R}{3}\delta(t)(\delta_{ij}\delta_{kl} + \delta_{ik}\delta_{jl} + \delta_{il}\delta_{jk}) + \\ f_R R_a(t)\delta_{ij}\delta_{kl} + \frac{f_R}{2}R_b(t)(\delta_{ik}\delta_{jl} + \delta_{il}\delta_{jk}) \end{aligned} \tag{6.34}$$

The linear polarized form of the nonlinear response function is given by [173],

$$R^{(3)}_{xxxx}(t) = (1-f_R)\delta(t) + f_R h_R(t) \tag{6.35}$$

where

$$h_R(t) = R_a(t) + R_b(t) \tag{6.36}$$

$$R_a(t) = f_a h_a(t) \tag{6.37}$$

$$R_b(t) = f_b h_b(t) + f_c h_a(t) \tag{6.38}$$

$R_a(t)$ and $R_b(t)$ are the isotropic and anisotropic parts of the Raman response, respectively. The coefficients should satisfy $f_a + f_b + f_c = 1$. $h_a(t)$ is given by

$$h_a(t) = t_1(t_1^{-2} + t_2^{-2})e^{-\frac{t}{t_2}}sin(\frac{t}{t_1}) \tag{6.39}$$

where $t_1 = 12.2$ fs and $t_2 = 32$ fs. $h_a(t)$ has been used by the single Lorentzian model. The isotropic Raman response stems from the symmetric stretching motion of the bridging oxygen atom in the Si-O-Si bond [133]. It turns out that this particular motion can be modeled by a single-Lorentzian function. However, the anisotropic response function needs to be included in the model to provide an accurate description of the total nonlinear Raman response. Agrawal and Lin fitted multiple Lorenztian functions to the experimental Raman gain data, and so $h_b(t)$ was found to be well modeled by

$$h_b(t) = \exp(-t/t_b)\frac{2t_b - t}{t_b^2} \tag{6.40}$$

where $t_b = 96$ fs. $h_a(t)$ and $h_b(t)$ are plotted in Figure 6.2. The causality of the Raman response function is seen in the plot because $h_{a,b}(t) = 0$ for $t < 0$. Substituting $R_a(t)$, $R_b(t)$ into $R^{(3)}_{xxxx}(t)$, we get,

$$R^{(3)}_{xxxx}(t) = (1 - f_R)\delta(t) + f_R(f_a + f_c)h_a(t) + f_R f_b h_b(t) \tag{6.41}$$

Therefore,

$$f_R = f_R(f_a + f_c) + f_R f_b = f_R(f_a + f_b + f_c)$$

Hence the coefficients should satisfy $f_a + f_b + f_c = 1$. In the Agrawal and Lin model, the values of f_a, f_b and f_c are calculated as $f_a = 0.75, f_b = 0.21, f_c = 0.04$. Since the equation of the Raman response includes both isotropic and anisotropic response contributions, the Raman gain in silica fibers is given by the following,

$$g_a(\omega) = 2\gamma f_R Im[\tilde{R_a}(\omega)] \tag{6.42}$$

$$g_b(\omega) = 2\gamma f_R Im[\tilde{R_a}(\omega)] \tag{6.43}$$

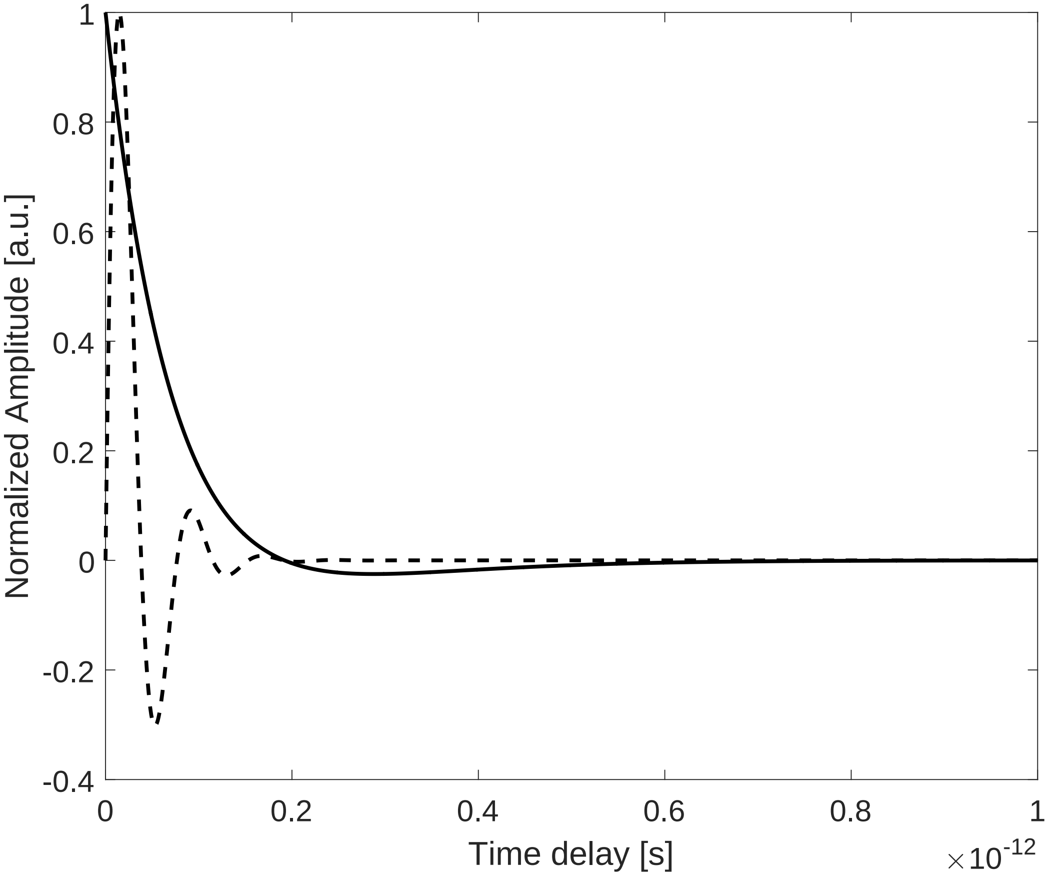

Figure 6.2: Raman response function $h_a(t)$ (black dashed line) and $h_b(t)$ (black solid line)

In this equation, $\gamma = n_2\omega_0/c$ is the nonlinear parameter and $\tilde{R}_{a,b}(\omega)$ is the Fourier transform of $\tilde{R}_{a,b}(t)$. The Raman gain for co-polarized and orthogonally polarized pumps are respectively found to be,

$$g_{\|}(\omega) = g_a(\omega) + g_b(\omega) \tag{6.44}$$

$$g_{\perp}(\omega) = g_b(\omega)/2 \tag{6.45}$$

Figure 6.3 shows the $g_{\|}(\omega)$ and $g_{\perp}(\omega)$ from Agrawal and Lin and are plotted to fit the experimental data from Stolen. f_R is chosen to be 0.245 to yield a Boson peak in the Raman gain equal to the experimental value of $g_R = 1.2e^{-11}$ cm/W at 795.5 nm. This choice allows the model to accurately simulate the Raman gain over $0-15$ THz. In addition, it describes well the Raman-induced changes in the nonlinear refractive index over the same frequency range.

The value of $f_R = 0.245$ is slightly higher than the 0.18 used in the single Lorentzian model, because the single Lorentzian model over-estimates the Raman gain in the spectral region below 15 THz. This results in an under-estimated electronic contribution to the nonlinear refractive index by about 5%. This under-estimation does not affect the nonlinear effects until the pulse width approaches the few-optical-cycle regime (< 30 fs). Because the conventional single-Lorentzian model neglects the anisotropic response of the Raman function $R_b(t)$, it does not provide an accurate description of the Raman response. To account for the anisotropic part, the new model suggested

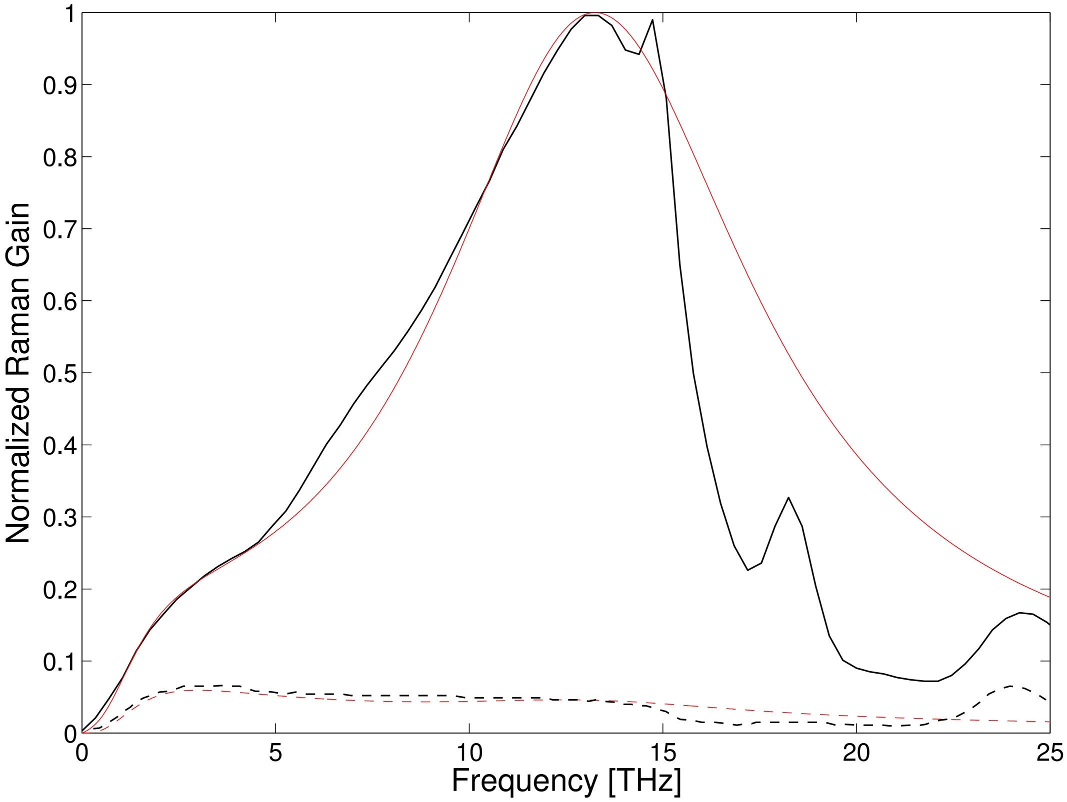

Figure 6.3: Raman gain spectra. Experimental data from Stolen: $g_\perp$ (black solid line) and $g_\parallel$ (black dotted line); fitting model: $g_\perp$ (red solid line) and $g_\parallel$ (red dotted line).

by Agrawal and Lin fits well both the Raman gain and Raman induced-changes in the nonlinear refractive index over $0-15$ THz. This model provides a more accurate description of the Raman response function for numerical simulation of the supercontinuum generation in optical fibers.

6.5 Coupled Generalized Nonlinear Schrödinger Equations

The GNLSE derived before describes a general model for the dispersion and nonlinear processes in a typical supercontinuum generation. Since we know the GNLSE is derived as shown in Eqn. 6.22. This equation can be applied to model non-birefringent supercontinuum generation in optical fiber, or for the special case that input polarization is exactly aligned to the eigen-axis of the fiber. In essence, the GNLSE is a simplified equation that assumes the polarization of the input light is preserved propagating inside a fiber.

However, this is not necessarily the case in reality. Even a single mode fiber (SMF) is not truly single mode. In fact, a SMF supports two orthogonal polarization modes with the same spatial distribution [133]. For an ideal fiber, the two modes are degenerate, which means the refractive indexes along the slow and the fast axis are equal ($n_x = n_y$). In practice, most optical fibers exhibit birefringence as a result of irregularities of core size and shape along the fiber. PCF usually has some intrinsic birefringence due to built in asymmetry of the structure. Therefore, to describe the inherent birefringent effect in optical fiber, we can separate index of refraction along the principle axis x and y as n_x and n_y and introduce a birefringence and a beat length parameter,

$$B_m = n_x - n_y \tag{6.46}$$

$$L_B = \lambda / B_m \tag{6.47}$$

For highly birefringent fiber, B_m is in the order of 10^{-4}, and the beat length is around 1 cm. For a weakly birefringence fiber, B_m is in the order of 10^{-6}, and the beat length can be up to 1 m. In some cases, the optical fibers are made to be highly birefringent in order to provide a stable eigenmode to maintain polarization of light propagation for supercontinuum generation. Therefore, to gain more insights into the polarization effect we have observed experimentally, it is necessary to develop a model that incorporates birefringence into the GNLSE.

To extend the GNLSE to include polarization effects for birefringent fibers, we need to split the GNLSE into coupled mode equations for two orthogonal polarizations. In the following section, the numerical investigation of pulse propagation in nonlinear birefringent fibers and the polarization dynamics will be presented. The numerical simulation algorithm using an eigen-polarization basis switching technique for the split-step Fourier method will also be discussed in details.

We begin with a study of linearly birefringent PCF, but we use a representation in the circular basis where the phase-dependent four-wave mixing term (FWM) is absent, which simplifies both the analytic representation and the numerical scheme. To reveal the underlying polarization effects of soliton fission and Raman soliton in SC, a model which takes into account the fiber birefringence effect requires the coupled GNLSE [154, 133, 10],

$$\begin{aligned}&\frac{\partial A_\pm}{\partial z}+\frac{1}{2}\alpha A_\pm+\sum_{n\geqslant 2}^{N} i^{n-1}\frac{\beta_n}{n!}\frac{\partial^n A_\pm}{\partial T^n}-i\left(\frac{\Delta\beta_0}{2}-\frac{\Delta\beta_1}{2}\frac{\partial}{\partial T}\right)A_\mp\\&=i\gamma(\omega_0)\left(1+\frac{i}{\omega_0}\frac{\partial}{\partial T}\right)\Big(A_\pm(z,T)\Big[f_R\int_0^\infty R(T')[|A_\pm(z,T-T')|^2+|A_\mp(z,T-T')|^2]dT'\\&+(1-f_R)[\frac{2}{3}|A_\pm(z,T)|^2+\frac{4}{3}|A_\mp(z,T)|^2]\Big]\Big)\end{aligned}\tag{6.48}$$

where A_+ and A_- are the electric field amplitudes of the two circularly polarized components. The circular polarization electric fields are related to the linear polarization electric fields as the following,

$$A_+=\frac{A_x+iA_y}{\sqrt{2}},\quad A_-=\frac{A_x-iA_y}{\sqrt{2}}\tag{6.49}$$

This model also incorporates all orders of dispersion, optical shock, Raman and Kerr nonlinearities as shown in Figure 6.4. T is the time reference in the group velocity frame, β_n is the n-th order dispersion parameter centered at frequency ω_0, and α is the loss coefficient which we neglect for a short length of fiber. We define linear birefringence $B=n_x-n_y$, where n_x and n_y are refractive indexes for the x and y polarization eigen-modes, respectively. $\Delta\beta_0=\beta_x-\beta_y=B\omega_0/c$ represents the phase mismatch due to fiber birefringence. $\Delta\beta_1=\frac{1}{v_{gx}}-\frac{1}{v_{gy}}=\epsilon B/c=\beta_{1x}-\beta_{1y}$ represents the group velocity mismatch between the slow and fast axes, where ϵ is a constant which typically varies between 0.38 and 1.3 [10].

$$\frac{\partial A_\pm}{\partial z} + \overbrace{\frac{1}{2}\alpha A_\pm}^{\text{Loss}} + \overbrace{\sum_{n\geqslant 2}^{N} i^{n-1}\frac{\beta_n}{n!}\frac{\partial^n A_\pm}{\partial T^n}}^{\text{Dispersion}} - \overbrace{\left(i\frac{\Delta\beta_0}{2} - \frac{\Delta\beta_1}{2}\frac{\partial}{\partial T}\right)}^{\text{Fiber birefringence}}A_\mp = i\gamma(\omega_0)\left(1+\overbrace{\frac{i}{\omega_0}\frac{\partial}{\partial T}}^{\text{Optical shock}}\right)$$

$$\left(A_\pm(z,T)\left[f_R\int_0^\infty \underbrace{R(T')}_{\text{Raman}}\left[|A_\pm(z,T-T')|^2+|A_\mp(z,T-T')|^2\right]dT' + (1-f_R)\left[\underbrace{\frac{2}{3}|A_\pm(z,T)|^2}_{\text{SPM}} + \underbrace{\frac{4}{3}|A_\mp(z,T)|^2}_{\text{XPM}}\right]\right]\right)$$

Figure 6.4: Nonlinear terms in the coupled generalized Nonlinear Schrödinger Equations.

In our simulation we assume $\epsilon = 1$ for the case of equal dispersion slopes between $\beta_x(\omega)$ and $\beta_y(\omega)$ because separate dispersion curves for x and y polarization components are not available. $R(T)$ is the Raman response function taking into account both the instantaneous electronic and delayed molecular response of fused silica. They are well approximated by [176],

$$R(t) = (1 - f_R)\,\sigma(t) + f_R\left(f_a h_a(t) + f_b h_b(t) + f_c h_a(t)\right) \tag{6.50}$$

where

$$h_a(t) = t_1\left(t_1^{-2} + t_2^{-2}\right)e^{-\frac{t}{t_2}}sin\left(\frac{t}{t_1}\right), \quad h_b(t) = e^{-\frac{t}{t_b}}\frac{2t_b - t}{t_b^2} \tag{6.51}$$

The characteristic time constants and weighting factors we used are $t_b = 96$ fs, $t_1 = 12.2$ fs, $t_2 = 32$ fs, $f_a = 0.75$, $f_b = 0.21$, $f_c = 0.04$ and $f_R = 0.245$ [159, 176].

Following [150], dispersion parameters of the PCF are given in Figure 6.5. These parameters correspond to a fiber with a zero dispersion wavelength at 743 nm and a laser pulse central wavelength of $\lambda_0 = 800$ nm in the anomalous dispersion regime. The nonlinear coefficient is $\gamma = 80$ kW^{-1} m^{-1}, and the peak input power $P_{peak} = 10$ kW is sufficient to produce 13th order solitons of the GNLSE for a Sech input pulse width $T_{FWHM} = 100$ fs. The loss term $\alpha = 0$ for the simulated

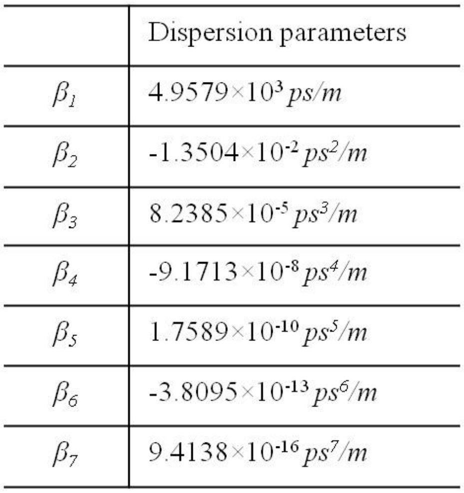

	Dispersion parameters
β_1	$4.9579\times10^{3}\ ps/m$
β_2	$-1.3504\times10^{-2}\ ps^2/m$
β_3	$8.2385\times10^{-5}\ ps^3/m$
β_4	$-9.1713\times10^{-8}\ ps^4/m$
β_5	$1.7589\times10^{-10}\ ps^5/m$
β_6	$-3.8095\times10^{-13}\ ps^6/m$
β_7	$9.4138\times10^{-16}\ ps^7/m$

Figure 6.5: Dispersion parameters for the photonic crystal fiber

fiber length of $L_{fiber} = 8$ cm.

6.5.1 Numerical algorithm for solving the coupled GNLSE using the eigen-polarization basis switching technique

So far the coupled GNLSE has been represented in a circular polarization basis as in Eqn. 6.48. However, it can also be represented with a linear polarization basis as the following,

$$\begin{aligned}
i\frac{\partial A_{x,y}}{\partial z} + i\beta_{1x}\frac{\partial A_{x,y}}{\partial z} + i\sum_{n\geqslant 2}^{N} i^{n-1}\frac{\beta_n}{n!}\frac{\partial^n A_{x,y}}{\partial T^n} & \\
= \gamma(1-f_R)A_{x,y}|A_{x,y}(T-T^{'})|^2 &+ \frac{2}{3}(1-f_R)\gamma|A_{y,x}(T-T^{'})|^2A_{x,y} \\
&+ \gamma f_R A_{x,y}\int\limits_0^{\infty} a(T^{'})|A_{y,x}(T-T^{'})|^2 + [a(T^{'})+b(T^{'})]|A_{x,y}(T-T^{'})|^2 dT^{'} \\
&+ f_R\gamma A_{x,y}\int\limits_0^{\infty} |A_{y,x}(T-T^{'})|^2 a(T^{'})dT^{'} \\
&+ \frac{1}{2}f_R A_{y,x}\int\limits_0^{\infty} A_{x,y}(T-T^{'})A^{*}_{y,x}(T-T^{'})b(T^{'})dT^{'} \\
&+ \frac{1}{3}(1-f_R)\gamma\exp(i\sigma_i z)A^{*}_{x,y}A^{2}_{y,x} \\
&+ \frac{1}{2}f_R\gamma A_{y,x}\exp(i\sigma_i z)\int\limits_0^{\infty} A^{*}_{x,y}(T-T^{'})A_{y,x}(T-T^{'})b(T^{'})dT^{'} \qquad (6.52)
\end{aligned}$$

In this equations, $a(T^{'})$ and $b(T^{'})$ are components of the Raman response functions whose Fourier transforms describes the spectral dependencies of the components of the nonlinear nuclear Raman susceptibility tensor in the fused silica (interested readers can refer to reference [177] for more details). The circularly polarization electric field is related to the linear polarization electric field by Eqn. 6.49. The first two terms on the right hand side of Eqn. 6.52 represents SPM and XPM, respectively. The third, fourth, fifth and seventh terms on the right hand side represents Raman terms while the sixth term is the vector FWM. Observing Eqn. 6.52, it is not hard to realize the complexity of using it to numerically model the nonlinear terms for supercontinuum generation.

The natural coordinate to describe linear propagation in elliptical core or uniaxially asymmetric PCF is a linear basis for the field components E_x and E_y along the x and y axis. But other basis can be used to describe the linear propagation, for instance, $\pm 45^o$ or right-left circular basis.

Although this will introduce a coupling term since these are not linear eigen-basis. The right-left circular basis is especially useful for nonlinear propagation since it eliminates the phase-dependent FWM term. Hence the coupled GNLSE in Eqn. 6.22 is expressed in a circular basis where the nonlinear terms decouple, although this then gives coupling due to the linear birefringence.

We model the coupled GNLSE using a vectorized symmetric split-step Fourier method which was introduced in the previous section. As shown in Figure 6.6, we solve the dispersion (linear) propagation step in the linear polarization basis $A_{x,y}(f)$ to diagonalize the Fourier evolution operator, and it is propagated in the Fourier space. Then we perform Fourier transform to obtain temporal field $A_{x,y}(t)$ and then transform it into a circular polarization basis $A_{\pm}(t)$ for the nonlinear propagation step. The nonlinear step is propagated in real space, while the causal Raman response convolution integral is performed with an additional temporal Fourier transform of the intensities of the circular basis field components. The temporal derivative of the nonlinear source (optical shock) is evaluated using a centered finite difference in time. After the nonlinear propagation step, the field is transformed back to linear basis $A_{x,y}(t)$. Another Fourier transform is performed on $A_{x,y}(t)$ to obtain $A_{x,y}(f)$ for the dispersion propagation step, and then the loop continues for each z propagation step using the split-step Fourier method until the end of the propagation in z.

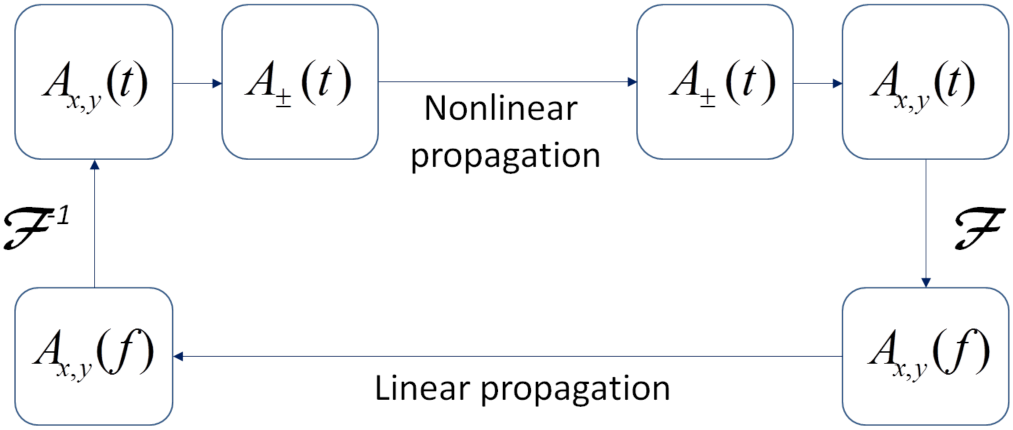

Figure 6.6: Numerical algorithm for solving the coupled-GNLSE by switching the polarization basis.

To avoid numerical instabilities, we check the convergence of the simulation by decreasing the step size of the propagation distance and the temporal and frequency sampling interval until no further changes occurred. At 2^{15} temporal and samples over a $T = 32$ ps simulation window separated by $\Delta t = 1$ fs and $\Delta z = 40$ μm spatial step size, we found the simulation reliably reaches a stable solution. The numerical simulation results using the polarization eigen-basis switching and split-step Fourier method will be discussed in the following chapter for both linear and circular birefringent PCF for both linear and elliptical input states of polarization.

In summary, the conventional approach of using scalar GNLSE becomes invalid for investigating polarization dynamics of supercontinuum generation. In this chapter, the detailed theoretical derivations of supercontinuum generation and the numerical simulation algorithm using vectorized GNLSE for understanding the polarization dynamics of supercontinuum generation were described. In particular, to more accurately model the Raman response function in supercontinuum generation, the recent Lin and Agrawal model considering the anisotropic nature of the Raman scattering effect were compared with the traditional single Lorentzian and the 13-peaks model and were chosen to be included in the numerical model. To effectively simulate the coupled GNLSE, an eigen-polarization basis switching technique was developed. The numerical simulation results represented with Poincaré sphere and new insights will be analyzed and discussed in detail for both linear and elliptical states of input polarization in the following chapter.

Chapter 7

Analysis and Poincaré sphere representations of the polarization dynamics for supercontinuum light source

7.1 Numerical modeling results for polarization instability of supercontinuum generation

The evolution of the state of polarizations of the ejected Raman soliton as representated on the Poincaré sphere is affected by both nonlinear and linear polarization rotations on the Poincaré sphere. The polarization dynamics reveal the presence of a polarization separatrix and the emergence of stable slow and unstable fast eigen polarizations for the Raman solitons ejected in the supercontinuum generation process. As far as we know, this is the first time polarization separatrix was numerically demonstrated for supercontinuum generation in a linearly birefringent photonic crystal fiber. Circularly birefringent fiber is investigated and found to simplify the nonlinear polarization dynamics, which will be discussed in detail in this chapter.

7.1.1 Soliton fission input and output states of polarization representation on the Poincaré sphere

A linearly polarized 100 fs chirp-free Sech pulse with 10 kW peak power is launched into the anomalous-dispersion region of the PCF. This high power input pulse corresponds to a 13th order soliton. The log-scale temporal and spectral evolutions of the SC process for fiber birefringence $B = 1 \times 10^{-5}$ and input polarization angle $\theta = 45°$ (to the slow axis) are plotted in Figure 7.2(a) and 7.2(f), showing the x and y eigen-polarization components separately as well as the total power.

Initially, the input field experiences pulse compression and spectral broadening due to self-phase modulation (SPM). The compressed pulse reaches a maximum peak power at around 1.7 cm, which agrees with the fission length calculation $L_{fiss} = L_D/N = 1.7$ cm [178], where the dispersion length $L_D = {T_{FWHM}}^2/3.11|\beta_2|$ for Sech input pulse. Beyond this distance, due to nonlinear effects such as Raman induced-frequency shift (RISF), self-steepening (SS), and linear effects such as third-order dispersion (TOD), the higher order soliton experiences soliton fission and breaks up into dispersive waves and multiple fundamental soliton-like pulses with varying peak powers and temporal widths (see Figure 7.2(g), which shows a zoomed-in of Figure 7.2(c)). From Figure 7.2(a) and 7.2(b) and Figure 7.2(d) and 7.2(e), we notice the x and y polarization components periodically couple and form a bound pair, i.e. exhibit soliton trapping, as they propagate in the PCF. Soliton trapping owes its existence to cross-phase modulation (XPM), represented by the last term on the right side of Eqn.6.48. The XPM-induced coupling between the x and y polarized solitons propagate at a common group velocity [133].

Soliton fission plays a critical role in higher order soliton SC [157, 20]. When soliton fission occurs (Figure 7.2(g)), multiple pulses are ejected and they form a bundle of interacting and interfering soliton components, except the shortest ejected pulse(s) which collides with the bundle of pulses, escapes with nearly half the total energy, and travels away from the main pulse as it slowly shifts toward a longer wavelength. This complex fission mechanism related to TOD was recently analogized to Newton's Cradle [179]. After the fission finishes (indicated by the dotted line in Figure 7.2(g)), the ejected soliton pulses shed excess energies to evolve into fundamental Raman solitons as they travel more slowly than the input pulse in the group velocity frame and simultaneously shift to longer wavelengths as a result of RISF. The direction of pulse energy transport is determined by the sign of TOD. Since the TOD is positive in this simulation, it results in a long wavelength shift of energy.

The soliton ejected earliest has the shortest temporal width, highest peak power and and the largest group velocity difference relative to the pump pulse and the computational group velocity frame. This first Raman soliton is responsible for the most spectral shift (indicated by black arrows

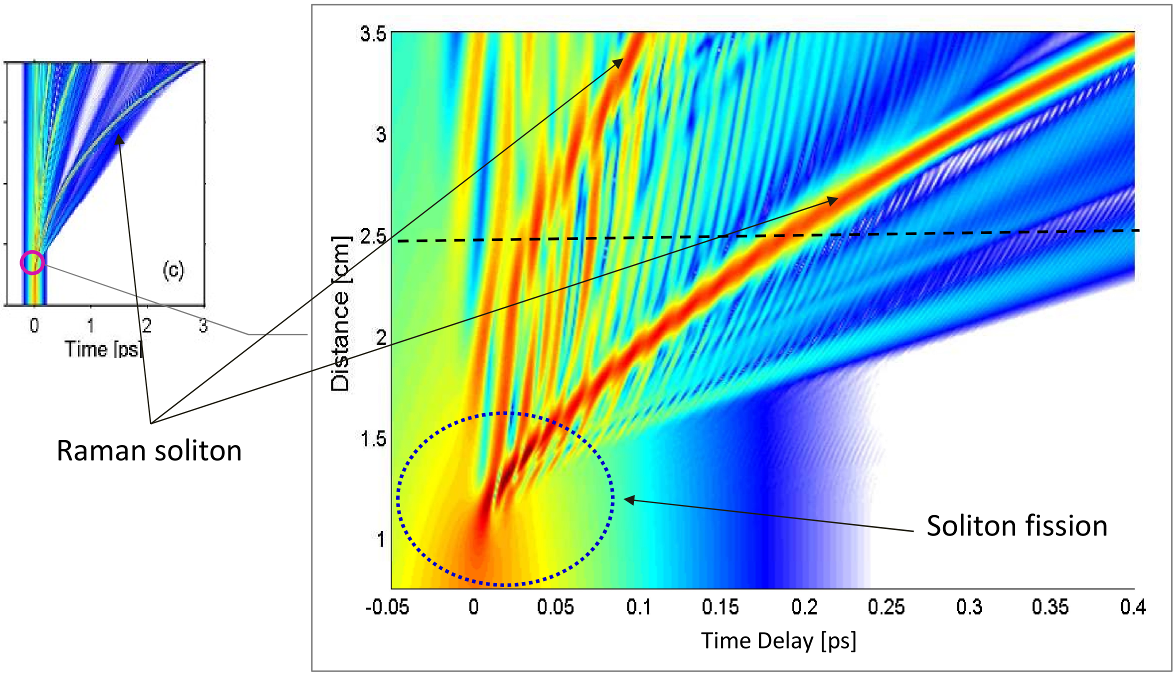

Figure 7.1: Soliton fission and Raman soliton ejected during the fission process. The dotted black line indicates the beginning of our analysis of the polarization dynamics of the ejected Raman soliton. The insect is the detailed zoomed-in temporal evolution of soliton fission process.

in Figure 7.3) and energy transfer to the long wavelength regime. Its SOP evolves as a unit upon propagation in the fiber [144]. Successive solitons can escape the bundle of interacting pulses depending on conditions such as fiber length and input power. As shown in Fig. 7.3, as the input polarization angle changes, the center of the soliton spectrum (indicated by arrows) at the end of the 8 cm fiber shifts too.

We investigate the SOP after soliton fission at a distance of $z = 2.4$ cm shown as dotted black line in Fig. 7.2(g)) and plot them on the Poincaré sphere as a function for various input polarizations and fiber birefringence. The results are shown in Fig. 7.4 for $B = 1 \times 10^{-8}$, 1×10^{-5}, 2.5×10^{-5} and 5×10^{-4}, respectively. $B = 1 \times 10^{-8}$ is the isotropic case, $B = 1 \times 10^{-5}$ is a typical value for a weakly birefringent PCF used in the literature, and $B = 5 \times 10^{-4}$ is a typical value for a highly birefringent commercial PCF. $B = 2.5 \times 10^{-5}$ corresponds to the intermediate case where

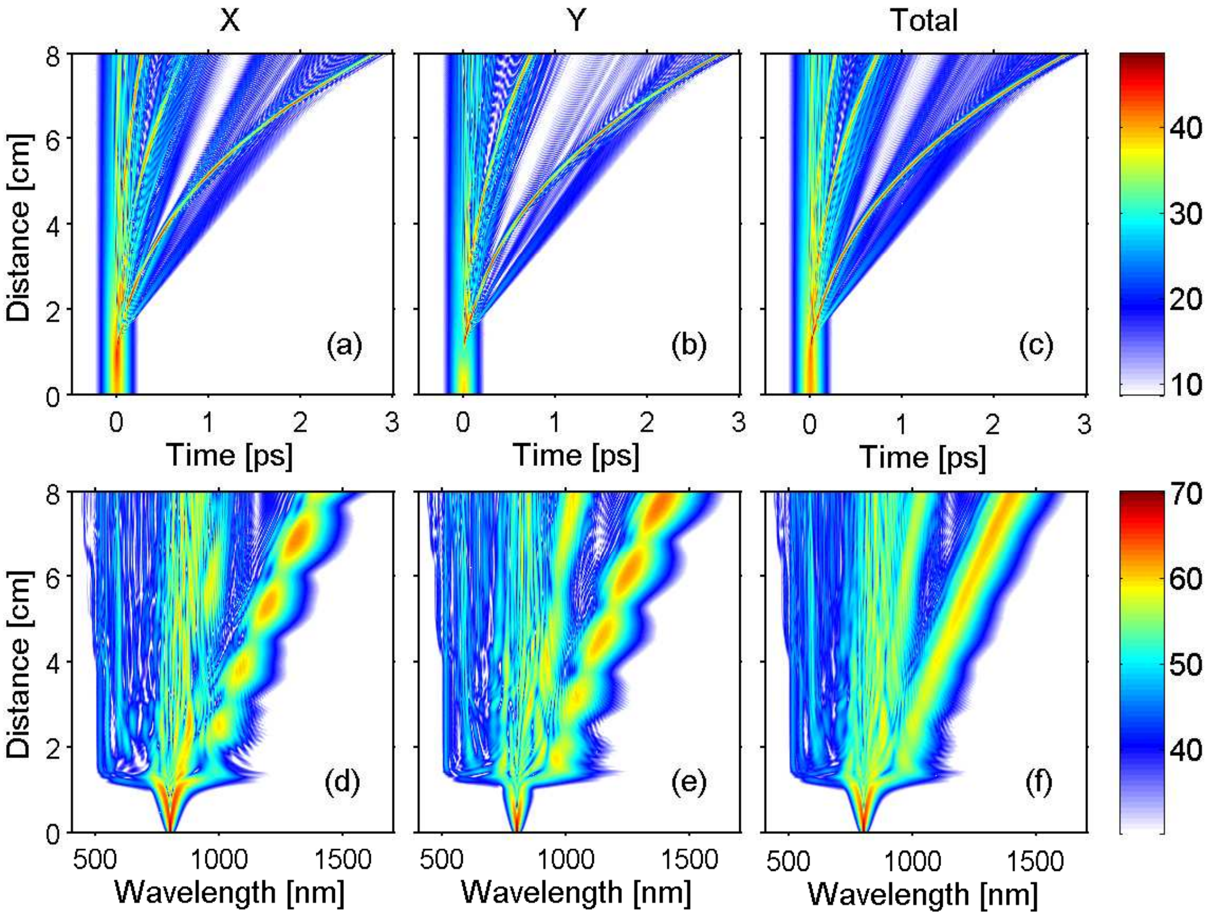

Figure 7.2: (a) to (f) Temporal and spectral evolutions of supercontinuum generation in PCF for $B = 1\times10^{-5}$ for linear input polarization with $\theta = 45°$: (a) to (c) are log-scale and color coded x, y and total temporal intensities, respectively; (d) to (f) are log-scale x, y and total power spectrums, respectively, color bars are in dB scale.

the ejected Raman soliton is near the polarization instability critical power and the polarization dynamics are most clearly revealed on the Poincaré sphere.

In the linear regime, the SOP of a monochromatic beam evolves as a rotation about the x-y axis on the Poincaré sphere periodically with a period equal to the beat length for $\lambda = 800$ nm, $L_B = \lambda/B = 80$ m, 8 cm, 3.17 mm and 1.6 mm, respectively. The input polarizations used in these simulations are linear (Fig. 7.4(a)) and elliptical (Figure 7.4(f)), spanning from 0° to ± 90° in ±5° steps.

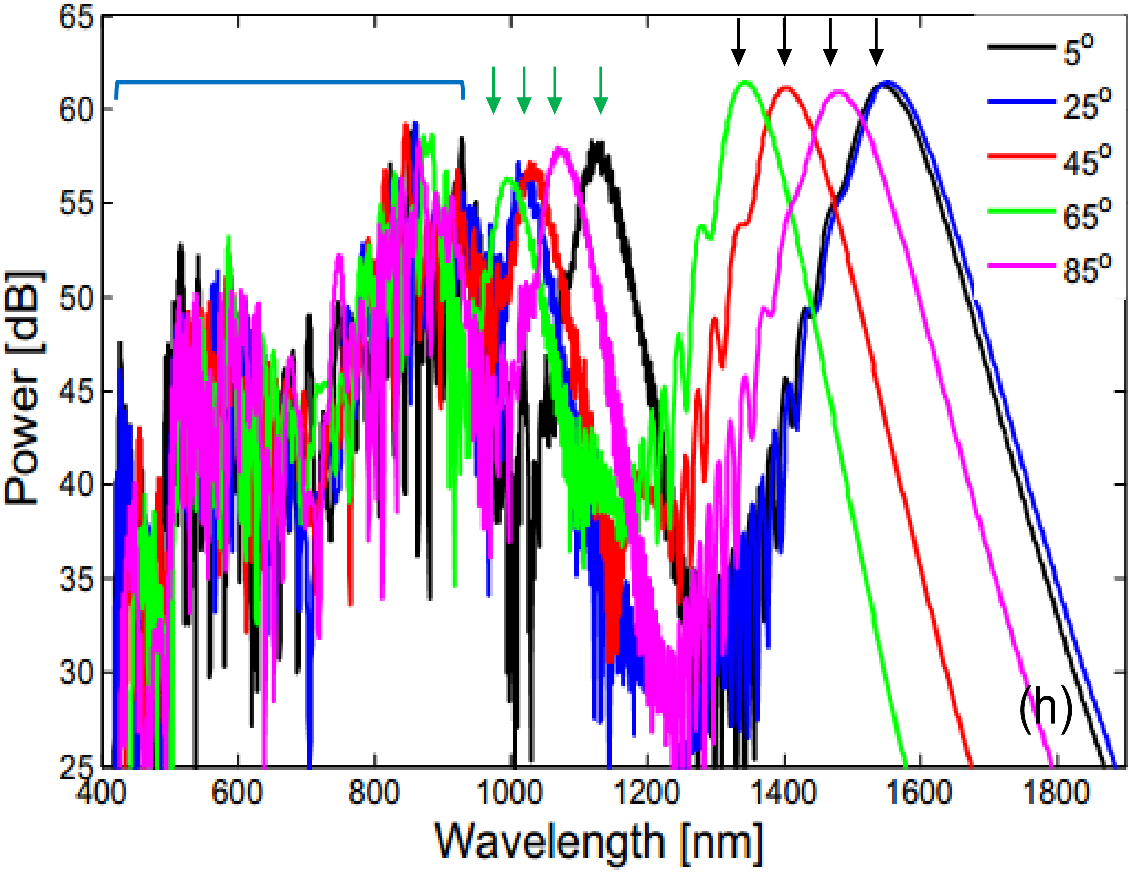

Figure 7.3: Simulated spectra of supercontinuum generation at the output of 8 cm long PCF with birefringence $B = 1 \times 10^{-5}$, for varying linear input polarization with $\theta = 5°$, $25°$, $45°$, $65°$ and $85°$. The blue horizontal bracket represent short wavelength region of dispersive waves, and the arrows point toward the first Raman solitons (black arrows) and second Raman solitons (green arrows).

A PI critical power $P_{cr} = 3\pi B/\lambda\gamma$ was predicted for CW light in nonlinear birefringent fiber using the Stokes parameters and the nonlinear dynamics on the Poincaré sphere [142]. Averaging the nonlinearity across the hyperbolic secant profile gives an additional numerical factor of 4.5 for nonlinear Schrödinger equations [143] which can be used to estimate the critical power for Raman solitons in PCF. We simulated Raman soliton polarization dynamics for several fiber birefringence between $B = 1 \times 10^{-8}$ and $B = 5 \times 10^{-4}$ and presented them on the Poincaré sphere. In particular, we used $B = 1 \times 10^{-5}$ and $B = 2.5 \times 10^{-5}$, where the ejected Raman soliton exceeds the critical power.

The SOPs of the ejected Raman soliton vary as the birefringence B increases as shown in Figure 7.4 (b) to 7.4(e) for linear input SOP (Figure 7.4(a)). Note that the different colors simply encode the different input SOP.

At low B (Figure 7.4(b)), the Raman soliton SOP remains the same as the input SOP, since for these linear inputs, nonlinear polarization rotation, also known as self-induced ellipse rotation [142, 133], leaves the SOP fixed on the equator.

As the fiber birefringence B is increased (Figure 7.4(c) and 7.4(d)), the soliton fission SOP is governed by both linear and nonlinear polarization rotations. A cluster of soliton fission SOPs appear around the slow-axis ($+s_1$-axis) close to the equator, so this represents an attraction of the polarization dynamics. In contrast, the soliton fission SOP are repelled away from the fast-axis ($-s_1$-axis). For low birefringence, some soliton fission SOPs appear at the $+s_3$ and $-s_3$-axis, depending on the sign of input SOP angle θ.

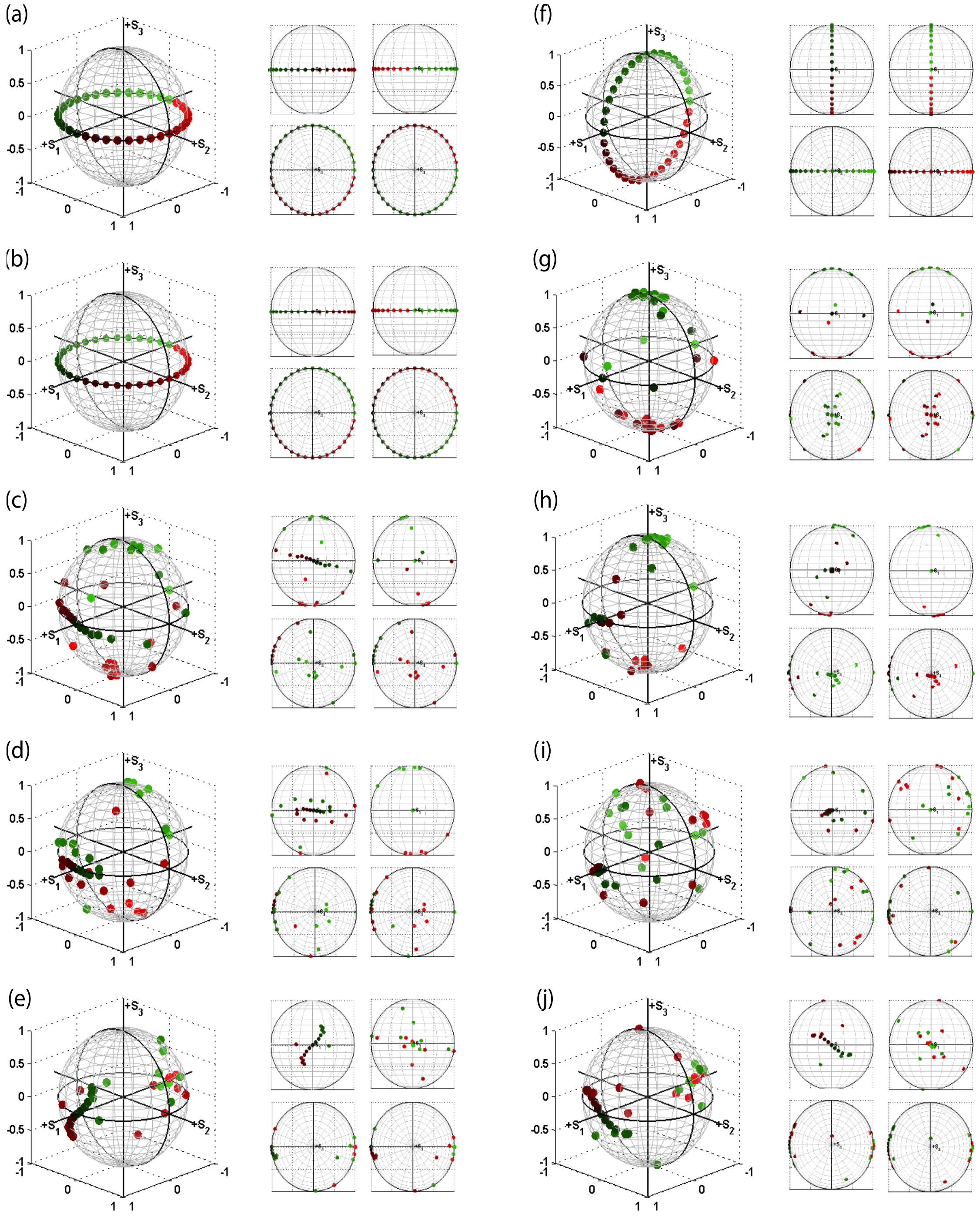

Figure 7.4: Poincaré sphere representations of the ejected Raman soliton SOP after soliton fission at a distance of $z = 2.4$ cm as a function of fiber birefringence and input polarizations. Input SOPs: (a) Linear and (f) Elliptical. Ejected Raman soliton pulse polarizations: (b) to (e) and (g) to (j) are for the linear and elliptical input SOP, respectively. $B = 1 \times 10^{-8}$ for (b) and (g), 1×10^{-5} for (c) and (h), 2.5×10^{-5} for (d) and (i), and 5×10^{-4} for (e) and (j). The 3D Poincaré sphere is supplemented with front and back views along the s_1-axis (slow $= x$ and fast $= y$), and top and bottom views along the s_3-axis (RHC and LHC).

For B $= 2.5\times10^{-5}$ (Figure 7.4(d)), the fast-axis instability at the back of the sphere is clearer, and we see an attraction of the ejected soliton SOP around the slow-axis at the front of the sphere. For high B $= 5 \times 10^{-4}$ (Figure 7.4(e)), the critical power is well in excess of the ejected Raman solitons and linear polarization rotation dominates, although polarizations are clearly clustered into a spiral around $+s_1$-axis they also cluster at $-s_1$-axis.

For elliptical input SOPs (Figure 7.4(f)), the output SOPs (Figs. 7.4(g) to 7.4(j)) are different from the linear case especially for low B (Figure 7.4(g)), because for B $= 1\times10^{-8}$, the majority of the soliton fission output SOPs are attracted to the poles (i.e. RHC and LHC states) instead of being fixed on the equator (Figure 7.4(b)). In Figure 7.4(i), B $= 2.5\times10^{-5}$, the SOPs disperse around the back of the sphere. Comparing with the linear case (Figure 7.4(d)), the clustering around the slow-axis is less pronounced. However, at high B (Figure 7.4(j)), the clustering around the slow and fast axis appear again, indicating linear polarization rotation dominance similar to the linear case of Figure 7.4(d).

7.1.2 Raman soliton input and output states of polarization representation on Poincaré sphere

In the previous section, we discussed the SOP of the ejected Raman soliton at $z = 2.4$ cm after soliton fission in SC from low to high linear birefringence, for linear and elliptical input SOPs. When soliton fission occurs, as shown in Figure 7.2(g), the first Raman soliton collides with the remaining bundle of solitons, escapes and transforms itself into a fundamental soliton by shedding excess energy as it propagates away from the main pulse and shifts toward longer wavelength. We now investigate how the SOP of this Raman soliton develops as it propagates down the fiber and how the different fiber birefringence and input SOP influence the evolution of the SOP of Raman soliton.

To investigate this, we locate the Raman soliton trajectory and fit it to an analytic polynomial function. Then we calculate the Stokes parameter $[S_0, S_1, S_2, S_3]$ at each time sample across the width of the Raman soliton and average these values across the temporal width of the soliton. If

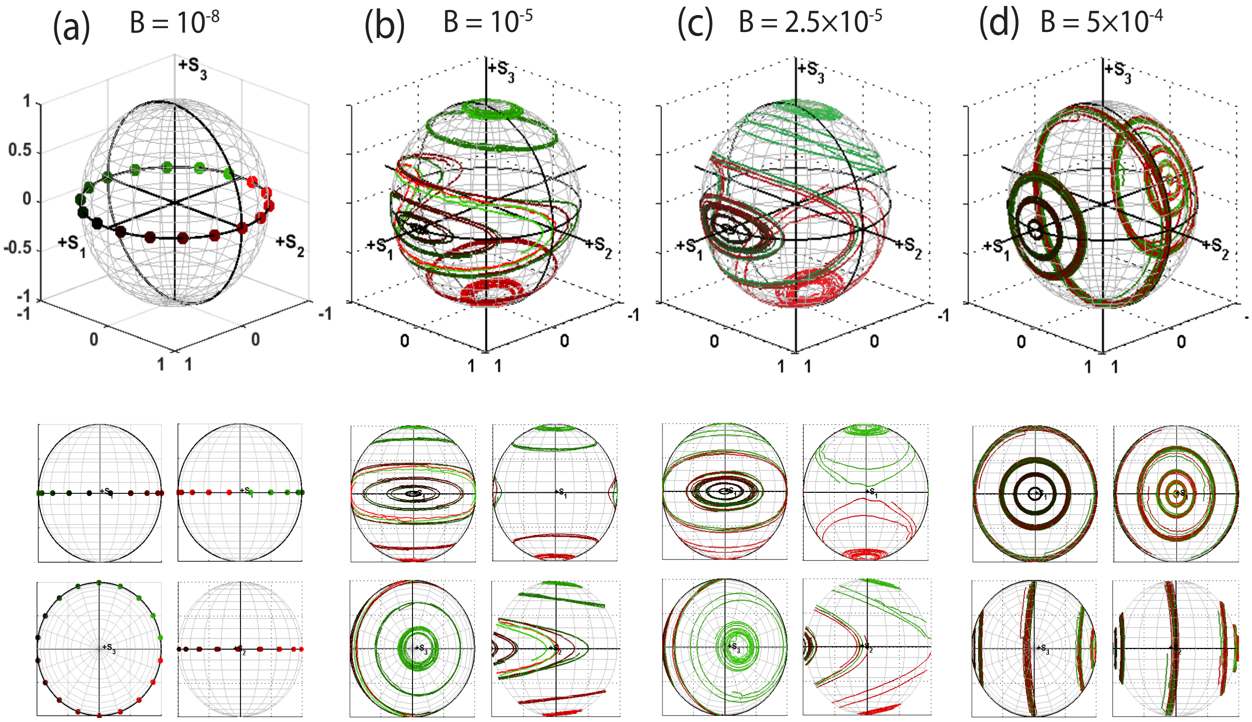

Figure 7.5: Poincaré sphere representations of the polarization evolution of the first ejected Raman soliton. (a) to (d) and (e) to (h) are polarization evolutions for linear and elliptical polarizations inputs to the PCF for SC generation, respectively. Birefringence $B = 1 \times 10^{-8}$ for (a) and (e), 1×10^{-5} for (b) and (f), 2.5×10^{-5} for (c) and (g) and 5×10^{-4} for (d) and (h). For these plots in addition to the 3D Poincaré sphere view, additional front and back views along $+s_1$-axis (slow $= x$) and -s_1-axis (fast $= y$) are shown, as well as top and side views along along $+s_3$-axis and $+s_2$-axis.

the polarization would vary across the temporal profile of the Raman soliton, then this would result in a depolarization since $\sqrt{{S_1}^2 + {S_2}^2 + {S_3}^2}$ would be less than S_0. However, we found that this was not the case and the entire Raman soliton would have a consistent polarization that would evolve as it propagate and would remain on the surface of the Poincaré sphere, with a degree of polarization DOP ≈ 1. The polarization dynamics are then represented as trajectories on the surface of the Poincaré sphere parameterized by the propagation distance. In Figure 7.5, we plot the SOP of the Raman soliton for both linear and elliptical SOP for θ spanning from $\pm 5°$ to $\pm$ 85° in $\pm 10°$ steps coded with the same colors used in Figs. 7.4 (a) and 7.4(f).

First, for the case of very low B and linear input SOP (Figure 7.5(a)), the evolution of Raman soliton SOP remains the same as input SOP due to vanishing nonlinear angular rotation on the equator. Therefore, for an almost isotropic fiber with high input intensity, the SOP of the Raman soliton is predictable for the entire length of propagation. Although, such a simple polarization evolution would be perturbed by random birefringence variations along the fiber length or the inclusion of quantum noise in the evolution equations.

However, with elliptical input SOP ((Figure 7.5(e)), since both x and y polarization components are excited, the trajectories of the SOP are seen to rotate around s_3-axis nonlinearly with speeds determined by the ellipticities that result from soliton fission ((Figure 7.4(g)). The rotation on the Poincaré sphere due to ellipse rotation is proportional to $S_3 = sin(2\chi)$ and the speed is maximized when $\chi = 22.5°$, half-way between the s_3-axis and the s_1-s_2 plane, and then decreases as the ellipticity of SOP moves toward more circular or more linear. The directions of rotation on the northern and southern hemispheres are the opposite, agreeing with an earlier study on polarization dynamics in low birefringence tapered fiber with slightly elliptical input polarization [157]. Two fixed points of nonlinear rotation in this case are RHC and LHC, i.e. the north and south poles of the s_3-axis.

For B $= 1 \times 10^{-5}$ (Figs. 7.5(b) and 7.5(f)), polarizations in the vicinity of the slow-axis rotate around the slow-axis ($+s_1$) in elliptical trajectories, which is a signature of a mixed state of linear and nonlinear polarization rotations [142]. As light intensity increases, nonlinear birefringence is induced because of the intensity-dependent refractive index. Asymmetry between the slow-and fast-axis arises when the induced nonlinear birefringence becomes comparable with the fiber intrinsic birefringence B. Furthermore, because for the slow-axis, the induced nonlinear birefringence adds to the intrinsic birefringence B, the slow-axis remains stable for input SOP close to it. On the other hand, along the fast-axis, because the induced birefringence reduces the intrinsic birefringence, as a result, the fast-axis becomes less stable. Interestingly, from the top views, the center of rotation for nonlinear ellipse rotation around the poles of the sphere are shifted toward the fast-axis, indicating formation of new nonlinear elliptical eigen-polarizations.

For $B = 2.5\times10^{-5}$, the induced nonlinear birefringence is comparable to the linear intrinsic birefringence, the effective beat length can become infinite for some states of polarization [133], and the polarization instability is most clearly revealed. The shift of the center of the nonlinear eigen-axis of rotation is evident and a new elliptical axis of nonlinear rotation is formed. The trajectories for the Raman soliton on the sphere is separated into three regions, one rotates around the stable slow-axis, two around the stable elliptical axis near the top and bottom of the sphere and a figure 8 separatrix crosses through the unstable fast axis. The number of fixed centers of rotation points is 3 in this case. For elliptical input SOPs (Figure 7.5(g)), the separatrix is revealed by the nearby trajectories.

For high B (Figs. 7.5(d) and 7.5(h)), the ejected Raman soliton is below the critical power for polarization instability, the polarization trajectories rotate around the stable slow and fast axis because linear polarization rotation around $+s_1$-axis dominates over the nonlinear ellipse rotation around $+s_3$-axis. The SOP trajectories rotate around the fast and slow axis in upright circles due to the dominance of linear birefringence over nonlinear rotation with only a slight nonlinear curvature seen from the side view. The number of fixed points (e.g. centers of rotation) change from three to two.

High linear birefringence can be used to suppress the unintentional birefringence or nonlinear polarization effects, and perhaps residual depolarization [10], when the incident polarization is aligned to the slow or fast-axis of the fiber. On the other hand, however, as shown in Figure 7.5(a), in the low birefringence case, the output SOPs are fixed on the equator remaining exactly the same as input SOPs. This tells us that with an isotropic fiber, with high input power, linear SOP of soliton fission and Raman soliton is predictable and controllable over the entire length of nonlinear propagation. But residual birefringence variations along the fiber would destroy this simple picture. Random birefringence could be included in the model to simulate the polarization dynamics for propagation in a long fiber.

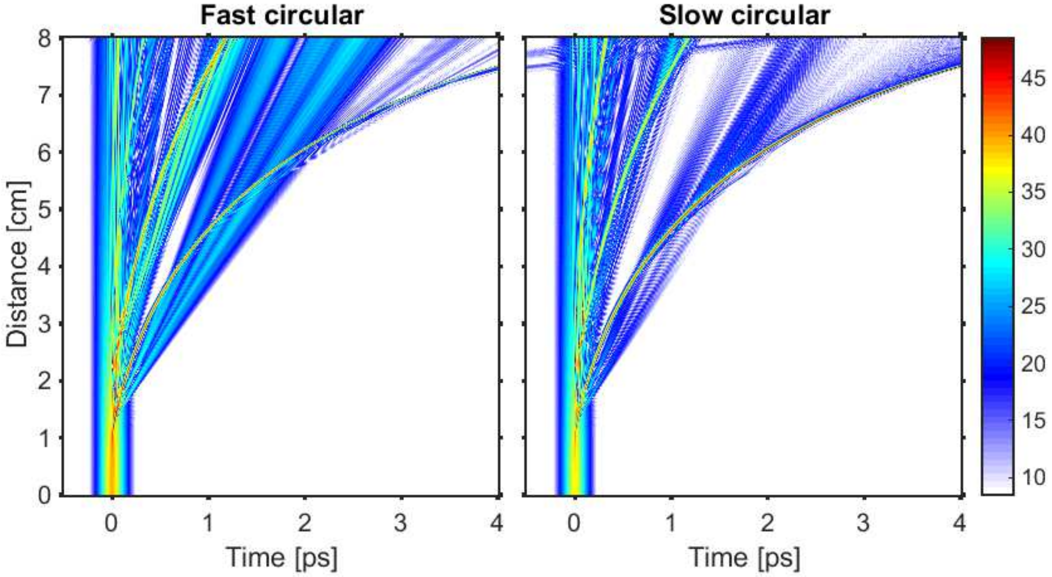

Figure 7.6: Temporal evolution of supercontinuum generation in circularly birefringent PCF for $B_c = 10^{-5}$ in log-scale showing the fast and slow components, for the case of a linear input polarization with $\theta = 45°$. Note that the slow component gains power as it propagates.

7.1.3 Raman soliton polarization evolution in circularly birefringent PCF

The complex polarization evolution of the Raman solitons ejected during the SC process in birefringent fiber and the resulting polarization instability can be interpreted on the Poincaré sphere as the interplay between linear rotations around the $+s_1$-axis and nonlinear rotations proportional to S_3 around the $+s_3$-axis. The interplay of these orthogonal rotations on the Poincaré sphere depend on the power and polarization of the Raman soliton ejected from the SC process. This dynamic process could simplified if instead the linear rotations also occur around the s_3-axis. This would be the case for circularly birefringent fiber, which can be produced by twisting the fiber as it is drawn [180]. We are thus motivated to simulate the SC process and the evolution of the polarization of the ejected Raman soliton for circularly birefringent fiber.

We simulated the SC process and the polarization dynamics of Raman solitons in a circularly birefringent PCF using coupled GNLSE for both the linear and elliptical input SOP used in the

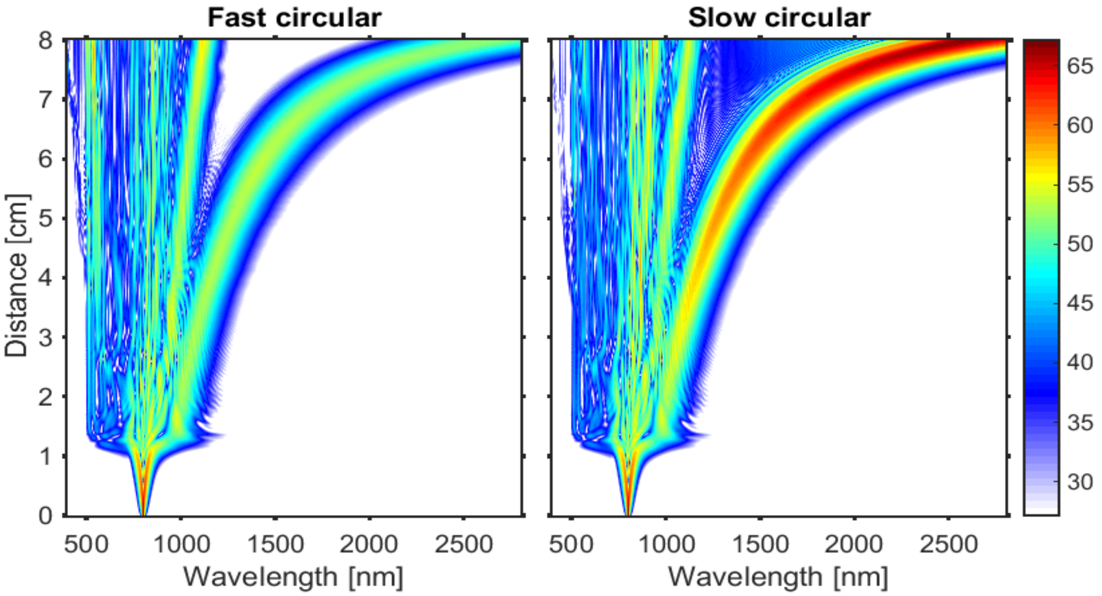

Figure 7.7: Spectral evolution of supercontinuum generation in circularly birefringent PCF for $B_c = 10^{-5}$ in log-scale for fast and slow components, for the case of linear input polarization with $\theta = 45°$.

linear birefringent fiber simulation. We define circular birefringence $B_c = n_s - n_f$, where n_s and n_f are the refractive indices for the slow and fast eigen-polarization components, respectively. For the circularly birefringent PCF case, instead of using $\Delta\beta_1 = \beta_{1x} - \beta_{1y}$ in Eq.6.48, we use $\Delta\beta_1 = \beta_{1s} - \beta_{1f}$ to represent the group velocity mismatch between slow and fast circular eigen-polarization components, where $\beta_{1s} = \epsilon n_s/c$, $\beta_{1f} = \epsilon n_f/c$ and $\epsilon = 1$ assuming equal slope between $\beta_s(\omega)$ and $\beta_f(\omega)$ as discussed in Section 2. The decoupling of the linear propagation of the circular eigen-polarization components and the phase-independent nonlinear terms implies that $\Delta\beta_0$ does not affect the propagation, so it is set to zero. Hence, the fourth term in Eq.6.48 becomes $i(\frac{\Delta\beta_1}{2}\frac{\partial}{\partial T})A_{\pm}$, while all the other terms remain the same.

We then numerically solved the circularly birefringent version of Eq.6.48 using a vector symmetric split-step Fourier method. In this case, both the dispersion and the nonlinear steps are performed in the circular basis. In Figure 7.6, the temporal evolution of both the slow and fast eigen-polarization component intensities are shown. The Raman soliton travels away from the main

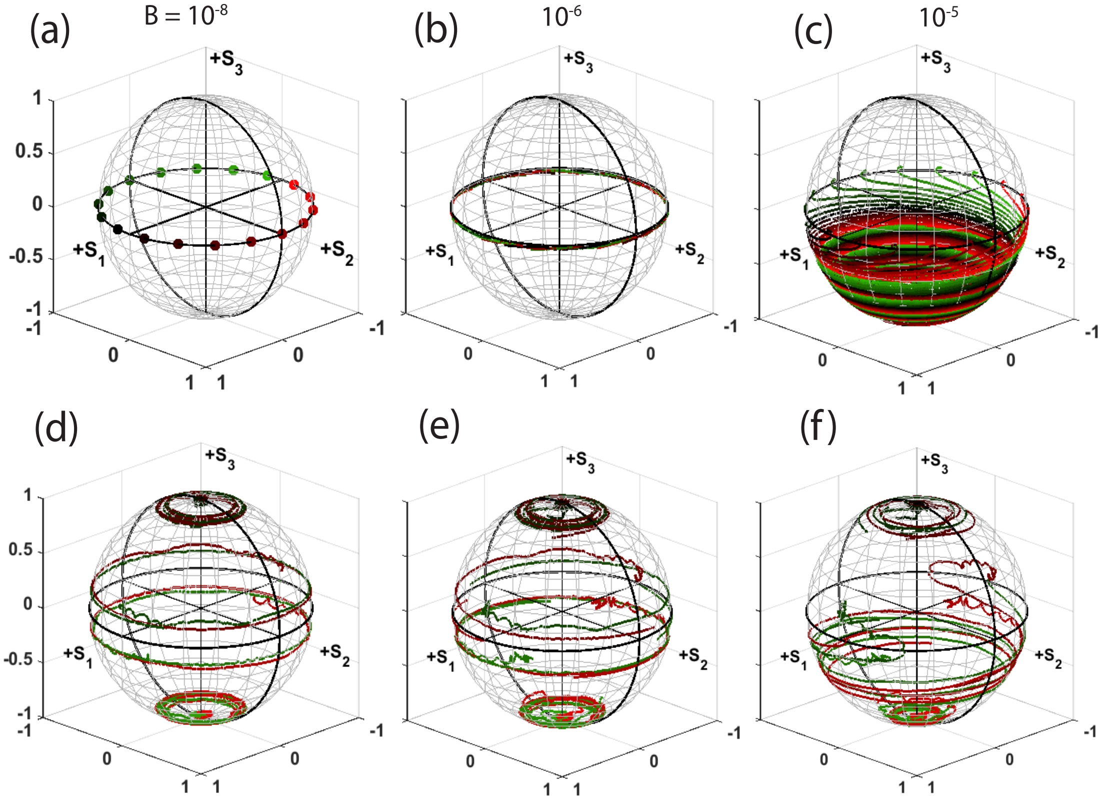

Figure 7.8: Poincaré sphere representations of Raman soliton polarization evolution for a circularly birefringent PCF. (a) to (c) and (d) to (f) are the polarization evolutions for the Raman soliton ejected during SC for linear and elliptical input polarizations, respectively. The fast circular component is at the north pole and the slow circular component is at the south pole. From (a) to (c) and (d) to (f), birefringence $B_c = 10^{-8}$, 10^{-6} and 10^{-5}, respectively.

pulse and is delayed even more than in the case of linear birefringence shown in Figure 7.2(a) and 7.2(b). The spectral evolution plots in Figure 7.7 show that the Raman soliton shifts toward an even longer wavelength compared to the linear birefringence PCF case in Figure 7.2(d) and 7.2(e). The appearance of a weak artifact at 7.5 cm due to slow circular wrapping around and becoming fast circular may be due to aliasing of the complex field.

The polarization dynamics of the ejected Raman solitons for various circular birefringence of $B_c = 10^{-8}$, 10^{-6} and 10^{-5} are represented on the Poincaré sphere in Fig. 7.8. The essentially isotropic case, $B_c = 10^{-8}$, is nearly identical to the isotropic linearly birefringent case, $B = 10^{-8}$, in Figure 7.5(e). Circularly birefringent PCF is not commercially available yet and twisting (either during fiber drawing or after) is likely to yield a small birefringence in the range of $B_c = 10^{-6}$ [180]. However, the interesting case of $B_c = 10^{-5}$ is also explored in our simulation since this leads to a beat length of $L_{beat} = 8$ cm, which is equal to our simulated fiber length. For linear input SOPs (Figs. 7.8 (a) to 7.8(c)), in the essentially isotropic case ($B_c = 10^{-8}$), the output SOPs of the Raman soliton are fixed on the equator similar to the linear birefringent PCF case (Figure 7.5(a)). However, as the circular birefringence is increased to 10^{-6}, we see the SOP of the Raman soliton rotates about the s_3-axis on the Poincaré sphere, in this case at a constant rate due to the circular birefringence. For $B = 10^{-5}$, the SOP of the Raman soliton rotates about s_3-axis and spirals toward the south pole, indicating a stable slow eigen-mode on the Poincaré sphere. Note that all the trajectories for the evolution of these linear polarizations are identical downward spirals on the Poincaré sphere converging towards the slow eigen-mode. Unlike the linear birefringent PCF case, the soliton fission process for the circularly birefringent fiber has not scrambled the SOP of the ejected Raman soliton.

Figures 7.8 (d) to 7.8(f) show the polarization evolution of the ejected Raman solitons for the various elliptically polarized Sech pulses injected into the fiber. We see purely nonlinear polarization rotation around the s_3-axis which is proportional to the S_3 stokes component of the ejected Raman soliton, which vanishes on the equator for the linear input SOP. However as the circular birefringence is increased ($B_c = 10^{-6}, 10^{-5}$), the output SOPs rotate around the s_3-axis and spiral downwards toward the slow eigen-mode. Notice that the rate that the spiral drifts downwards increase with increasing birefringence. The rotation rate around the $+s_3$-axis is different on the northern hemisphere where linear and nonlinear effects counteract, while on the southern hemisphere these two effects cooperate. The fast eigen-mode at the north pole of the Poincaré sphere is an unstable state since the trajectories spiral away from it.

In this chapter, we have explored the complex polarization dynamics of the Raman solitons ejected during supercontinuum generation in photonic crystal fibers (PCF) through representations of polarization trajectories on the Poincaré sphere. The theoretical background and numerical method for solving the generalized nonlinear Schrödinger equations (GNLSE) were introduced. An accurate model of Raman response function was studied and compared with the 13-peaks and the single Lorentzian model. We then use numerical vector beam propagation simulations of the coupled GNLSE which include all orders of dispersion, Kerr and delayed Raman nonlinearities and optical shock. The simulation utilized a dispersive linear step in the frequency domain in the fiber eigen-basis combined with a nonlinear step in the time domain using the circular basis, where the nonlinear terms simplify since the phase-dependent four-wave mixing term disappears. This allowed the calculation of the SC process for both linearly and circularly birefringent (e.g., twisted) PCF with varying birefringence.

Different states of linearly and elliptically polarized 100 fs Sech pulses were applied to the simulated PCF input to investigate the polarization of the ejected Raman soliton. We also studied the dynamics of its polarization evolution on the Poincaré sphere for various fiber birefringence. The Raman solitons were seen to have a nearly constant state of polarization across their temporal profile, with an averaged Stokes vector that remained on the surface of the Poincaré sphere and exhibited no depolarization during propagation.

For essentially isotropic PCF, the nonlinear ellipse rotation vanishes for linearly polarized inputs. In this case, the ejected Raman soliton remains linearly polarized, although this would be susceptible to perturbations caused by random birefringence variations along the fiber length. While for elliptical input polarizations, the ejected Raman soliton revealed nonlinear ellipse rotation about the s_3 axis of the Poincaré sphere in proportion to the ellipticity S_3. Highly linear birefringent fiber led to Raman solitons with various polarization evolutions dominated by linear polarization rotation about the s_1 axis on the Poincaré sphere. Intermediate linear birefringence leads to complicated interplay of these orthogonal rotations at which the nonlinear refractive index due to the ejected soliton is close to the fiber birefringence. On the Poincaré sphere, this polarization instability was manifested with the emergence of three stable polarization states (along $+s_1$ corresponding to the slow-axis and tilted slightly away from $\pm s_3$), a fast axis instability (along $-s_1$), and a polarization separatrix.

Circularly birefringent fiber, made by twisting during fiber drawing, will exhibit both linear rotations of the Poincaré sphere about s_3 and nonlinear rotation about s_3 proportional to S_3. In this case, it leads to a much simpler polarization evolution as pure rotations around s_3, however with a downward spiral on the Poincaré sphere away from the unstable fast circular eigenstate towards the stable slow circular eigenstate. This suggests that if twisted PCF can be fabricated with sufficient circular birefringence to dominate over unwanted linear birefringence induced by bendings or stress, it may lead to the most stable and repeatable single polarization output supercontinuum by launching the stable slow circular polarization into the twisted PCF. For optical imaging applications requiring a broadband single polarization, this could effectively double the available output power of the supercontinuum process as compared with unpolarized outputs often produced by the supercontinuum generated in a PCF.

Chapter 8

Thesis summary and Outlook

In my thesis, I described the experimental investigations and numerical simulations of a polarization dynamic broadband light source and polarization effects for polarimetry optical imaging in scattering medium. In the first part of the thesis, I presented my research from analysis of optical scattering using Mie and Rayleigh scattering matrix approach and the review of optical properties of scattering medium, to polarized light propagation in scattering medium. During the investigation of polarization imaging in scattering medium, I reviewed several polarimetry techniques using Stokes and Mueller matrix techniques. The polarization memory effect is particularly interesting and has not been thoroughly investigated yet for optical imaging in scattering medium. From the polarization-gated imaging study, I expanded the scattering matrix analytical models to compute the point spread functions for both polarization sum and difference imaging techniques based on prior investigations in the literature for both Mie and Rayleigh scatterers. I also investigated the depolarization of multiple-scattered light for linearly and circularly polarized incident light based on the Green's function approach derived previously for scattered light fields. To demonstrate the image quality improvement from the analytical results from the PSF scattering matrix and depolarizations, I conducted experiments to measure the optical scattering of a scattering phantom and then performed polarization difference imaging using the phantom. The results shows 11 times improved image contrast using polarization difference imaging in a highly scattering medium compared with polarization sum imaging for small particles in the Rayleigh regime using orthogonal linearly polarized light. The Stokes parameter theory is the tool that was used in the simulations for studying the polarization dynamics of the broadband light source for optical imaging in scattering medium.

In the second part of the thesis, I studied a dynamic structured illumination microscope aimed for Fourier synthesis optical imaging in scattering media using acousto-optically modulated traveling wave illumination to sample spatial Fourier components in the time domain using a single pixel for detection. This technique is an extension of the Doppler encoded excitation pattern (DEEP) microscope developed in our lab [78, 116]. This imaging technique was experimentally constructed based on moving illumination pattern generation from an acousto-optic deflector (AOD) controlled by a direct digital synthesizer and only requires a photodiode detector for Fourier domain imaging. A strobe-mode was developed in order to visualize the moving illumination pattern generation. The microscope was constructed based on interfering the two first-order diffracted laser beams from the AOD driven by a frequency chirp signal from the direct digital synthesizer (DDS). I developed a matched-filtering algorithm to extract the DEEP signal from the detector for an amplitude grating object and a grating reconstruction was shown to agree well with a conventional CCD image of the grating object. A polarization interferometric structured illumination microscope was also investigated using the 0^{th} and 1^{st} order diffracted beams from the birefringent and optically active TeO_2 Bragg cell. A few insights were gained from this experiment: the polarization of the input beam to the TeO_2 crystal can be optimized for the polarization switching process to enhance diffraction efficiency. In addition, the polarized illumination from the sinusoidal spatial fringes generated by the TeO_2 crystal has the capability to detect objects (especially birefringent objects) inside a scattering medium for high resolution Fourier domain imaging. Biologically tissue and tendon are known to be birefringent and can be imaged by the polarized dynamic structured illumination microscope. However, in order to image into scattering media using this Fourier basis structured illumination technique, a broadband laser source is required.

Therefore, in the third part of the thesis I investigated a broadband supercontinuum light source for optical imaging in scattering medium both experimentally and theoretically. I demonstrated a high power and ultra-broadband supercontinuum laser source using dispersion-compensated

Ti:Sapphire laser pulses and a highly nonlinear photonic crystal fiber (PCF). In this experiment, I demonstrated a polarization-controlled octave-spanning supercontinuum light source and the results were theoretically investigated in details. During the experiment, the supercontinuum spectrum was observed to depend on the input polarization to the photonic crystal fiber and this provided a motivation for further numerical simulation work to study the behavior using detailed numerical simulation and to investigate the polarization dynamics of Raman solitary-waves generated by the supercontinuum process. The complex polarization dynamics of supercontinuum generation was explored by simulating the generalized vector nonlinear Schrödinger equations (GNLSE) for both isotropic and polarization maintaining with inputs of both linear and elliptical polarizations. To obtain the numerical data of the Raman solitary-wave as it red-shifts to longer wavelengths while propagating in the nonlinear fiber, I developed a numerical method to accurately track and extract the Raman solitary-wave spectrum from the supercontinuum simulation. This new extraction method enabled the numerical analysis of the polarization dynamics of the Raman solitary-wave in a complex supercontinuum generation for the first time. Then the Stokes parameters were calculated, and the polarization trajectories visualized on the Poincaré sphere revealed rich polarization dynamics including a polarization separatrix and fast axis instability. Furthermore, an eigen-polarization basis switching technique was developed to model the coupled GNLSE using the circular basis for the nonlinear propagation step and the linear basis for the dispersion step because the circular basis eliminates the phase-dependent four-wave mixing term.

Previous research works were focused on polarization evolutions in linearly birefringent fibers while the circularly birefringent PCF were neglected. In this work, polarization dynamics of supercontinuum generation in circularly birefringent fibers was also numerically investigated. For the circular birefringence case, a simplified polarization evolution of the ejected Raman solitary-wave was demonstrated that was unlike the complicated polarization dynamics in the linear birefringence case. This finding has potentials for optical imaging applications where a high output power and single circularly polarized broadband light source are required.

8.1 Summary of thesis contributions

My contributions for the investigations of polarization dynamic light source and polarization effects for optical imaging in a scattering medium can be summarized as the following,

- Theoretical investigations of optical properties of optical scattering medium in both Mie and Rayleigh scattering regimes using scattering probably functions derived from scattering matrix
- Theoretical investigations of image quality enhancement for polarization difference imaging for Mie and Rayleigh scattering based on scattering matrix approach from prior works
- Experimental demonstration of image contrast improvement of optical imaging in a highly scattering medium using polarization difference technique from orthogonally linearly polarizations in the Rayleigh scattering regime
- Experimental demonstration of polarization interferometric dynamics structured illumination microscope for optical Fourier domain imaging using single pixel detector and acousto-optically modulated illumination
- Experimentally demonstrated and theoretically developed a matched filtering algorithm for signal reconstruction in structured illumination Fourier domain imaging
- Experimentally demonstrated an optical delay line for repetition rate doubling using broadband dielectric mirrors for broadband polarization rotation of a supercontinuum light source
- Theoretical investigation of Raman response function by comparing the single Lorentzian, 13-peaks Hollenback and Lin and Agrawal models to accurately and efficiently simulate the supercontinum generation simulation based on coupled nonlinear Schrödinger equations
- Experimental demonstration of a polarization-controlled supercontinuum light source for optical imaging using ultrafast pulses generated from a Ti:Sapphire laser and a highly nonlinear photonics crystal fiber

- Theoretical demonstration of polarization dynamics of supercontinuum generation for various input state of polarizations for both isotropic and anisotropic fiber media using coupled nonlinear Schrödinger equations
- Theoretical demonstration of dynamic polarization trajectories and polarization separatrix of Raman soliton-like waves in supercontinuum generation using Poincaré sphere representations
- Theoretically demonstration of eigen-polarization basis-switch algorithm in the symmetric split-step Fourier method for solving the dispersion step and nonlinear step separately
- Theoretical demonstration of a slow mode circularly polarized tunable broadband light source that can be achieved through fiber twisting for a potentially stable cirsularly polarized light source for optical imaging applications

8.2 Future directions

My thesis work focused on theoretical and experimental investigations of optical imaging in scattering medium using polarization effects and a broadband supercontinuum light source. One finding of the research is the polarization difference imaging can improve image contrast in scattering media and it may have potentials for structured illumination optical imaging in scattering medium. In particular, if the polarization difference imaging is incorporated into the acousto-optically generated structured illumination imaging, it can not only enhance optical imaging contrast, but also enable detection of birefringent objects in a highly scattering environment. If the research in this direction can be continued, we could expect to see enhancement of optical imaging and sensing in biological tissues.

The coherence gating for optical imaging proposed previously motivated the experimental and numerical studies of the broadband supercontinuum light source. I investigated the supercontinuum laser based on bench top experiment using a photonic crystal fiber and a high repetition rate Ti:Sapphire laser. However, in recent years, other types of tapered and silicon waveguides are showing signed of promising octave-spanning supercontinuum for chip-scale integrated optical devices. My research in the polarization dynamic supercontinuum laser provides a useful tool for designing and modeling the polarization effects for such integrated supercontinuum laser device. The numerical model based on vectorized generalized nonlinear Schrödinger equations can be applied to model the dispersion parameters and nonlinearities not only for linear but also for circularly birefringent waveguides for various optical input powers. Furthermore, this polarimetric simulation calculating Stokes parameters can model all input and output states of polarizations of the waveguide and visualize the polarization evolution of any part of the light spectra along the waveguide through Poincaré sphere representations.

I also hope the theoretical investigations can shed insights and hence motivate a new type of stable circularly polarized broadband light source, because the research results presented in the later part of the thesis suggests if circularly birefringent photonic crystal fibers can be fabricated by twisting the fiber during the drawing process with sufficient circular birefringence to dominate random unwanted linear birefringence, it can lead to the most stable and repeatable single polarization supercontinuum output if the stable slow mode circular polarization is launched into the fiber. This potentially enables a new type of polarized, versatile and broadband light source for optical imaging in a scattering medium. To continue the investigation, the proposed light source can be realized in the experiment following a similar setup but with a circularly birefringent fiber medium. For practical applications, this circularly polarized fiber medium is not restricted to standard nonlinear photonic crystal fibers. As mentioned, it could potentially be made from crystals that can provide enough nonlinearity and dispersion engineering or by tapering the PCF to be made compact enough for integrated photonic chip optical imaging. The waveguide medium can be integrated with a compact laser source to generate circularly polarized broadband illumination with tunability and stability, which I envision would be an attractive light source for biomedical imaging, spectroscopy, polarization sensitive and multi-wavelength imaging in scattering medium.

Bibliography

[1] Eitan Edrei and Giuliano Scarcelli. Optical imaging through dynamic turbid media using the Fourier-domain shower-curtain effect. Optica, 3(1):71–74, jan 2016.

[2] S P Morgan, M P Khong, and M G Somekh. Effects of polarization state and scatterer concentration on optical imaging through scattering media. Applied optics, 36(7):1560–5, mar 1997.

[3] Mats G L Gustafsson. Nonlinear structured-illumination microscopy: wide-field fluorescence imaging with theoretically unlimited resolution. Proceedings of the National Academy of Sciences of the United States of America, 102(37):13081–6, sep 2005.

[4] Lihong V Wang and Hsin-i Wu. Biomedical optics: principles and imaging. John Wiley & Sons, 2012.

[5] Valery V. Tuchin. Polarized light interaction with tissues. Journal of Biomedical Optics, 21(7):071114, apr 2016.

[6] J. S. Tyo, M. P. Rowe, E. N. Pugh, and N. Engheta. Target detection in optically scattering media by polarization-difference imaging. Applied Optics, 35(11):1855, apr 1996.

[7] S G Demos and R R Alfano. Temporal gating in highly scattering media by the degree of optical polarization. Optics letters, 21(2):161–3, jan 1996.

[8] Demirhan Kobat, Michael E. Durst, Nozomi Nishimura, Angela W. Wong, Chris B. Schaffer, and Chris Xu. Deep tissue multiphoton microscopy using longer wavelength excitation. Optics Express, 17(16):13354, aug 2009.

[9] V. V. (Valerii Viktorovich) Tuchin and Society of Photo-optical Instrumentation Engineers. Tissue optics : light scattering methods and instruments for medical diagnosis.

[10] Haohua Tu, Yuan Liu, Xiaomin Liu, Dmitry Turchinovich, Jesper Lægsgaard, and Stephen A Boppart. Nonlinear polarization dynamics in a weakly birefringent all-normal dispersion photonic crystal fiber: toward a practical coherent fiber supercontinuum laser. Opt. Express, 20(2):1113–1128, 2012.

[11] Paras N. Prasad and John Wiley & Sons. Introduction to biophotonics. Wiley-Interscience, 2003.

[12] Jeff Hecht. Short history of laser development. Optical Engineering, 49(9):091002, sep 2010.

[13] D Huang, E. Swanson, C. Lin, J. Schuman, W. Stinson, W Chang, M. Hee, T Flotte, K Gregory, C. Puliafito, and al. Et. Optical coherence tomography. Science, 254(5035):1178–1181, nov 1991.

[14] Robert Hellwarth and Paul Christensen. Nonlinear optical microscopic examination of structure in polycrystalline ZnSe. Optics Communications, 12(3):318–322, nov 1974.

[15] Winfried Denk, James H Strickler, and Watt W Webb. Two-Photon Laser Scanning Fluorescence Microscopy. Source: Science, New Series, 248(4951):73–76, 1990.

[16] R. R. Alfano and S. L. Shapiro. Emission in the Region 4000 to 7000 Å Via Four-Photon Coupling in Glass. Physical Review Letters, 24(11):584–587, mar 1970.

[17] F. Silva, D.R. Austin, A. Thai, M. Baudisch, M. Hemmer, D. Faccio, A. Couairon, and J. Biegert. Multi-octave supercontinuum generation from mid-infrared filamentation in a bulk crystal. Nature Communications, 3:807, may 2012.

[18] Th. Udem, J. Reichert, T. W. Hänsch, and M. Kourogi. Accuracy of optical frequency comb generators and optical frequency interval divider chains. Optics Letters, 23(17):1387, sep 1998.

[19] David J. Jones, Scott A. Diddams, Jinendra K. Ranka, Andrew Stentz, Robert S. Windeler, John L. Hall, and Steven T. Cundiff. Carrier-Envelope Phase Control of Femtosecond Mode-Locked Lasers and Direct Optical Frequency Synthesis. Science, 288(5466), 2000.

[20] A V Husakou and J Herrmann. Supercontinuum generation of higher-order solitons by fission in photonic crystal fibers. Phys. Rev. Lett., 87(20):203901, 2001.

[21] Jinendra K Ranka, Robert S Windeler, and Andrew J Stentz. Visible continuum generation in air-silica microstructure optical fibers with anomalous dispersion at 800 nm. Optics letters, 25(1):25–27, 2000.

[22] Alexander Apolonski, Boris Povazay, Angelika Unterhuber, Wolfgang Drexler, William J Wadsworth, Jonathan C Knight, and Phillip St J Russell. Spectral shaping of supercontinuum in a cobweb photonic-crystal fiber with sub-20-fs pulses. J. Opt. Soc. Am. B, 19(9):2165–2170, 2002.

[23] Jonathan C Knight. Photonic crystal fibres. Nature, 424(6950):847–851, 2003.

[24] Valery V. Tuchin, Sergei R. Utz, and Ilya V. Yaroslavsky. Tissue optics, light distribution, and spectroscopy. Optical Engineering, 33(10):3178, oct 1994.

[25] Alfred Vogel and Vasan Venugopalan. Mechanisms of Pulsed Laser Ablation of Biological Tissues.

[26] J M Schmitt and G Kumar. Turbulent nature of refractive-index variations in biological tissue. Optics Letters, 21(16):1310, aug 1996.

[27] Craig F. Bohren and Donald R. Huffman, editors. Absorption and Scattering of Light by Small Particles. Wiley-VCH Verlag GmbH, Weinheim, Germany, apr 1998.

[28] L E Paramonov S. Ya. Sid'ko, V. N. Lopatin. Polarization Characteristics of Solutions of Biological Particles. Nauka, Novosibirsk, 1990.

[29] M.J.C. Van Gemert, S.L. Jacques, H.J.C.M. Sterenborg, and W.M. Star. Skin optics. IEEE Transactions on Biomedical Engineering, 36(12):1146–1154, 1989.

[30] Craig F. Bohren and Donald R. Huffman, editors. Absorption and Scattering of Light by Small Particles. Wiley-VCH Verlag GmbH, Weinheim, Germany, apr 1998.

[31] C Dunsby and P M W French. Techniques for depth-resolved imaging through turbid media including coherence-gated imaging. Journal of Physics D: Applied Physics, 36(14):R207–R227, jul 2003.

[32] Steven L Jacques. Optical properties of biological tissues: a review. Phys. Med. Biol. Phys. Med. Biol, 58(58):37–61, 2013.

[33] Julia L Sandell and Timothy C Zhu. A review of in-vivo optical properties of human tissues and its impact on PDT. Journal of biophotonics, 4(11-12):773–87, nov 2011.

[34] Frédéric Bevilacqua, Dominique Piguet, Pierre Marquet, Jeffrey D. Gross, Bruce J. Tromberg, and Christian Depeursinge. In vivo local determination of tissue optical properties: applications to human brain. Applied Optics, 38(22):4939, aug 1999.

[35] Frédéric Bevilacqua, Andrew J. Berger, Albert E. Cerussi, Dorota Jakubowski, and Bruce J. Tromberg. Broadband absorption spectroscopy in turbid media by combined frequency-domain and steady-state methods. Applied Optics, 39(34):6498, dec 2000.

[36] R. R. Anderson and J. A. Parrish. Optical Properties of Human Skin. In The Science of Photomedicine, pages 147–194. Springer US, Boston, MA, 1982.

[37] H. C. van de (Hendrik Christoffel) Hulst. Light scattering by small particles. Dover Publications, 1981.

[38] V. V. (Valerii Viktorovich) Tuchin, Lihong V. Wang, and Dmitry A. Zimnyakov. Optical polarization in biomedical applications. Springer, 2006.

[39] Max. Born. Principles of Optics. Elsevier Science, 1980.

[40] Christian Brosseau. Fundamentals of polarized light : a statistical optics approach. Wiley, 1998.

[41] R. M. A. Azzam and N. M. Bashara. Ellipsometry and polarized light. North-Holland, Amsterdam ;;New York, 1987.

[42] William A. Shurcliff. Polarized light. Harvard Univ Press, 2013.

[43] Christian Mätzler. Matlab functions for Mie scattering and Absorption V2 - _ MATLAB Functions. Technical report, 2002.

[44] J. Scott Tyo, Dennis L. Goldstein, David B. Chenault, and Joseph A. Shaw. Review of passive imaging polarimetry for remote sensing applications. Applied Optics, 45(22):5453, aug 2006.

[45] Uwe J. Meierhenrich, Wolfram H.-P. Thiemann, Bernard Barbier, André Brack, Christian Alcaraz, Laurent Nahon, and Ray Wolstencroft. Circular Polarization of Light by Planet Mercury and Enantiomorphism of its Surface Minerals. Origins of Life and Evolution of the Biosphere, 32(2):181–190, 2002.

[46] L. W. Bandermann, J. C. Kemp, and R. D. Wolstencroft. Circular Polarization of Light Scattered from Rough Surfaces. Monthly Notices of the Royal Astronomical Society, 158(3):291–304, jul 1972.

[47] JAMES C. KEMP, RAMON D. WOLSTENCROFT, and JOHN B. SWEDLUND. Circular Polarization: Jupiter and Other Planets. Nature, 232(5307):165–168, jul 1971.

[48] Kinsell L. Coulson, Victor S. Whitehead, and Charles Campbell. Polarized Views Of The Earth From Orbital Altitude. pages 35–41. International Society for Optics and Photonics, aug 1986.

[49] Brent D. Cameron, M. J. Raković, Mehrübe Mehrübeolu, George W. Kattawar, Sohi Rastegar, Lihong V. Wang, and Gerard L. Coté. Measurement and calculation of the two-dimensional backscattering Mueller matrix of a turbid medium. Optics Letters, 23(7):485, apr 1998.

[50] Brent D. Cameron, M. J. Raković, Mehrübe Mehrübeolu, George W. Kattawar, Sohi Rastegar, Lihong V. Wang, and Gerard L. Coté. Measurement and calculation of the two-dimensional backscattering Mueller matrix of a turbid medium: errata. Optics Letters, 23(20):1630, oct 1998.

[51] M.P Silverman and Wayne Strange. Object delineation within turbid media by backscattering of phase-modulated light. Optics Communications, 144(1-3):7–11, dec 1997.

[52] J. S. Ryan and A. I. Carswell. Laser beam broadening and depolarization in dense fogs. Journal of the Optical Society of America, 68(7):900, jul 1978.

[53] Min Xu and R R Alfano. Circular polarization memory of light. Physical Review E, 72(6):65601, 2005.

[54] Ralph Nothdurft and Gang Yao. Applying the polarization memory effect in polarization-gated subsurface imaging. Optics Express, 14(11):4656, may 2006.

[55] C M Macdonald, S L Jacques, and I V Meglinski. Circular polarization memory in polydisperse scattering media. Physical review. E, Statistical, nonlinear, and soft matter physics, 91(3):033204, mar 2015.

[56] Andreas Hielscher, Angela Eick, Judith Mourant, Dan Shen, James Freyer, and Irving Bigio. Diffuse backscattering Mueller matricesof highly scattering media. Optics Express, 1(13):441, dec 1997.

[57] John D. van der Laan, Jeremy B. Wright, David A. Scrymgeour, Shanalyn A. Kemme, and Eustace L. Dereniak. Evolution of circular and linear polarization in scattering environments. Optics Express, 23(25):31874, dec 2015.

[58] Duo-Min He. Underwater Laser-illuminated Range-gated Imaging scaled by 22.5 cm ns1 with serial targets. Journal of Ocean University of China, 3(2):208–219, oct 2004.

[59] S.C.W. Hyde, N.P. Barry, R. Jones, J.C. Dainty, and P.M.W. French. High resolution depth resolved imaging through scattering media using time resolved holography. Optics Communications, 122(4-6):111–116, jan 1996.

[60] M. Kempe, E. Welsch, and W. Rudolph. Comparative study of confocal and heterodyne microscopy for imaging through scattering media. Journal of the Optical Society of America A, 13(1):46, jan 1996.

[61] A.G. Andreou and Z.K. Kalayjian. Polarization imaging: principles and integrated polarimeters. IEEE Sensors Journal, 2(6):566–576, dec 2002.

[62] Ron H. Douglas and Craig W. Hawryshyn. Behavioural studies of fish vision: an analysis of visual capabilities. In The Visual System of Fish, pages 373–418. Springer Netherlands, Dordrecht, 1990.

[63] Iñigo Novales Flamarique, Craig W. Hawryshyn, and Ferenc I. Hárosi. Double-cone internal reflection as a basis for polarization detection in fish. Journal of the Optical Society of America A, 15(2):349, feb 1998.

[64] M. P. Rowe, N. Engheta, S. S. Easter, and E. N. Pugh. Graded-index model of a fish double cone exhibits differential polarization sensitivity. Journal of the Optical Society of America A, 11(1):55, jan 1994.

[65] J. Scott Tyo. Enhancement of the point-spread function for imaging in scattering media by use of polarization-difference imaging. Journal of the Optical Society of America A, 17(1):1, jan 2000.

[66] Akira Ishimaru. Wave propagation and scattering in random media. IEEE Press, 1997.

[67] A. Quehl. L. M. Lampert: Modern Dairy Products Composition. Food Value. Processing Chemistry. Bacteriology. Testing. Imitation Dairy Products. I. Auflage, 446 Seiten, 84 Abb., 64 Tab. Chemical Publishing Company, Inc., New York 1975, Preis: 13, 50 £. Food / Nahrung, 21(10):967–967, 1977.

[68] M.J.C. Van Gemert, S.L. Jacques, H.J.C.M. Sterenborg, and W.M. Star. Skin optics. IEEE Transactions on Biomedical Engineering, 36(12):1146–1154, dec 1989.

[69] M P Rowe, E N Pugh, J S Tyo, and N Engheta. Polarization-difference imaging: a biologically inspired technique for observation through scattering media. Optics letters, 20(6):608–10, mar 1995.

[70] W.B. Wang, S.G. Demos, J. Ali, and R.R. Alfano. Imaging fluorescent objects embedded inside animal tissues using polarization difference technique. Optics Communications, 142(4-6):161–166, oct 1997.

[71] D. Bicout, C. Brosseau, A. S. Martinez, and J. M. Schmitt. Depolarization of multiply scattered waves by spherical diffusers: Influence of the size parameter. Physical Review E, 49(2):1767–1770, feb 1994.

[72] Dominique Bicout and Christian Brosseau. Multiply scattered waves through a spatially random medium : entropy production and depolarization. Journal de Physique I, 2(11):2047–2063, nov 1992.

[73] F. C. MacKintosh, J. X. Zhu, D. J. Pine, and D. A. Weitz. Polarization memory of multiply scattered light. Physical Review B, 40(13):9342–9345, nov 1989.

[74] Http://www.horiba.com/us/en/scientific/products/particle characterization/applications/milk homogenization/. Milk Homogenization - HORIBA.

[75] Milk Homogenization - HORIBA.

[76] Tom J. Geurts P. Walstra, Pieter Walstra, Jan T. M. Wouters. Dairy Science and Technology. 2005.

[77] August Köhler. Ein neues Beleuchtungsverfahren f{ü}r mikrophotographische Zwecke. Zeitschrift f{ü}r wissenschaftliche Mikroskopie und f{ü}r mikroskopische Technik, 10(4):433–440, 1893.

[78] Daniel Feldkhun. Doppler Encoded Excitation Patterning (DEEP) Microscopy. Electrical, Computer & Energy Engineering Graduate Theses & Dissertations, 2010.

[79] W Lukosz. Optical Systems with Resolving Powers Exceeding the Classical Limit*. JOSA, 56(11):1463–1471, 1966.

[80] W Lukosz. Optical systems with resolving powers exceeding the classical limit. II. JOSA, 57(7):932–941, 1967.

[81] M. A. A. Neil, R. Juskaitis, and T. Wilson. Method of obtaining optical sectioning by using structured light in a conventional microscope. Optics Letters, 22(24):1905, dec 1997.

[82] M. G. L. Gustafsson. Surpassing the lateral resolution limit by a factor of two using structured illumination microscopy. SHORT COMMUNICATION. Journal of Microscopy, 198(2):82–87, may 2000.

[83] M A A Neil, R Juškaitis, and T Wilson. Real time 3D fluorescence microscopy by two beam interference illumination. Optics communications, 153(1):1–4, 1998.

[84] Juskaitis R Bastiaens P I Wilson T Neil MA Squire A. Wide-field optically sectioning fluorescence microscopy with laser illumination. Journal of Microscopy, 2000.

[85] Pier Alberto Benedetti, Valtere Evangelista, Dante Guidarini, and Stefano Vestri. Method for the acquisition of images by confocal, 2000.

[86] Rainer Heintzmann and Christoph G Cremer. Laterally modulated excitation microscopy: improvement of resolution by using a diffraction grating. In BiOS Europe'98, pages 185–196. International Society for Optics and Photonics, 1999.

[87] Jan T Frohn, Helmut F Knapp, and Andreas Stemmer. True optical resolution beyond the Rayleigh limit achieved by standing wave illumination. Proceedings of the National Academy of Sciences, 97(13):7232–7236, 2000.

[88] Rainer Heintzmann, Thomas M Jovin, and Christoph Cremer. Saturated patterned excitation microscopya concept for optical resolution improvement. JOSA A, 19(8):1599–1609, 2002.

[89] Mats G L Gustafsson, Lin Shao, Peter M Carlton, C J Rachel Wang, Inna N Golubovskaya, W Zacheus Cande, David A Agard, and John W Sedat. Three-dimensional resolution doubling in wide-field fluorescence microscopy by structured illumination. Biophysical journal, 94(12):4957–4970, 2008.

[90] Guoan Zheng, Roarke Horstmeyer, and Changhuei Yang. Wide-field, high-resolution Fourier ptychographic microscopy. Nature photonics, 7(9):739–745, 2013.

[91] Lei Tian, Xiao Li, Kannan Ramchandran, and Laura Waller. Multiplexed coded illumination for Fourier Ptychography with an LED array microscope. Biomedical optics express, 5(7):2376–2389, 2014.

[92] Benjamin Judkewitz and Changhuei Yang. Axial standing-wave illumination frequency-domain imaging (SWIF). Optics express, 22(9):11001–11010, 2014.

[93] Venugopal Srinivasan, Hsin-Chu Liu, and Maurice Halioua. Automated phase-measuring profilometry of 3-D diffuse objects. Applied optics, 23(18):3105–3108, 1984.

[94] Xianyu Su and Lian Xue. Phase unwrapping algorithm based on fringe frequency analysis in Fourier-transform profilometry. Optical Engineering, 40(4):637–643, 2001.

[95] Hua Du and Zhaoyang Wang. Three-dimensional shape measurement with an arbitrarily arranged fringe projection profilometry system. Optics letters, 32(16):2438–2440, 2007.

[96] W H Wang, Y S Wong, and G S Hong. 3D measurement of crater wear by phase shifting method. Wear, 261(2):164–171, 2006.

[97] Song Zhang and Peisen S Huang. Novel method for structured light system calibration. Optical Engineering, 45(8):83601, 2006.

[98] Feipeng Da and Shaoyan Gai. Flexible three-dimensional measurement technique based on a digital light processing projector. Applied optics, 47(3):377–385, 2008.

[99] Markus Vogel, Zheng Yang, Alexander Kessel, Christoph Kranitzky, Christian Faber, and Gerd Häusler. Structured-illumination microscopy on technical surfaces: 3D metrology with nanometer sensitivity. In SPIE Optical Metrology, pages 80820S—-80820S. International Society for Optics and Photonics, 2011.

[100] Liang-Chia Chen and Chung-Chih Huang. Miniaturized 3D surface profilometer using digital fringe projection. Measurement Science and Technology, 16(5):1061, 2005.

[101] Zheng Yang and Gerd Häusler. Structured-Illumination-MAcroscopy(SIMA) for high speed electronic inspection.

[102] Shujun Huang, Zonghua Zhang, Yan Zhao, Jie Dai, Chao Chen, Yongjia Xu, E Zhang, and Lili Xie. 3D fingerprint imaging system based on full-field fringe projection profilometry. Optics and Lasers in Engineering, 52:123–130, 2014.

[103] Gabriel Popescu, Takahiro Ikeda, Ramachandra R Dasari, and Michael S Feld. Diffraction phase microscopy for quantifying cell structure and dynamics. Optics letters, 31(6):775–777, 2006.

[104] YongKeun Park, Gabriel Popescu, Kamran Badizadegan, Ramachandra R Dasari, and Michael S Feld. Diffraction phase and fluorescence microscopy. Optics Express, 14(18):8263–8268, 2006.

[105] Gabriel Popescu, YongKeun Park, Ramachandra R Dasari, Kamran Badizadegan, and Michael S Feld. Coherence properties of red blood cell membrane motions. Physical Review E, 76(3):31902, 2007.

[106] Sri Rama Prasanna Pavani, Ariel R Libertun, Sharon V King, and Carol J Cogswell. Quantitative structured-illumination phase microscopy. Applied optics, 47(1):15–24, 2008.

[107] Basanta Bhaduri, Hoa Pham, Mustafa Mir, and Gabriel Popescu. Diffraction phase microscopy with white light. Optics letters, 37(6):1094–1096, 2012.

[108] Aamod Shanker, Lei Tian, and Laura Waller. Defocus-based quantitative phase imaging by coded illumination. In SPIE BiOS, pages 89490R—-89490R. International Society for Optics and Photonics, 2014.

[109] Soren D Konecky, Amaan Mazhar, David Cuccia, Anthony J Durkin, John C Schotland, and Bruce J Tromberg. Quantitative optical tomography of sub-surface heterogeneities using spatially modulated structured light. Optics express, 17(17):14780–14790, 2009.

[110] David J Cuccia, Frederic Bevilacqua, Anthony J Durkin, and Bruce J Tromberg. Modulated imaging: quantitative analysis and tomography of turbid media in the spatial-frequency domain. Opt. Lett, 30(11):1354–1356, 2005.

[111] David J Cuccia, Frederic Bevilacqua, Anthony J Durkin, Frederick R Ayers, and Bruce J Tromberg. Quantitation and mapping of tissue optical properties using modulated imaging. Journal of biomedical optics, 14(2):24012, 2009.

[112] Alexander J Lin, Adrien Ponticorvo, Soren D Konecky, Haotian Cui, Tyler B Rice, Bernard Choi, Anthony J Durkin, and Bruce J Tromberg. Visible spatial frequency domain imaging with a digital light microprojector. Journal of biomedical optics, 18(9):96007, 2013.

[113] Vijay Raj Singh, Heejin Choi, Elijah Y S Yew, Dipanjan Bhattacharya, Luo Yuan, Colin J R Sheppard, Jagath C Rajapakse, George Barbastathis, and Peter T C So. Improving signal-to-noise ratio of structured light microscopy based on photon reassignment. Biomedical optics express, 3(1):206–214, 2012.

[114] Darren Roblyer, Thomas D OSullivan, Robert V Warren, and Bruce J Tromberg. Feasibility of direct digital sampling for diffuse optical frequency domain spectroscopy in tissue. Measurement Science and Technology, 24(4):45501, 2013.

[115] Tyler B Rice, Elliott Kwan, Carole K Hayakawa, Anthony J Durkin, Bernard Choi, and Bruce J Tromberg. Quantitative, depth-resolved determination of particle motion using multi-exposure, spatial frequency domain laser speckle imaging. Biomedical optics express, 4(12):2880–2892, 2013.

[116] Daniel Feldkhun and Kelvin H Wagner. Doppler encoded excitation pattern tomographic optical microscopy. Applied Optics, 49(34):H47—-H63, 2010.

[117] Mats G L Gustafsson, John W Sedat, and David A Agard. Method and apparatus for three-dimensional microscopy with enhanced depth resolution, 1997.

[118] Amnon Yariv and Pochi Yeh. Optical waves in crystals, volume 10. Wiley, New York, 1984.

[119] Jieping. Xu and Robert. Stroud. Acousto-optic devices : principles, design, and applications. Wiley, 1992.

[120] Sangtaek Kim, Robert R Mcleod, M Saffman, and Kelvin H Wagner. Doppler-free, multiwavelength acousto-optic deflector for two-photon addressing arrays of Rb atoms in a quantum information processor. Applied optics, 47(11):1816–31, apr 2008.

[121] Joseph W Goodman. Introduction to Fourier optics. Roberts and Company Publishers, 2005.

[122] H Tu and SA Boppart. Coherent fiber supercontinuum for biophotonics. Laser & photonics reviews, 2013.

[123] PV Kelkar, F Coppinger, and AS Bhushan. Time domain optical sensing. -Optics Society 1999 ..., 1999.

[124] A Bassi, J Swartling, C D'Andrea, and A Pifferi. Time-resolved spectrophotometer for turbid media based on supercontinuum generation in a photonic crystal fiber. Optics, 2004.

[125] G McConnell. Confocal laser scanning fluorescence microscopy with a visible continuum source. Optics Express, 2004.

[126] P Li, K Shi, and Z Liu. Manipulation and spectroscopy of a single particle by use of white-light optical tweezers. Optics letters, 2005.

[127] C Dunsby, PMP Lanigan, and J McGinty. An electronically tunable ultrafast laser source applied to fluorescence imaging and fluorescence lifetime imaging microscopy. Journal of Physics D:, 2004.

[128] I Hartl, XD Li, C Chudoba, RK Ghanta, and TH Ko. Ultrahigh-resolution optical coherence tomography using continuum generation in an airsilica microstructure optical fiber. Optics, 2001.

[129] CH Camp, S Yegnanarayanan, and AA Eftekhar. Multiplex coherent anti-Stokes Raman scattering (MCARS) for chemically sensitive, label-free flow cytometry. Optics, 2009.

[130] Philip Russell. Photonic crystal fibers. science, 299(5605):358–362, 2003.

[131] Philip St J Russell. Photonic-crystal fibers. Journal of lightwave technology, 24(12):4729–4749, 2006.

[132] John M Dudley and J Roy Taylor. Ten years of nonlinear optics in photonic crystal fibre. Nature Photonics, 3(2):85–90, 2009.

[133] Govind P Agrawal. Nonlinear Fiber Optics. Academic, 2007.

[134] Zhaoming Zhu and Thomas G Brown. Polarization properties of supercontinuum spectra generated in birefringent photonic crystal fibers. JOSA B, 21(2):249–257, 2004.

[135] K. K. Sharma. Optics : principles and applications. Academic Press, 2006.

[136] Charles E Greninger. Reflective device for polarization rotation. Applied optics, 27(4):774–776, 1988.

[137] S Keppler, M Hornung, R Bödefeld, M Kahle, J Hein, and M C Kaluza. All-reflective, highly accurate polarization rotator for high-power short-pulse laser systems. Optics express, 20(18):20742–20747, 2012.

[138] Nikolai I Petrov. Achromatic polarization rotator. Applied optics, 46(25):6340–6343, 2007.

[139] Herbert G Winful. Self-induced polarization changes in birefringent optical fibers. Appl. Phys. Lett., 47(3):213–215, 1985.

[140] Herbert G Winful. Polarization instabilities in birefringent nonlinear media: application to fiber-optic devices. Opt. Lett., 11(1):33–35, 1986.

[141] G Gregori and S Wabnitz. New exact solutions and bifurcations in the spatial distribution of polarization in third-order nonlinear optical interactions. Phys. Rev. Lett., 56(6):600, 1986.

[142] Benedetto Daino, Giovanni Gregori, and Stefan Wabnitz. New all-optical devices based on third-order nonlinearity of birefringent fibers. Opt. Lett., 11(1):42–44, 1986.

[143] J M Soto-Crespo, Nail Akhmediev, and Adrian Ankiewicz. Soliton propagation in optical devices with two-component fields: a comparative study. J. Opt. Soc. Am. B, 12(6):1100–1109, 1995.

[144] Y Barad and Y Silberberg. Polarization evolution and polarization instability of solitons in a birefringent optical fiber. Phys. Rev. Lett., 78(17):3290, 1997.

[145] Stephen G Evangelides Jr, Linn F Mollenauer, James P Gordon, and Neal S Bergano. Polarization multiplexing with solitons. J. Lightwave Technol., 10(1):28–35, 1992.

[146] Mohammed N Islam, U C Paek, C E Soccolich, and J P Gordon. Soliton intensity-dependent polarization rotation. Opt. Lett., 15(1):21–23, 1990.

[147] K J Blow, N J Doran, and David Wood. Polarization instabilities for solitons in birefringent fibers. Opt. Lett., 12(3):202–204, 1987.

[148] Curtis R Menyuk. Stability of solitons in birefringent optical fibers. II. Arbitrary amplitudes. J. Opt. Soc. Am. B, 5(2):392–402, 1988.

[149] D N Christodoulides and R I Joseph. Vector solitons in birefringent nonlinear dispersive media. Opt. Lett., 13(1):53–55, 1988.

[150] Zhaoming Zhu and Thomas G Brown. Polarization properties of supercontinuum spectra generated in birefringent photonic crystal fibers. J. Opt. Soc. Am. B, 21(2):249–257, 2004.

[151] Zhaoming Zhu and Thomas Brown. Experimental studies of polarization properties of supercontinua generated in a birefringent photonic crystal fiber. Opt. Express, 12(5):791–796, 2004.

[152] V L Kalashnikov, Peter Dombi, Takao Fuji, W J Wadsworth, J C Knight, P St J Russell, R S Windeler, and Alexander Apolonski. Maximization of supercontinua in photonic crystal fibers by using double pulses and polarization effects. Appl. Phys. B, 77(2-3):319–324, 2003.

[153] Mikko Lehtonen, Goery Genty, Hanne Ludvigsen, and Matti Kaivola. Supercontinuum generation in a highly birefringent microstructured fiber. Appl. Phys. Lett., 82(14):2197–2199, 2003.

[154] Stéphane Coen, Alvin Hing Lun Chau, Rainer Leonhardt, John D Harvey, Jonathan C Knight, William J Wadsworth, and Philip St J Russell. Supercontinuum generation by stimulated Raman scattering and parametric four-wave mixing in photonic crystal fibers. J. Opt. Soc. Am. B, 19(4):753–764, 2002.

[155] John M. Dudley and Stéphane Coen. Supercontinuum generation in photonic crystal fiber. Reviews of Modern Physics, 78(4):1135–1184, oct 2006.

[156] F Luan, a Yulin, J C Knight, and Dmitry V Skryabin. Polarization instability of solitons in photonic crystal fibers. Optics express, 14(14):6550–6556, 2006.

[157] F Lu, Q Lin, W H Knox, and Govind P Agrawal. Vector soliton fission. Phys. Rev. Lett., 93(18):183901, 2004.

[158] YR Shen. Principles of Nonlinear Optics. 1984.

[159] Keith J Blow and David Wood. Theoretical description of transient stimulated Raman scattering in optical fibers. IEEE J. Quantum. Elect., 25(12):2665–2673, 1989.

[160] D Marcuse. Theory of dielectric optical waveguides. 2013.

[161] AW Snyder and J Love. Optical waveguide theory. 2012.

[162] JA Buck. Fundamentals of optical fibers. 2004.

[163] S. V. Chernikov and P. V. Mamyshev. Femtosecond soliton propagation in fibers with slowly decreasing dispersion. Journal of the Optical Society of America B, 8(8):1633, aug 1991.

[164] John M Dudley, Goëry Genty, and Stéphane Coen. Supercontinuum generation in photonic crystal fiber. Reviews of modern physics, 78(4):1135, 2006.

[165] Keith J Blow and David Wood. Theoretical description of transient stimulated Raman scattering in optical fibers. Quantum Electronics, IEEE Journal of, 25(12):2665–2673, 1989.

[166] RA Fisher and W Bischel. The role of linear dispersion in plane wave self phase modulation. Applied Physics Letters, 1973.

[167] Johan Hult. A fourth-order Runge–Kutta in the interaction picture method for simulating supercontinuum generation in optical fibers. Journal of Lightwave Technology, 25(12):3770–3775, 2007.

[168] VE Zakharov and AB Shabat. Exact theory of two-dimensional self-focussing and one-dimensional self-modulating waves in nonlinear media. Sov. Phys.-JETP (Engl. Transl.), 1972.

[169] Steven M Blair. Optical soliton-based logic gates. 1998.

[170] Roger H Stolen, James P Gordon, W J Tomlinson, and Hermann A Haus. Raman response function of silica-core fibers. JOSA B, 6(6):1159–1166, 1989.

[171] D Hollenbeck and CD Cantrell. Multiple-vibrational-mode model for fiber-optic Raman gain spectrum and response function. JOSA B, 2002.

[172] G. E. Walrafen and P. N. Krishnan. Model analysis of the Raman spectrum from fused silica optical fibers. Applied Optics, 21(3):359, feb 1982.

[173] Q Lin and Govind P Agrawal. Raman response function for silica fibers. Optics letters, 31(21):3086–3088, 2006.

[174] Robert W Boyd. Nonlinear optics. Academic press, 2003.

[175] Kelvin H Wagner. Nonlinear Optics lecture Notes. University of Coloradu at Boulder, 2009.

[176] Q Lin and Govind P Agrawal. Raman response function for silica fibers. Opt. Lett., 31(21):3086–3088, 2006.

[177] E A Golovchenko and A N Pilipetskii. Unified analysis of four-photon mixing, modulational instability, and stimulated Raman scattering under various polarization conditions in fibers. JOSA B, 11(1):92–101, 1994.

[178] Yuji Kodama and Akira Hasegawa. Nonlinear pulse propagation in a monomode dielectric guide. IEEE J. Quantum. Elect., 23(5):510–524, 1987.

[179] R Driben, B A Malomed, A V Yulin, and D V Skryabin. Newton's cradles in optics: From N-soliton fission to soliton chains. Phys. Rev. A, 87(6):63808, 2013.

[180] R Ulrich and A Simon. Polarization optics of twisted single-mode fibers. Appl. Optics, 18(13):2241–2251, 1979.